The Thesis Committee for Benjamin Witten Barr
Certifies that this is the approved version of the following thesis:

Investigation and Modeling of Coupled Thermochemical and Thermomechanical Erosion in Thermally Degrading Systems

APPROVED BY
SUPERVISING COMMITTEE:

Supervisor:

Ofodike A. Ezekoye

Gregory J. Rodin

Investigation and Modeling of Coupled Thermochemical and Thermomechanical Erosion in Thermally Degrading Systems

by

Benjamin Witten Barr, B.S.

Thesis

Presented to the Faculty of the Graduate School of

The University of Texas at Austin

in Partial Fulfillment

of the Requirements

for the Degree of

Master of Science in Engineering

The University of Texas at Austin

May 2012

Dedication

This thesis is dedicated to my dear family and friends, whose love has brought me this far and will bear me into the future. No work which I can create and dedicate is an adequate symbol for my love for them.

Acknowledgements

I would first like to thank my advisor, Dr. Ofodike Ezekoye, for his guidance and support throughout my graduate education. His knowledge, experience, and patience have been invaluable in my work and in training me to become a competent, responsible engineer. I would also like to acknowledge Dr. Rochan Upadhyay and Reed Anzalone for their prior work in our ablation group. Their work has been the foundation of my own, and their help and cooperation during my time in the group have enhanced the quality of my own contribution.

I thank the Center for Predictive Engineering and Computational Sciences (PECOS) at the University of Texas at Austin for their support of my work. This work was funded by the Department of Energy [National Nuclear Security Administration] under Award Number [DE-FC52-08NA28615]. I would also like to thank two specific members of the PECOS staff, Chris Simmons and Karl Schulz, for their help in administrative and computational matters, respectively.

Additionally, I would like to thank Dr. Gregory Rodin and Dr. Joseph Koo for their collaboration on this and other projects relating to ablation, and I would like to thank the members of the UT Fire Research Group for their friendship and support during my time in graduate school.

Finally, I would like to thank my parents, Laurie and Britten Barr, my brother, Winston Barr, my friends, Ladd Spears and Paul Boulmay, and my extended family, biological and otherwise, whose love and support have made this achievement possible. The pursuit of scientific understanding is inconsequential to me without these.

Abstract

Investigation and Modeling of Coupled Thermochemical and Thermomechanical Erosion in Thermally Degrading Systems

Benjamin Witten Barr, M.S.E.

The University of Texas at Austin, 2012

Supervisor: Ofodike A. Ezekoye

The coupled effects of thermochemical and thermomechanical erosion are investigated. A quasi-steady ablation model with finite rate surface chemistry is developed and applied to a solid carbon combustion scenario to investigate the system's behavior in situations in which surface reactions are not in equilibrium. It is found that in this regime, the system can be described effectively in terms of the B number and the Damkohler number, and a useful algebraic relationship between these parameters is determined for nonequilibrium behavior.

The thermochemical ablation model is then expanded by considering mechanical removal of thermochemically weakened material from the ablating surface. A model is developed for a randomly oriented carbon fiber preform material, like that used in the production of phenolic impregnated carbon ablator (PICA), and this model is incorporated into the previously developed ablation code. It is found that for PICA in realistic reentry scenarios, the removal of individual fibers from the ablating surface by mechanical erosion is not an important mass loss mechanism, although hypothetical situations exist where this mechanism for mechanical removal of material is non-negligible.

The thermo-chemo-mechanical erosion mechanism is then extended to address brand generation in wildland fire scenarios. A model is developed to predict the size and number distribution of embers generated from a tree with fractal geometry. This model is coupled to a simple plume and propagation model similar to those existing in the literature, and a case study is performed for a realistic wildfire scenario. The presence of an optimal branch diameter for brand propagation is identified, and areas for future work in thermo-chemo-mechanical degradation are discussed.

Table of Contents

List of Tables

List of Figures

Chapter 1: Introduction

Durability of solid materials is a critical consideration in the design of systems which operate in extreme environments. In extreme conditions, physical and chemical changes occur in solid materials which greatly affect their thermal, rheological, electrical, elastic, acoustic, and strength properties. The full spectrum of changes that a material may undergo is vast, and in certain applications, the materials of greatest value are those that can endure extreme environments and remain unchanged, or that can at least be sacrificed to protect more essential parts of their system.

This is the case for Thermal Protection Systems (TPS) in atmospheric reentry. These systems are designed to protect vehicles from the extreme environments experienced during the reentry process, and their detailed design has occupied the attention of generations of aerospace and mechanical engineers. A specific class of lightweight TPS materials, called ablative materials, is designed to degrade while in use. These materials, which are usually solids or composites containing carbon, undergo chemical reactions which absorb energy from the environment and release gaseous products which thicken the external boundary layer, thus providing effective thermal protection in the midst of their own destruction.

The primary degradation mechanism of ablative TPS materials, such as graphite, PICA (phenolic impregnated carbon ablator), and carbon-carbon ablators, is mass loss by chemical reactions at high temperatures. This thermochemical ablation may occur volumetrically (pyrolysis of phenolic matrix) or at the surface of the ablator (reactions with the gases in the boundary layer or sublimation). Volumetric processes result in significant mass loss, a decrease in density, and usually the formation of a carbonaceous char at the surface of the solid. Surface reactions occur on the carbonaceous surface and result in actual regression of the surface. The thermochemical degradation mechanism has been studied and modeled in great detail, but there is still room for further investigation and enhanced understanding.

In addition to thermochemical erosion, the high Mach number flows across the surface of the ablator may subject it to mechanical erosion, in which discrete solid

particles are removed from the surface. This generally augments the recession rate of the solid, but its mechanism is complicated and highly dependent on the material in use. Additionally, mechanical erosion is not ubiquitous in ablative TPS scenarios in the same way that thermochemical erosion is, so this degradation mechanism has not been studied as extensively.

In this work both the thermochemical and mechanical degradation mechanisms are investigated. First, thermochemical erosion is analyzed using a modeling approach that has been developed and implemented by Upadhyay, Anzalone, Ezekoye, and other researchers at the Center for Predictive Engineering and Computational Sciences (PECOS) at the University of Texas at Austin. Their prior work has produced a detailed ablation model capable of predicting accurately the recession rate of different classes of materials. The current work analyzes the major modeling assumptions of this and other advanced models in order to better understand the way their behavior changes under different environmental conditions. Informed by the results of the thermochemical erosion study, the mechanical erosion mechanism is then investigated. A model is developed for PICA which shows how mechanical mass loss may be dependent not only on the state of friction at the surface but also on the thermochemical erosion rate itself.

The mechanical loss of material in thermal/fluid systems is not exclusive to the reentry scenario, however, and the concepts developed in the PICA mechanical erosion study are subsequently extended to a seemingly unrelated realm: the generation of firebrands in a wildland fire. It is found that in this scenario, for branching vegetative fuels, the loss of combustible solid mass as embers is dependent upon the thermochemical degradation of the plant within the flame front. A model for the generation and propagation of brands is developed, and areas for future work in brand generation modeling are identified.

A key conclusion of the current work is the observation that in many systems, the processes of thermochemical and mechanical loss of mass are intimately coupled. The overall modeling process developed in this thesis for thermo-chemo-mechanical degradation will be shown to be equally applicable to TPS in atmospheric reentry and

tree branches in a wildfire. While the development will largely focus on TPS, it will be shown that some of the results can be applied to the degradation of tree branches and eventual loss of tree elements in the extreme environment of a wildfire.

Chapter 2: Thermochemical Ablation with Finite Rate Kinetics

The physics of ablation in hypersonic flows is extremely complex, as shown in Figure 2.1. The high velocities characteristic of reentry scenarios typically induce bow shock waves around the nose of a vehicle, heating the post-shock gases to high temperatures and causing reactions to occur among the chemical species in the flow. The high-enthalpy external flow applies radiative and convective heat fluxes to the surface of the ablator, which undergoes chemical reactions in response to the increased solid temperature. Chemical reactions may occur at the surface of the ablator (oxidation, nitridation, or sublimation) or in-depth (pyrolysis of virgin material), and the gases produced are expelled from the surface, removing both mass and energy from the ablating surface as it recedes. In this manner, an ablating material becomes an effective thermal protection system because energy from the external heat flux is carried away by gaseous reaction products and not allowed to penetrate to the protected surface. Additionally, the gases blowing out of the surface insulate the surface from the high-enthalpy external flow, decreasing the convective heat transfer coefficient.

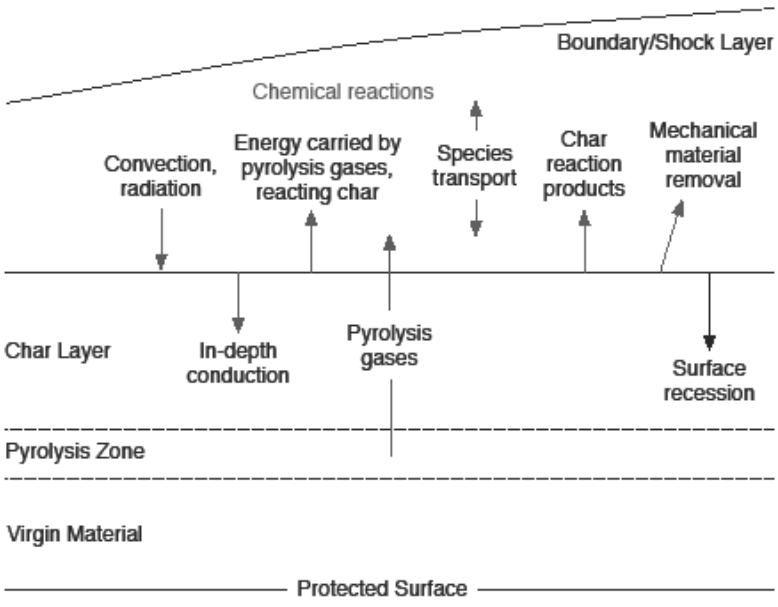

Figure 2.1: The physics of ablation in hypersonic environments, taken from [1].

Although the processes involved in hypersonic ablation are exceedingly complex, engineering predictions are possible and have been made with success in this domain since the adoption of ablating systems in the 1950s. The complete modeling of reentry physics has been the work of generations of engineers and scientists, and in this work we respectfully limit our scope to the thermo-chemo-mechanical degradation processes that occur at the surface of the TPS. The modeling of this component of hypersonic reentry is possible using laws of conservation (for mass and energy) and models for surface chemistry. The development of the conservation laws is relatively straightforward, but the modeling of surface chemistry requires more consideration.

Two main approaches for surface chemistry are available and have been widely implemented in TPS modeling; these are the equilibrium and kinetic approaches. In the equilibrium formulation, it is assumed that the time scale associated with chemical reactions is short compared to the time scale associated with heat and mass transport, and therefore that gaseous species at the surface are essentially in thermodynamic equilibrium throughout the time of interest. There is then (generally) a unique gas composition at the surface for each value of surface temperature, and this composition is calculated using a minimization of Gibbs energy. The surface composition is related to a set of species mass balances for the open system, and curves of wall temperature versus the B number, a nondimensional mass loss rate, are obtained for designated values of surface pressure. The specific values of wall temperature and B number for a given scenario are then determined based on the system energy balance. The equilibrium model has been implemented in a number of widely used models [2-7].

The kinetic approach assumes that surface reactions are not fast enough to be perpetually in equilibrium and models surface thermochemistry using finite rate reactions which depend at least on the surface temperature and surface species concentrations. These reaction rates are incorporated into species and energy balances, whose solution provides the desired values for wall temperature and surface recession rate. Kinetic models for thermochemistry have also been previously implemented in ablation modeling [4, 8, 9].

For reentry scenarios in which reaction time scales are very short relative to transport time scales, the kinetic model returns the same solution as the equilibrium model; this behavior is well observed in chemically reacting systems. What is less clear is the coupled behavior of the surface species concentrations, wall temperature, and B number as a system transitions between equilibrium and nonequilibrium regimes in reentry scenarios. The present section attempts to address this issue by drawing analogy to results obtained in combustion literature [10-12], where the theory of the B number has been extensively treated and the relationship between reaction and transport time scales is described in nondimensional terms using the Damkohler number. In the following section, we develop a model for an ablating system using the kinetic model, which allows exploration of the transition to equilibrium behavior. This model is then simplified so that it accounts for all relevant physical processes in ablation but simplifies submodels such as property evaluation, reaction chemistry, and transport coefficients. This allows for more efficient exploration of the governing physics without the complication of extensive algebraic manipulation. Using the simplified model, we explore the qualitative behavior of the transition out of the equilibrium regime and identify relevant nondimensional parameters for describing the physical behaviors. We develop an approximate formulation for the behavior of the B number in nonequilibrium regimes and validate the formulation with experimental data.

2.1 The Governing Physics of Quasi-Steady-State Ablation

The following subsection derives equations which describe the heat transfer, mass transfer, and chemical processes involved in ablation. First, conservation laws for mass and energy are developed globally and across the ablating surface; these laws are valid regardless of the model used for reaction chemistry. A model for finite rate kinetics is then developed and incorporated into the conservation laws, and additional submodels are also described. This model for ablation has been implemented with a large amount of detail in all submodels by researchers at PECOS so that it produces quantitatively accurate results in realistic scenarios [1, 13]. Detailed derivation of all submodels can be

found in those works, but since quantitative accuracy is not the focus of this work, the detail of some submodeling is omitted in the following derivation. After the model is described generally, it is simplified for the case of solid carbon oxidation, and a useful form is obtained for the forthcoming investigation of the B number.

2.1.1 Thermochemical Ablation Model Derivation

In order to model the complex physics in Figure 2.1, a number of assumptions are made. The most important one is the quasi-steady-state assumption, which states that, although the heating and decomposition of an ablating material is a transient process, the transient response is very close to the steady state solution throughout the time of interest. This allows time derivatives to be removed from the governing partial differential equations, greatly simplifying the problem. The quasi-steady-state assumption is valid when changes in environmental conditions are very small within the characteristic thermal response time of the solid. For instance, for a system heated by an external heat flux $\dot{q}''$, the heat flux and its change $\Delta\dot{q}''$ over the characteristic time τ must obey the relationship

$$\frac{\Delta\dot{q}''}{\dot{q}''} \ll 1 \tag{2.1}$$

The first term of a Taylor series expansion for $\Delta\dot{q}''$ gives the approximation

$$\Delta\dot{q}'' = \frac{d\dot{q}''}{dt}\tau \tag{2.2}$$

The characteristic thermal response time is the time that it takes for the transient solution to approach the steady state solution. For conduction within a solid with no recession (there is no recession in an ablating system in the early stages of heating), the governing partial differential equation is

$$\rho c_p \frac{\partial T}{\partial t} = k\frac{\partial^2 T}{\partial x^2} \tag{2.3}$$

where ρ is density, c_p is constant pressure specific heat capacity, and k is thermal conductivity. Scaling analysis on this equation defines the transient thermal penetration depth δ_{tr} as

$$\delta_{tr} \sim \sqrt{\alpha t} \tag{2.4}$$

where α is thermal diffusivity.

The steady state recession of an ablative material receding at velocity v is governed by

$$\rho c_p v \frac{\partial T}{\partial x} = k \frac{\partial^2 T}{\partial x^2} \tag{2.5}$$

Scaling defines the steady state thermal penetration depth δ_{ss} as

$$\delta_{ss} \sim \frac{\alpha}{v} \tag{2.6}$$

The characteristic time $t = \tau$ is then the time for which $\delta_{tr} = \delta_{ss}$, or

$$\tau \sim \frac{\alpha}{v^2} \tag{2.7}$$

Incorporating Equations 2.2 and 2.7 into 2.1 gives the condition for the quasi-steady-state approximation:

$$\frac{d\dot{q}''}{dt} \frac{\alpha}{v^2 \dot{q}''} \ll 1 \tag{2.8}$$

A typical carbon-carbon ablator has thermal diffusivity on the order of 10^{-5} m^2/sec and recedes at around 1 mm/sec under a heat flux of 5 MW/m^2. Table 2.1 shows the left side of Equation 2.8 evaluated for different values of $d\dot{q}''/dt$. For this scenario, systems with rates of change in the external heat flux less than about 0.1 MW/m^2-s can be modeled at each point in time by applying steady state theory to the heat flux at that point in time.

Table 2.1: Evaluation of quasi-steady-state approximation for a realistic reentry scenario.

$\frac{d\dot{q}''}{dt}$ (MW/m^2-s)	$\frac{d\dot{q}''}{dt} \frac{\alpha}{v^2 \dot{q}''}$
0.001	0.002
0.01	0.02
0.1	0.2
1	2

In addition to the quasi-steady-state approximation, the model uses a one-dimensional spatial coordinate system, global energy and mass balances for the ablating solid (meaning that internal profiles are not calculated), equilibrium in-depth pyrolysis occurring at a fixed temperature, non-reacting pyrolysis gases which are in thermal equilibrium with the solid, and a non-reacting boundary layer. In this section, we also assume that mechanical erosion does not occur, although this assumption will be relaxed in Chapter 3.

We now derive the governing equations for quasi-steady-state ablation. Figure 2.2 shows the global energy balance for the ablating solid undergoing pyrolysis and surface reactions and receding at a speed v_s, with a frame of reference attached to the moving surface and x positive into the solid. At the ablating wall ($x = 0$, subscript w), energy enters the solid through conduction and leaves through the enthalpy of the carbonaceous char (subscript C) and the pyrolysis gases (subscript py). The other side of the control volume is described as the transferred substance state, or T state, which is the depth at which no thermal effects are felt and no gradients exist in any variables. At the T state, the only energy entering or leaving the control volume is the enthalpy of the virgin material entering (subscript v).

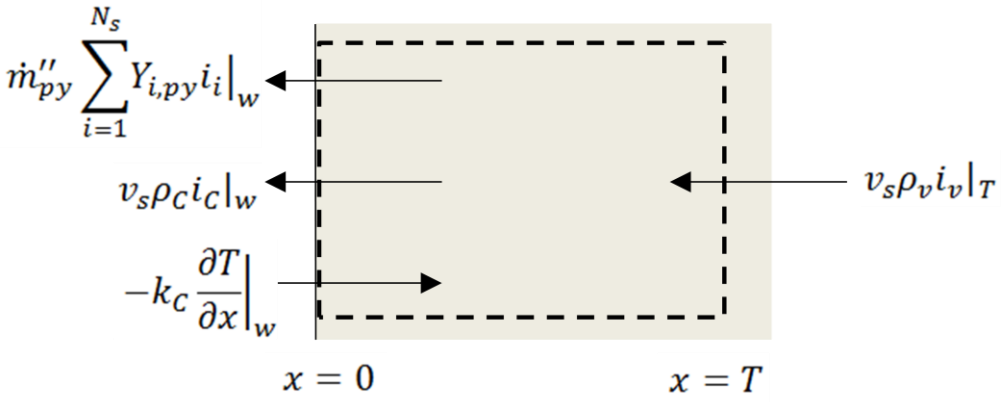

Figure 2.2: Control volume for global energy conservation in solid.

Conservation of energy for the control volume in Figure 2.2 gives

$$k_C \frac{\partial T}{\partial x}\bigg|_w = -\rho_C v_s i_C|_w + \rho_v v_s i_v|_T - \dot{m}''_{py} \sum_{i=1}^{N_s} Y_{i,py} i_i\big|_w \qquad 2.9$$

where i is specific enthalpy, $\dot{m}''$ is mass flux, N_s is the total number of gaseous species considered in the pyrolysis gas and boundary layer flows, and Y is the mass fraction for gaseous species. The terms are, from left to right, conduction into the solid, enthalpy of char leaving the solid, enthalpy of virgin material entering the solid, and enthalpy of pyrolysis gases leaving the solid.

At the surface, each gas species is conserved as shown in Figure 2.3. The species mass balance takes the form

$$J_i|_w + \rho_g v_w Y_{i,w} = \widetilde{N}_i + \dot{m}''_{py} Y_{i,py} \qquad 2.10$$

The terms are, from left to right, diffusive flux of the i^{th} species out of the wall in the gas phase, mass flux of the i^{th} species in the bulk gas flow out of the wall (where v_w is the blowing velocity of the gas from the wall and subscript g refers to the gas phase at the wall), generation of the i^{th} species through surface reactions, and mass flux of the i^{th} species in the pyrolysis gases.

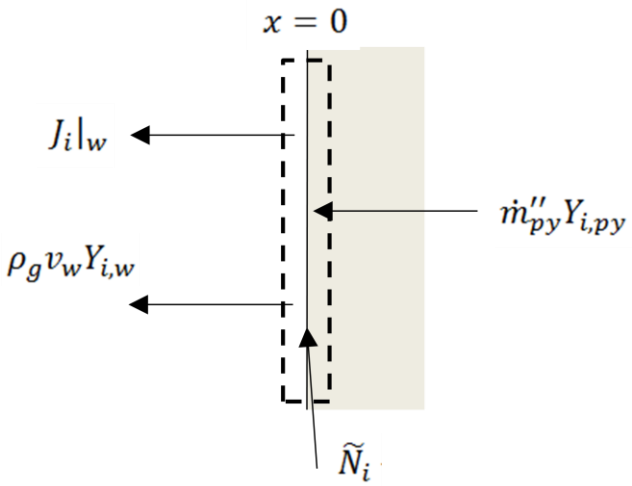

Figure 2.3: Control volume for species conservation at ablating surface.

Energy is conserved at the ablating surface as shown in Figure 2.4. The surface energy balance is

$$-k_g \frac{\partial T}{\partial x}\Big|_w - \sum_{i=1}^{N_s} i_i J_i|_w - \rho_g v_w \sum_{i=1}^{N_s} Y_{i,w} i_i\Big|_w + \rho_C v_s i_C|_w + \dot{m}''_{py} \sum_{i=1}^{N_s} Y_{i,py} i_i\Big|_w + \alpha \dot{q}''_{ext} - \varepsilon\sigma\left(T_w{}^4 - T_{surr}{}^4\right) + k_C \frac{\partial T}{\partial x}\Big|_w = 0 \quad (2.11)$$

where α is the surface absorptivity, $\dot{q}''_{ext}$ is an external heat flux applied to the surface (such as radiation from hot gas in the boundary layer), ε is the surface emissivity, σ is the Stefan-Boltzmann constant, and T_{surr} is the farfield surroundings temperature. The terms in the energy balance are, from left to right, diffusive flux of energy from the external gas phase into the surface, energy carried by gases diffusing out of the surface, energy carried by gases in the bulk flow out of the surface, energy carried by char convecting into the surface, energy carried by pyrolysis gases convecting into the surface, applied external flux, radiation exchange between surface and surroundings, and diffusive flux of energy from the surface into the solid. Equation 2.11 may be simplified using Equations 2.9 and 2.10. Substituting for the diffusive flux into the solid in Equation 2.11 using Equation 2.9, reformulating the second and third terms in Equation 2.11 using Equation 2.10, and replacing the first term in Equation 2.11 with a generalized convective flux gives the final simplified surface energy balance:

$$\dot{q}''_{conv,in} - \sum_{i=1}^{N_s} \left(\tilde{N}_i + \dot{m}''_{py} Y_{i,py}\right) i_i|_w + \rho_v v_s i_v|_T + \alpha \dot{q}''_{ext} - \varepsilon\sigma\left(T_w{}^4 - T_{surr}{}^4\right) = 0 \quad (2.12)$$

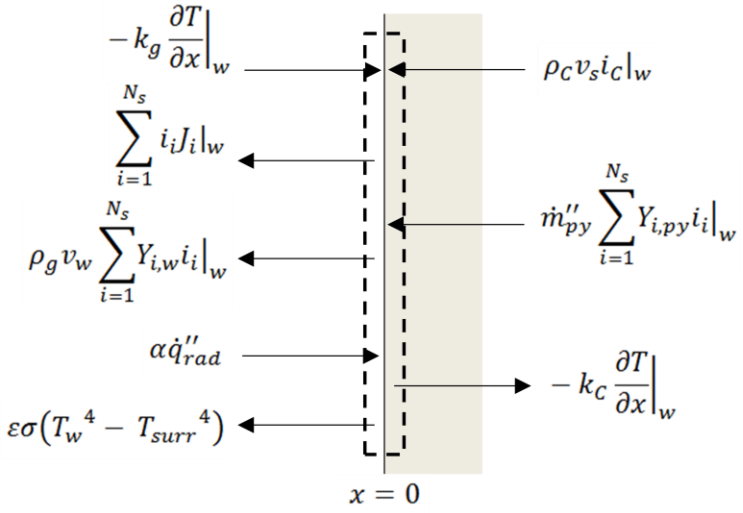

Figure 2.4: Control volume for energy conservation at ablating surface.

The equations just derived are valid for both the equilibrium and kinetic approaches. To model the chemical source terms $\widetilde{N}_i$ in Equation 2.12, surface chemistry must be modeled using one of the two approaches. Because we wish to explore the nonequilibrium regime, we choose to model surface chemistry using finite rate reactions for heterogeneous combustion of surface carbon. A very large number of species and reactions are present at the ablating surface in a real reentry scenario, and it is up to the discretion of the modeler to determine the proper number of species and reactions to model for a particular desired level of accuracy. To illustrate, the existing ablation model of PECOS [1, 13] considers a total of N_s = 13 gaseous species: reacting species (CO, CN, C_3, O, O_2, N), non-reacting species in the external flow (N_2, NO, C_2, $C_{(g)}$), and non-reacting species in the pyrolysis gases (C_2H, H_2, H). In this model, the reacting species participate in four finite rate reactions with carbon:

- Oxidation (with atomic oxygen): $C_{(s)} + O \rightarrow CO$
- Oxidation (with molecular oxygen): $C_{(s)} + \frac{1}{2}O_2 \rightarrow CO$
- Nitridation: $C_{(s)} + N \rightarrow CN$
- Sublimation: $3C_{(s)} \rightarrow C_3$

In the general finite rate kinetic model, surface reactions are modeled in the general form

$$\dot{m}''_{k,C} = \rho_g Y_{k,w} {T_w}^n A_k exp\left(-\frac{E_{a,k}}{\bar{R}T_w}\right)\frac{\nu_C W_C}{\nu_k W_k} \qquad 2.13$$

which is an Arrhenius statement for the loss of carbon due to the k^{th} gas phase reactant ($\dot{m}''_{k,C}$) in each of the $k = 1 \rightarrow K$ reactions. In the above equation, n is a dimensionless exponent, A_k is the preexponential factor for the k^{th} gas phase reactant, $E_{a,k}$ is the activation energy, $\bar{R}$ is the universal gas constant, ν is a stoichiometric coefficient for the reaction considered, and W is the molar mass. For the sublimation reaction in the PECOS model, the difference between the equilibrium and actual surface mole fractions of C_3 ($x_{C_3,eq} - x_{C_3}$) replaces the wall mass fraction of C_3 ($Y_{C_3,w}$). The mass loss rates of carbon are related to the chemical source terms $\widetilde{N}_i$ by

$$\widetilde{N}_i = \sum_{k=1}^{K} a_k \left(\dot{m}''_{k,C}\frac{\nu_i W_i}{\nu_C W_C}\right) \qquad 2.14$$

where a_k = 1 if the species i is a product of the k^{th} reaction, -1 if the species is a reactant, and 0 if the species is not involved in the reaction.

Global conservation of mass also implies the following equalities between the char mass flux rate and the surface reaction rates and between the fluxes of blowing gas ($\dot{m}''_g$), char ($\dot{m}''_C$), pyrolysis gas ($\dot{m}''_{py}$), and virgin material ($\dot{m}''_v$):

$$\dot{m}''_C = \rho_C v_s = \sum_{k=1}^{K} \dot{m}''_{k,C} = \dot{m}''_{O,C} + \dot{m}''_{O_2,C} + \dot{m}''_{N,C} + \dot{m}''_{C_3,C} \qquad 2.15$$

$$v_w \rho_g = \dot{m}''_g = \dot{m}''_C + \dot{m}''_{py} = \dot{m}''_v = \rho_v v_s \qquad 2.16$$

The right side of Equation 2.15 must in general include contributions from all reactions modeled; the expression for the PECOS model is shown.

The final submodels for the thermochemical ablation model are those for pyrolysis gas production and bow shocks. For cases in which the ablator decomposes and releases pyrolysis gas, the mass flux of gases is determined by the change in density between the virgin and char, as shown through a rearrangement of Equation 2.16:

$$\dot{m}''_{py} = \dot{m}''_v - \dot{m}''_c = (\rho_v - \rho_c)v_s \quad 2.17$$

Pyrolysis is assumed to occur at a specified pyrolysis temperature, and the composition of the pyrolysis gases is determined through an equilibrium calculation of the elemental constituents of the virgin material at that temperature (similar to the calculations performed at the surface for ablation with the equilibrium assumption at the surface).

In the event of a bow shock, the state and composition of the post-shock gases at the edge of the boundary layer are determined based on the Rankine-Hugoniot relations:

$$i_1 + \frac{1}{2}{u_1}^2 = i_0 + \frac{1}{2}{u_0}^2 \quad 2.18$$

$$p_1 + \rho_1{u_1}^2 = p_0 + \rho_0{u_0}^2 \quad 2.19$$

where u is the gas velocity, p is the static pressure, and subscripts 0 and 1 refer to pre- and post-shock gases, respectively. Here the pre- and post-shock gases are assumed to be in thermal and chemical equilibrium, and the post-shock composition is determined based on equilibrium gas chemistry.

Lastly, gas state properties are related using the ideal gas law, and thermodynamic properties such as enthalpy are generated using polynomial correlations created for NASA's Chemical Equilibrium with Applications code [14].

It should be noted here that the preceding derivation is completely general; if the shock model is removed the conservation equations and chemistry are applicable to any case of quasi-steady solid combustion in radiative and convective contact with a reservoir. This fact will be demonstrated in the following subsection when the model is applied to a case of carbon combustion and is important for the following validation of the ablation model using combustion data.

2.1.2 Simplified Model: Heterogeneous Oxidation of Solid Carbon

For complex systems such as an ablating TPS in reentry, it is often useful to develop a simplified model for exploring the system's fundamental behavior. We accomplish this by considering the oxidation of solid carbon (such as graphite or the carbon fiber preform used in some composite TPS materials), which does not pyrolyze,

by molecular oxygen in air ($Y_{O_2,\infty} = 0.232$, $Y_{N_2,\infty} = 0.768$) to produce CO according to the reaction

$$C_{(s)} + \frac{1}{2}O_{2(g)} \rightarrow CO_{(g)} \qquad 2.20$$

where 1 gram of O_2 burns with $r = (\nu_C W_C)/(\nu_{O_2} W_{O_2})$ grams of C to make $(1 + r)$ g of CO. This is certainly not the only reaction that takes place on a reentry TPS, but the choice simplifies the governing equations and facilitates investigation of their behavior, and the conclusions drawn may then be extrapolated to more complicated, realistic cases. The single reaction is also easier to characterize experimentally, allowing the opportunity for our model to be validated against experiments.

For the simplified model, three species must be considered in the gas phase: O_2, CO, and N_2. The mass balance (Equation 2.10) for O_2 reduces to

$$J_{O_2}\big|_w + \rho_g v_w Y_{O_2,w} = \widetilde{N}_{O_2} \qquad 2.21$$

Since O_2 is the only species that reacts with the graphite, Equation 2.15 gives $\dot{m}''_C = \dot{m}''_{O_2,C}$, and since pyrolysis does not occur, Equation 2.16 gives $\rho_g v_w = \dot{m}''_g = \dot{m}''_C = \dot{m}''_v$. Defining, for convenience, the mass consumption rate of oxygen as

$$\dot{m}''_{O_2} = -\widetilde{N}_{O_2} = \rho_g Y_{O_2,w} A_{O_2} exp\left(-\frac{E_{a,O_2}}{\bar{R} T_w}\right) \qquad 2.22$$

where the exponent n is set to zero, and defining the diffusive flux $J_{O_2}\big|_w$ by analogy to Newton's law of cooling with mass transfer coefficient h_m, the oxygen mass balance becomes

$$h_m\left(Y_{O_2,w} - Y_{O_2,\infty}\right) + \dot{m}''_{O_2} r Y_{O_2,w} + \dot{m}''_{O_2} = 0 \qquad 2.23$$

where the subscript ∞ refers to the gas phase freestream state. The gas density adjacent to the wall (ρ_g) in Equation 2.22 should generally be calculated according to the ideal gas law using the molecular weight of the mixture at the wall ($W_{mix,w}$). However, little error is introduced and the solution to the conservation equations is immensely simplified by assuming that the mixture molecular weight is approximately that of the freestream, which in this case is air ($W_{mix,w} \approx W_{air}$). This assumption is used in the simplified model.

The surface energy balance (Equation 2.12) is simplified to yield

$$-h(T_w - T_\infty) + \dot{m}''_{O_2} i_{O_2}\big|_w - \dot{m}''_{O_2}(1+r) i_{CO}|_w + \dot{m}''_{O_2} r i_v|_T + \alpha \dot{q}''_{ext} - \varepsilon\sigma\left({T_w}^4 - {T_{surr}}^4\right) = 0 \quad (2.24)$$

where Newton's law of cooling with heat transfer coefficient h has been used to define the convective flux. The enthalpy of each species is made up of formation enthalpy and sensible enthalpy, which may be approximated using constant specific heats as

$$i_i = \frac{\tilde{\imath}_i^o}{W_i} + c_{p,i}\left(T - T_{ref}\right) \quad (2.25)$$

where $\tilde{\imath}_i^o$ is the molar heat of formation and T_{ref} is the reference temperature at which $\tilde{\imath}_i^o$ is evaluated. The energy balance then becomes

$$-h(T_w - T_\infty) + \dot{m}''_{O_2}\left[\Delta i_{comb,O_2} + c_{p,O_2}\left(T_w - T_{ref}\right) - c_{p,CO}\left(T_w - T_{ref}\right)(1+r) + c_{p,C}\left(T_T - T_{ref}\right)r\right] + \alpha \dot{q}''_{ext} - \varepsilon\sigma\left({T_w}^4 - {T_{surr}}^4\right) = 0 \quad (2.26)$$

where the enthalpy of combustion on an O_2 basis is defined as

$$\Delta i_{comb,O_2} = \frac{1}{W_{O_2}}\left(\tilde{\imath}_{O_2}^o - \tilde{\imath}_{CO}^o \frac{\nu_{CO}}{\nu_{O_2}} + \tilde{\imath}_C^o \frac{\nu_C}{\nu_{O_2}}\right) \quad (2.27)$$

If we assume that the virgin material enters at T_{ref}, the final form of the energy balance is

$$-h(T_w - T_\infty) + \dot{m}''_{O_2}\left[\Delta i_{comb,O_2} + c_{p,O_2}\left(T_w - T_{ref}\right) - c_{p,CO}\left(T_w - T_{ref}\right)(1+r)\right] + \alpha \dot{q}''_{ext} - \varepsilon\sigma\left({T_w}^4 - {T_{surr}}^4\right) = 0 \quad (2.28)$$

Equations 2.22, 2.23, and 2.28 can now be solved iteratively to obtain T_w, $Y_{O_2,w}$, and $\dot{m}''_{O_2}$. The surface recession rate v_s for carbon oxidation is then available from Equation 2.16.

2.2 THE *B* NUMBER IN FINITE RATE ABLATION MODELING

The behavior of the B number in equilibrium and nonequilibrium systems will now be investigated. The B number is first derived analytically, and then it is incorporated into the simplified ablation model derived in section 2.1.2, which is put into

nondimensional form. The model is validated using experimental data for graphite combustion, and the behavior of the equations is then explored in depth.

2.2.1 Definition and Derivation of the B Number

The B number, also called the mass transfer potential, is useful in describing thermochemical erosion rates in nondimensional terms. When ablation models with equilibrium and finite rate chemistry are compared, the discrepancies between the reported B numbers may be explained by examining the definition of B. The B number is derived in this section to give a full understanding of its origin, which will enable the discrepancies between the equilibrium and finite rate models to be explained clearly. More extensive analytical treatment of the B number may be found in [10-11, 15-16].

As in section 2.1.2, we consider only the oxidation of solid carbon by molecular oxygen (Equation 2.20). We approximate the boundary layer flow across the ablating surface as a Couette flow of thickness δ, as shown in Figure 2.5. The direction normal to the wall is defined as x and is positive out of the wall in this derivation. This is different from section 2.1.1, in which x was defined as positive into the solid. These two derivations are uncoupled, and no problem arises from the change in coordinate system.

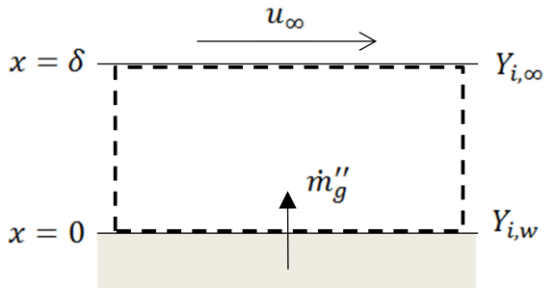

Figure 2.5: Couette flow approximation to boundary layer over an ablating surface.

For Couette flow, global conservation of mass reduces to $\dot{m}_x'' = const$, and since $\dot{m}_x''|_w = \dot{m}_g''$, we know that $\dot{m}_x'' = \dot{m}_g''$ everywhere within the boundary layer. The mass flux of a gaseous species i undergoing chemical reactions within the flow is governed by the species conservation equation, which for steady state Couette flow reduces to

$$\dot{m}_g'' \frac{dY_i}{dx} = \frac{d}{dx}\left(\rho_g D_i \frac{dY_i}{dx}\right) + \dot{m}_{i,rxn}''' \qquad 2.29$$

where D is the diffusion coefficient for a species and $\dot{m}_{i,rxn}'''$ is the volumetric generation rate of a species i through chemical reactions.

At $x = \delta$, the mass fractions assume their freestream values, $Y_{i,\infty}$. The boundary condition at the solid surface is more complicated, because it involves mass transfer from the condensed phase. Figure 2.6 shows a control volume for the solid phase, which includes both the surface and the solid material up to the T state.

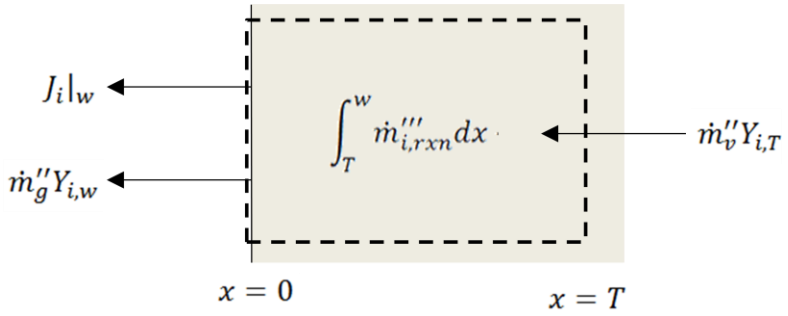

Figure 2.6: Control volume for surface boundary condition for Couette flow boundary layer.

This control volume is similar to Figure 2.3 on the gas side, but the solid phase contributions now include convection of mass in the virgin material and generation of mass volumetrically within the solid. The surface boundary condition for any species i is then defined as

$$\dot{m}_g'' Y_{i,w} + J_i|_w = \int_T^w \dot{m}_{i,rxn}''' dx + \dot{m}_v'' Y_{i,T} \qquad 2.30$$

or, using Fick's law of diffusion and Equation 2.16,

$$\dot{m}_g'' Y_{i,w} - \rho_g D_i \frac{dY_i}{dx}\bigg|_w = \int_T^w \dot{m}_{i,rxn}''' dx + \dot{m}_g'' Y_{i,T} \qquad 2.31$$

From reaction stoichiometry we can relate the $\dot{m}_{i,rxn}'''$ terms for the species in Equation 2.20 by

$$\dot{m}'''_{C,rxn} = r\dot{m}'''_{O_2,rxn} = -\frac{r}{1+r}\dot{m}'''_{CO,rxn} \tag{2.32}$$

This allows us to combine Equation 2.29 for $i = C$ with Equation 2.29 for $i = O_2$ to eliminate the $\dot{m}'''_{i,rxn}$ terms. Assuming that all species have equal diffusion coefficients, we obtain

$$\dot{m}''_g \frac{d}{dx}\left(Y_C - rY_{O_2}\right) = \frac{d}{dx}\left(\rho_g D \frac{d}{dx}\left(Y_C - rY_{O_2}\right)\right) \tag{2.33}$$

Performing the same combination on the condensed phase boundary condition (Equation 2.31) yields

$$\dot{m}''_g\left(Y_{C,w} - rY_{O_2,w}\right) - \rho_g D \frac{d}{dx}\left(Y_C - rY_{O_2}\right)\Big|_w = \dot{m}''_g\left(Y_{C,T} - rY_{O_2,T}\right) \tag{2.34}$$

or, more simply,

$$\dot{m}''_g\left[\left(Y_C - rY_{O_2}\right)_w - \left(Y_C - rY_{O_2}\right)_T\right] = \rho_g D \frac{d}{dx}\left(Y_C - rY_{O_2}\right)\Big|_w \tag{2.35}$$

We now define an intermediary variable b as

$$b = \frac{\left(Y_C - rY_{O_2}\right)}{\left(Y_C - rY_{O_2}\right)_w - \left(Y_C - rY_{O_2}\right)_T} \tag{2.36}$$

This variable can be used to simplify the conservation of species equation and both the condensed phase and freestream boundary conditions, yielding

$$\dot{m}''_g \frac{db}{dx} = \frac{d}{dx}\left(\rho_g D \frac{db}{dx}\right) \tag{2.37a}$$

$$x = 0: \qquad \dot{m}''_g = \rho_g D \frac{db}{dx}\Big|_w \tag{2.37b}$$

$$x = \delta: \qquad b = b_\infty = \frac{\left(Y_C - rY_{O_2}\right)_\infty}{\left(Y_C - rY_{O_2}\right)_w - \left(Y_C - rY_{O_2}\right)_T} \tag{2.37c}$$

Equation 2.37a can now be solved using the boundary conditions 2.37b and 2.37c. The first integration gives

$$\dot{m}''_g b = \rho_g D \frac{db}{dx} + const \tag{2.38}$$

Using boundary condition 2.37b yields

$$const = \dot{m}_g'' b_w - \rho_g D \left.\frac{db}{dx}\right|_w = \dot{m}_g''(b_w - 1) \tag{2.39}$$

which then gives

$$\dot{m}_g''(b - b_w + 1) = \rho_g D \frac{db}{dx} \tag{2.40}$$

Separating variables and integrating, assuming that $\rho_g D$ is constant throughout the boundary layer, we have

$$\ln(b - b_w + 1) = \frac{\dot{m}_g''}{\rho_g D} x + const \tag{2.41}$$

Evaluating the constant using boundary condition 2.37c yields

$$const = \ln(b_\infty - b_w + 1) - \frac{\dot{m}_g'' \delta}{\rho_g D} \tag{2.42}$$

and the final form

$$\frac{\dot{m}_g''}{\rho_g D}(\delta - x) = -\ln\left(\frac{b - b_w + 1}{b_\infty - b_w + 1}\right) \tag{2.43}$$

Of particular interest is the state at the surface of the condensed phase. With $b = b_w$ at $x = 0$, we have

$$\frac{\dot{m}_g'' \delta}{\rho_g D} = \ln(b_\infty - b_w + 1) \tag{2.44}$$

With this result, we may now introduce and examine the B number. The B number is defined as

$$B = b_\infty - b_w = \frac{\left(Y_C - rY_{O_2}\right)_\infty - \left(Y_C - rY_{O_2}\right)_w}{\left(Y_C - rY_{O_2}\right)_w - \left(Y_C - rY_{O_2}\right)_T} \tag{2.45}$$

This gives the simple result for the Couette flow boundary layer of

$$\frac{\dot{m}_g'' \delta}{\rho_g D} = \ln(B + 1) \tag{2.46}$$

The result just obtained states that, given a particular system (δ, $\rho_g D$), the rate of mass transfer is a function only of the B number (hence the mass transfer potential description), and that the rate of mass transfer increases monotonically with the B number. From Equation 2.45, we see that the mass transfer potential relates the

magnitudes of the quantity $Y_C - rY_{O_2}$ at the freestream, surface, and transferred substance states. This grouping is significant because it is a conserved quantity, meaning that the generation term in its species conservation equation (Equation 2.29) disappears, and it is only transported by convection and diffusion, never created or destroyed. Many other conserved quantities exist: concentrations of components in an inert mixture (as in an evaporation problem), concentrations of components in a reacting mixture that are related through stoichiometry (for the carbon oxidation reaction considered, the quantities $\left(Y_C - rY_{O_2}\right)$, $(Y_C + rY_{CO}/(1+r))$, and $\left(Y_{O_2} + Y_{CO}/(1+r)\right)$ are conserved), concentrations of elements in a mixture regardless of configuration (since atoms are not created or split apart), and total enthalpy (because energy is conserved). Each of these quantities obeys the same form of conservation equation and thus behaves similarly in the gas phase. The conservation equation and boundary conditions for any conserved quantity $\mathcal{P}$ for the Couette flow can then be formulated by examining Equation 2.37 as

$$\dot{m}_x'' \frac{d\mathcal{P}}{dx} = \frac{d}{dx}\left(\varphi \frac{d\mathcal{P}}{dx}\right) \tag{2.47a}$$

$$x = 0: \qquad \dot{m}_x'' = \frac{\varphi \left.\frac{d\mathcal{P}}{dx}\right|_w}{\mathcal{P}_w - \mathcal{P}_T} \tag{2.47b}$$

$$x = \delta: \qquad \mathcal{P} = \mathcal{P}_\infty \tag{2.47c}$$

and the B number is defined as

$$B \equiv \frac{\mathcal{P}_\infty - \mathcal{P}_w}{\mathcal{P}_w - \mathcal{P}_T} \tag{2.48}$$

The actual boundary layer flow is much more complex than the Couette flow described, and an analytical solution for B does not exist if the full boundary layer equations are considered. However, in the case of very low mass transfer rates compared to the rate of convection of the external flow, a Newton's law of cooling model may be used for the diffusive flux at the wall, and Equation 2.47b becomes

$$\dot{m}_g'' = \frac{h_m(\mathcal{P}_\infty - \mathcal{P}_w)}{\mathcal{P}_w - \mathcal{P}_T} \tag{2.49}$$

This gives the following formulation for the B number:

$$B = \frac{\dot{m}_g''}{h_m} \tag{2.50}$$

Because the Newton's Law of Cooling model is applicable in the limit of low mass transfer, Equation 2.50 should be recovered from Equation 2.46 as $\dot{m}_g'' \to 0$. From Equation 2.46, it is required that $B \to 0$ as $\dot{m}_g'' \to 0$ in order to bring the right side to zero. As $B \to 0$, a Taylor series expansion of $\ln(B+1)$ about 0 gives $\ln(B+1) \approx B$. Scaling also gives $h_m \sim \varphi/\delta \sim \rho_g D/\delta$ and Equation 2.50 is recovered. In cases of solid ablation, $\dot{m}_g''$ is sufficiently small that Equation 2.50 is accurate, and it is used throughout the present work.

We are now in a position to explain the differences observed between equilibrium and finite rate chemistry models used in ablation in terms of the B number. The B number, with $\mathcal{P} = Y_C - rY_{O_2}$, is

$$B = \frac{\left(Y_C - rY_{O_2}\right)_\infty - \left(Y_C - rY_{O_2}\right)_w}{\left(Y_C - rY_{O_2}\right)_w - \left(Y_C - rY_{O_2}\right)_T} \tag{2.51}$$

For oxidizing solid carbon, such as graphite, there is no carbon in the freestream, no oxygen in the solid, and no carbon vapor at the wall (because the vapor pressure of carbon is negligible at the temperatures encountered), so $Y_{C,\infty} = Y_{C,w} = Y_{O_2,T} = 0$. Additionally, carbon is the only constituent of graphite, so $Y_{C,T} = 1$. The B number reduces to

$$B = \frac{Y_{O_2,\infty} - Y_{O_2,w}}{Y_{O_2,w} + \frac{1}{r}} \tag{2.52}$$

At equilibrium, the concentration of oxygen at the surface is essentially zero, because the equilibrium constant K_P goes to ∞. The B number in this case is

$$B_{eq} = rY_{O_2,\infty} \tag{2.53}$$

When reactions are not sufficiently fast compared to transport processes for the equilibrium approach to be valid, the surface concentration of oxygen will be greater than zero, and in some cases may even be the same order of magnitude as the freestream concentration. The B number in this case is

$$B_{kin} = \frac{Y_{O_2,\infty} - Y_{O_2,w}}{Y_{O_2,w} + \frac{1}{r}} \leq B_{eq} \qquad 2.54$$

We can now see that the equilibrium formulation of the B number is an upper limit to its value, which from now on will be called B_{max}. When reaction times are short compared to transport times, B_{kin} will assume the value of B_{max}, but when reaction times are comparable to or long compared to transport times, B_{kin} will decrease from B_{max}, and calculations made using an equilibrium model will no longer be appropriate. This behavior will be observed over the course of this work in an experimental investigation of graphite oxidation and will be subsequently extended to the reentry scenario, with the intention of clarifying the expectable behavior that will be encountered in regimes for which the equilibrium approximation is not appropriate.

The equilibrium model for thermochemical ablation is discussed in Appendix A. The description follows that used in the Aerotherm Chemical Equilibrium (ACE) code [4]. Also included is a sample calculation for graphite in air. The results of this study are the equilibrium counterpart of the kinetic model for graphite oxidation being developed presently, and they will be used for comparison in modeling the reentry scenario in section 2.2.4.4.

2.2.2 Nondimensionalization

As with many thermal/fluids problems, the behavior of the carbon oxidation problem may be better understood by nondimensionalizing the governing equations of the simplified model. We choose to nondimensionalize the variables T_w and $Y_{O_2,w}$ by T_∞ and $Y_{O_2,\infty}$ to create nondimensional wall temperature (θ) and wall O_2 concentration (ϕ) as

$$\theta = \frac{T_w - T_\infty}{T_\infty} \qquad 2.55a$$

$$\phi = \frac{Y_{O_2,\infty} - Y_{O_2,w}}{Y_{O_2,\infty}} \qquad 2.55b$$

We also define a nondimensional activation energy as

$$\gamma = \frac{E_{a,O_2}}{\bar{R}T_\infty} \qquad 2.55c$$

Incorporating these nondimensionalized terms into Equation 2.23, and using Equation 2.22 to define $\dot{m}''_{O_2}$, the O_2 mass balance becomes

$$-\phi + \left[\frac{\rho_\infty Y_{O_2,\infty} A_{O_2}}{h_m Y_{O_2,\infty}}\right]\frac{(1-\phi)}{(\theta+1)} exp\left(\frac{-\gamma}{\theta+1}\right)\left(rY_{O_2,\infty}(1-\phi)+1\right) = 0 \qquad 2.56$$

and the energy balance becomes

$$-\theta + \left[\frac{\rho_\infty Y_{O_2,\infty} A_{O_2}}{hT_\infty/\Delta i_{comb,O_2}}\right]\frac{(1-\phi)}{(\theta+1)} exp\left(\frac{-\gamma}{\theta+1}\right) H + \frac{\alpha \dot{q}''_{ext}}{hT_\infty} - \frac{\varepsilon\sigma {T_\infty}^3}{h}\left((\theta+1)^4 - \left(\frac{T_{surr}}{T_\infty}\right)^4\right) = 0 \qquad 2.57a$$

where H is a nondimensional group that accounts for sensible enthalpy of the species involved in reaction and is defined as

$$H = 1 + \frac{1}{\Delta i_{comb,O_2}}\left[c_{p,O_2}\left(T_\infty(\theta+1) - T_{ref}\right) - c_{p,CO}\left(T_\infty(\theta+1) - T_{ref}\right)(1+r)\right] \qquad 2.57b$$

The dimensionless quantities in square brackets in Equations 2.56 and 2.57a can be interpreted as order-of-magnitude ratios between reaction and mass transport rates and between reaction and thermal transport rates, respectively. These ratios are traditionally defined as Damkohler numbers, and in our context we define

$$Da_M = \frac{\rho_\infty Y_{O_2,\infty} A_{O_2}}{h_m Y_{O_2,\infty}} \qquad 2.58a$$

$$Da = \frac{\rho_\infty Y_{O_2,\infty} A_{O_2}}{hT_\infty/\Delta i_{comb,O_2}} \qquad 2.58b$$

These two numbers are related because the heat transfer and mass transfer coefficients are analogous in the low mass transfer limit. For a flow with Lewis number = 1 (an appropriate approximation in this context) the coefficients are related by $h_m = h/c_{p,flow}$. The Damkohler numbers are then related by

$$\frac{Da}{Da_M} = \frac{h_m Y_{O_2,\infty}}{hT_\infty/\Delta i_{comb,O_2}} = \frac{Y_{O_2,\infty}\Delta i_{comb,O_2}}{c_{p,flow}T_\infty} \qquad 2.58c$$

The mass and energy balances become finally

$$-\phi + Da_M \frac{(1-\phi)}{(\theta+1)} exp\left(\frac{-\gamma}{\theta+1}\right)\left(rY_{O_2,\infty}(1-\phi)+1\right) = 0 \quad 2.59a$$

$$-\theta + Da \frac{(1-\phi)}{(\theta+1)} exp\left(\frac{-\gamma}{\theta+1}\right) H + \frac{\alpha \dot{q}''_{ext}}{hT_\infty} - \frac{\varepsilon\sigma {T_\infty}^3}{h}\left[(\theta+1)^4 - \left(\frac{T_{surr}}{T_\infty}\right)^4\right] = 0 \quad 2.59b$$

In the surface equilibrium limit, where reaction rates are very fast compared to transport, $Da = Da_M \to \infty$, and Equation 2.59a requires that $\phi \to 1$, or $Y_{O_2,w} \to 0$, which agrees with equilibrium calculations. In the other limit, where transport is very fast compared to reaction rates, $Da = Da_M \to 0$, and Equation 2.59a requires that $\phi \to 0$, or $Y_{O_2,w} \to Y_{O_2,\infty}$, which makes sense for a system in good contact with the O_2 reservoir.

One final manipulation puts the governing equations in the most favorable form for the subsequent discussion. Applying nondimensionalization to the definition of the low mass transfer B number (Equation 2.50) yields

$$B = B_{max}\left[Da_M \frac{(1-\phi)}{(\theta+1)} exp\left(\frac{-\gamma}{\theta+1}\right)\right] \quad 2.60$$

Incorporating this into the governing equations gives the final compact form

$$-\phi + \frac{B}{B_{max}}\left[B_{max}(1-\phi)+1\right] = 0 \quad 2.61a$$

$$-\theta + \frac{Da}{Da_M}\left(\frac{B}{B_{max}}\right) H + \frac{\alpha \dot{q}''_{ext}}{hT_\infty} - \frac{\varepsilon\sigma {T_\infty}^3}{h}\left[(\theta+1)^4 - \left(\frac{T_{surr}}{T_\infty}\right)^4\right] = 0 \quad 2.61b$$

Equations 2.60 and 2.61 are a general description of a reacting system in contact with an environmental reservoir, with surface chemistry described by Equation 2.60, mass exchange by Equation 2.61a, and energy exchange by Equation 2.61b. This set of equations is generally applicable to systems satisfying this description, which will allow prediction of ablation behavior based on calibration with a simple combustion scenario in the following sections.

2.2.3 Validation of Simplified Model with Graphite Oxidation Experiments

The simplified model was validated by comparison to the experiments of Matsui et al. [17], which were performed to investigate the effects of transport on the combustion of solid carbon. Experiments were performed for solid carbon combusting in a stagnation

flow with the temperature of the surface controlled by acetylene burners beneath the test apparatus, as shown in Figure 2.7. Both the surface temperature and the stagnation velocity gradient $2a$ were varied to obtain curves of combustion rate (mg/cm^2-s) versus surface temperature (K) for different values of the velocity gradient.

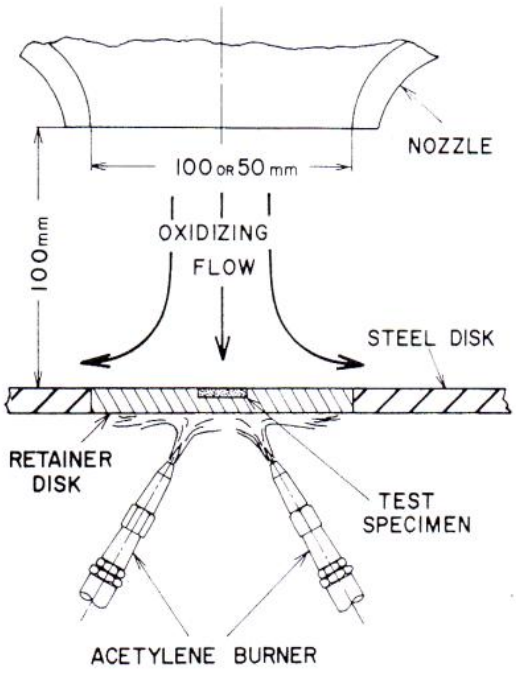

Figure 2.7: Experimental setup of Matsui et al., taken from [17].

Because of the generalized derivation of the governing equations, Equations 2.60 and 2.61 can be applied to the oxidizing stagnation flow experiments, with the external radiative flux $\alpha \dot{q}''_{ext}$ replaced by a general heat flux $\dot{q}''_{burner}$ provided by the acetylene burners. Matsui et al. determine experimental values for the activation energy and preexponential factor for the combustion of carbon with O_2, which are used in our model predictions. The activation energy of Matsui et al. compares well with that of later research, Tognotti et al. [18]. Values for these kinetic parameters, as well as other parameters used in this validation study, are tabulated in Table B.1 in Appendix B. The assumption that the reaction in Equation 2.20 is the only important reaction is also reasonable for the temperature range tested. The heat transfer coefficient h was

approximated using the similarity solution for axisymmetric stagnation flow, given by [19] as

$$h = k_{flow} G(Pr) \sqrt{\frac{a}{\nu_{flow}}} \approx k_{flow} (0.762 Pr^{0.4}) \sqrt{\frac{a}{\nu_{flow}}} \qquad 2.62$$

where ν is kinematic viscosity and the subscript $flow$ refers to the external boundary layer flow. Values of h are listed with their corresponding values of a in Table B.2 in Appendix B.

The simplified model was exercised across a range of $\dot{q}''_{burner}$ to produce the same range of T_w tested in the experiments, generating curves for each value of a tested. Experimental and modeling results for combustion rate as a function of wall temperature and stagnation velocity gradient are shown in Figure 2.8.

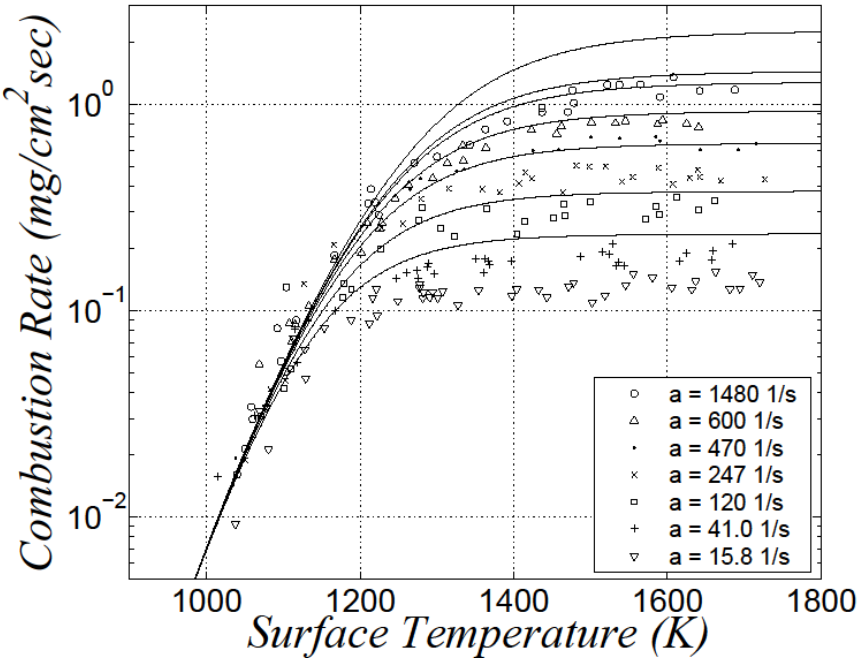

Figure 2.8: Combustion rate versus surface temperature for different values of stagnation velocity gradient.

Figure 2.8 shows clearly that the simplified model reproduces qualitatively the behavior observed in the experiments. At low temperatures, all curves converge to a

single line, and they break away at higher temperatures to assume constant values, with each value dependent upon the stagnation velocity gradient. In all cases, the simplified model over-predicts the combustion rate. Because the model contains many simplifications, particularly in the submodels for the heat transfer coefficient and the evaluation of properties, the model should not be expected to produce quantitative results with a high level of accuracy. It is clear that the majority of the relevant physical processes are accounted for in the simplified model, and more detailed modeling in the submodels should produce better quantitative agreement with data.

After acknowledging the limits in the quantitative accuracy of the simplified model in its raw form, the submodel for the heat transfer coefficient, which we are least confident in, was tuned to produce better agreement with the experimental results. It was found that by multiplying the heat transfer coefficient for all values of a by a factor of ½, excellent agreement was found with the experimental results, as shown in Figure 2.9. Values for the tuned heat transfer coefficients are also given in Table B.2.

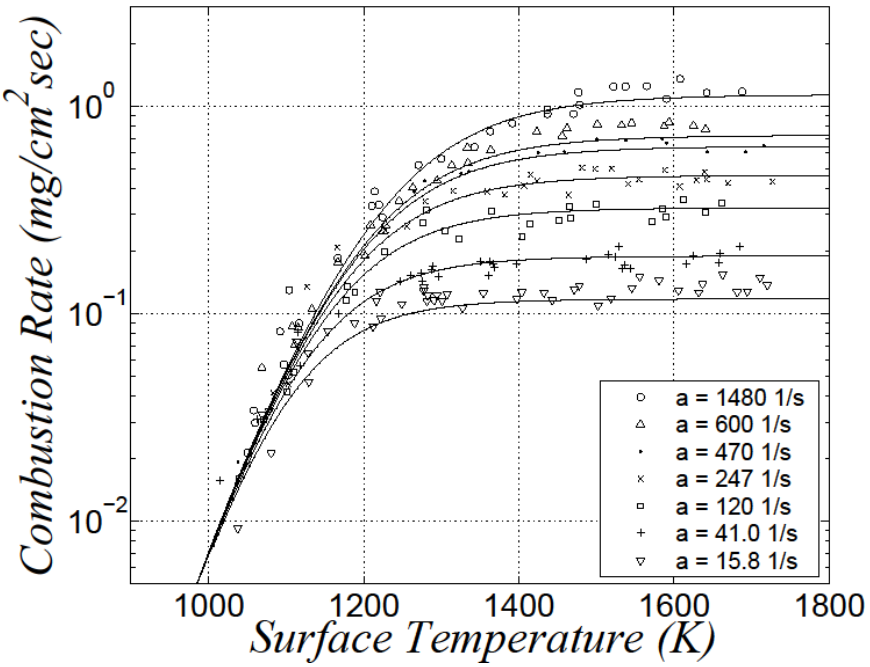

Figure 2.9: Combustion rate versus surface temperature for different values of stagnation velocity gradient, after adjustment of heat transfer coefficient.

The adjusted model works well for all values of a. The fact that these results were obtained by simply multiplying the heat transfer coefficient submodel by a proportionality constant indicates that bias exists somewhere in the full model (not necessarily just in the heat transfer coefficient submodel), and it is fortunate that the bias is so easily correctable.

The experimental comparison with the results of Matsui et al. shows that the simplified model is an excellent predictor of the qualitative behavior of ablation problems. Because the model is formulated for general cases of solid combustion, we are confident that qualitative conclusions reached with the simplified model in a combustion scenario should extend to more complex cases, such as the reentry problem. With sufficient validation of the simplified model, we now use it to draw conclusions about the behavior of ablating systems in equilibrium and nonequilibrium regimes.

2.2.4 Nonequilibrium Behavior in Thermochemically Ablating Systems: the Damkohler Number

There are many ways to interpret and analyze the B number in combustion scenarios. The following discussion explores the B number using a Damkohler number analysis, beginning first with nondimensionalization results obtained by Matsui et al. and then deepening the understanding of these results using the mass and energy balances. The conclusions drawn are then used to predict B number behavior in reentry scenarios.

2.2.4.1 Damkohler Analysis of Matsui et al.

The concept of the Damkohler number is well-utilized in combustion literature. The Damkohler number can be interpreted as a ratio between the characteristic time for chemical reactions and the characteristic time for thermal transport, or

$$Da \sim \frac{\tau_{transport}}{\tau_{reaction}} \qquad 2.63$$

Generally speaking, when reactions occur much faster than heat and mass transport, the Damkohler number tends toward ∞, and when transport is much faster than reactions, the Damkohler number tends toward 0. The Damkohler number is utilized effectively in ignition problems, where it identifies whether or not reactions are quick enough to

overcome energy loss rates and lead to thermal runaway, and in turbulent combustion, where it identifies whether or not reactions are quick enough to occur in the time allowed by flow processes.

For the solid combustion scenarios currently of interest, there are several options for definition of the Damkohler number. The first is that already defined in Equation 2.58, where Da and Da_M fall naturally out of the mass and energy balances due to nondimensionalization. Those Damkohler numbers are groupings of model constants and as such do not contain actual values for wall temperature and O_2 concentration, only reference values. Thus, they do not give a specific description of the actual surface chemistry, only of what it would be like under freestream conditions. This type of Damkohler formulation is therefore of limited use in directly predicting the behavior of the B number.

Matsui et al. define another Damkohler number in order to collapse their experimental data. They nondimensionalize the combustion rate using a characteristic flow velocity of $\left(2a\nu_{flow}\right)^{1/2}$ and obtain

$$M = \frac{\dot{m}_g''/\rho_g}{\left(2a\nu_{flow}\right)^{1/2}} = \frac{v_w}{\left(2a\nu_{flow}\right)^{1/2}} \qquad 2.64$$

They also formulate a Damkohler number, which we designate Da^*, as

$$Da^* = \frac{rA_{O_2}exp\left(-\frac{E_{a,O_2}}{\bar{R}T_w}\right)}{\left(2a\nu_{flow}\right)^{1/2}} \qquad 2.65$$

Da^* depends directly upon the wall temperature T_w, and thus includes the full contribution of the temperature-dependent part of the Arrhenius rate. It does not, however, contain any dependence upon the surface concentration of O_2, which also affects the overall reaction rate. Da^* thus shows the relative strengths of the temperature effect and the transport.

Figure 2.10 shows the data of Matsui et al. and the curves generated with the simplified model collapsed using M and Da^*. The collapse is excellent for the data, showing that M and Da^* are important nondimensional groups in the solid combustion

problem. The lines generated using the simplified model also collapse and agree well with the data, showing that the simplified model is indeed an appropriate description of the physics involved.

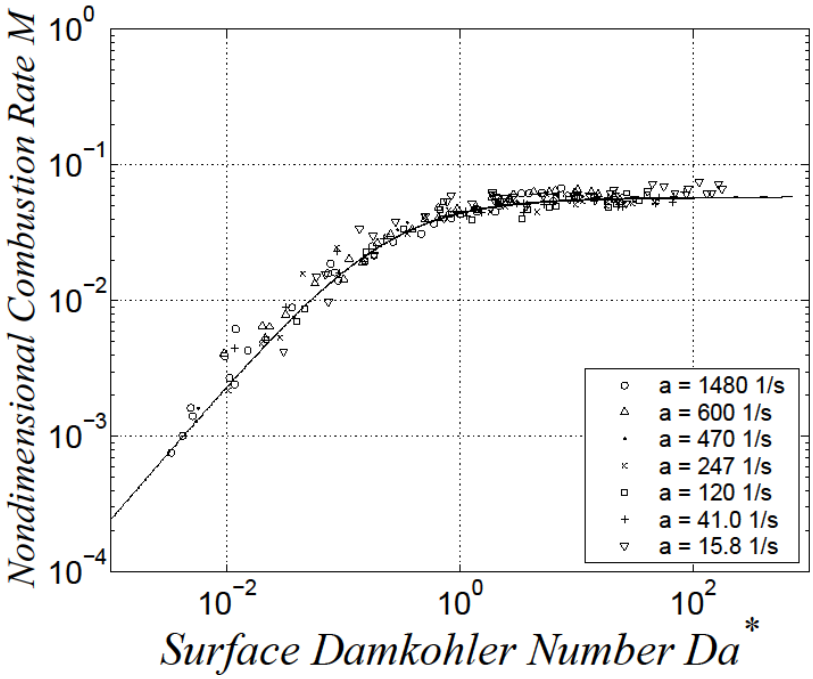

Figure 2.10: Data of Matsui et al. and model prediction collapsed using M and Da^*.

The nondimensional combustion rate M is essentially the B number, and in the present context it is beneficial to reformulate the results of Figure 2.10 in terms of the B number, as shown in Figure 2.11. The resulting curves are essentially proportional to those of Figure 2.10, showing that M and B are equivalent. The B curves asymptotically approach the value $B = 0.174$, which from Equation 2.53 is the value for B_{max}:

$$B_{max} = rY_{O_2,\infty} = Y_{O_2,\infty}\left(\frac{\nu_C W_C}{\nu_{O_2} W_{O_2}}\right) = 0.174 \qquad 2.66$$

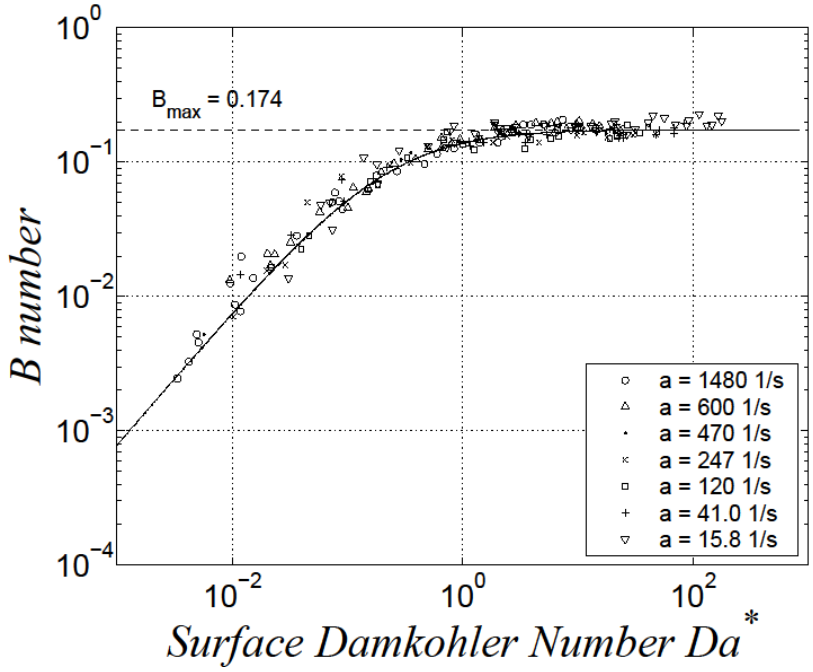

Figure 2.11: Data of Matsui et al. and model prediction collapsed using B and Da^*.

The utility of the Damkohler number is now apparent. At high Da^*, reaction rates are very high compared to transport rates, and the surface reactions go to their equilibrium value, which is B_{max}. At low Da^*, transport rates are high relative to reaction rates, and O_2 is transported to the surface quickly enough that it can accumulate in appreciable quantities. B thus decreases from the equilibrium value, as predicted by Equation 2.54:

$$B_{kin} = \frac{Y_{O_2,\infty} - Y_{O_2,w}}{Y_{O_2,w} + \frac{1}{r}} \leq B_{max} \qquad 2.54$$

Additional insight can be obtained by plotting the results of B vs. Da^* on a linear ordinate, as shown in Figure 2.12. We now see B asymptotically approaching B_{max} as $Da^* \to \infty$ and asymptotically approaching 0 as $Da^* \to 0$, with a smooth transition region between the two extremes. We therefore identify three regions: a diffusionally controlled regime for $Da^* \gtrsim 10^1$ in which reactions are fast relative to transport, a kinetically controlled regime for $Da^* \lesssim 10^{-2}$ in which transport is fast relative to reactions, and a

transition regime for $10^{-2} \lesssim Da^* \lesssim 10^{1}$ in which the rates of both processes are comparable.

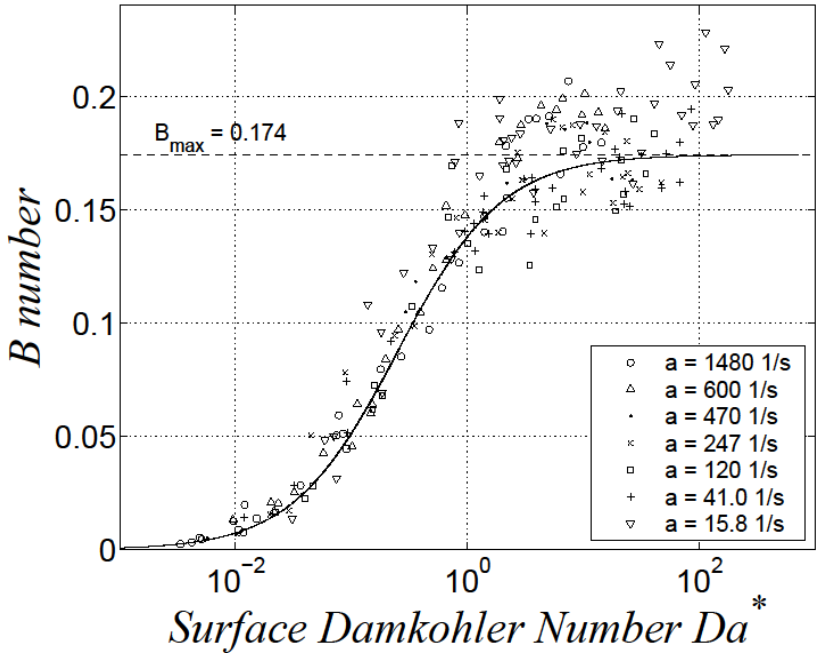

Figure 2.12: B and Da^*, showing three regions of behavior.

2.2.4.2 Mass Balance Considerations

The results obtained through nondimensionalization using B and Da^* are encouraging, but the formulation for Da^* includes no influence from the surface O_2 concentration, and it is strange that such good collapse is obtained from a seemingly arbitrary quantity. Insight can be gained by examining the formulation for the nondimensional combustion rate, M, of Matsui et al. They define the mass loss rate, $\dot{m}_g''$, as

$$\dot{m}_g'' = \rho_g Y_{O_2,w} A_{O_2} exp\left(-\frac{E_{a,O_2}}{\bar{R}T_w}\right)\left(\frac{\nu_C W_C}{\nu_{O_2} W_{O_2}}\right) \qquad 2.67$$

which, when combined with Equation 2.64 gives

$$M = \frac{\rho_g Y_{O_2,w} A_{O_2} exp\left(-\frac{E_{a,O_2}}{\bar{R}T_w}\right)\left(\frac{\nu_C W_C}{\nu_{O_2} W_{O_2}}\right)}{\rho_g \left(2a\nu_{flow}\right)^{1/2}} = Y_{O_2,w} Da^* \qquad 2.68$$

Because collapse is obtained when M and Da^* are plotted, this suggests that a relationship may exist between M, or equivalently B, and $Y_{O_2,w}$.

This relationship is obtained from the nondimensionalized mass balance, Equation 2.61a:

$$-\phi + \frac{B}{B_{max}}[B_{max}(1-\phi)+1] = 0 \qquad 2.61a$$

Rearrangement of this gives an explicit formulation for B in terms of only one variable, ϕ:

$$\frac{B}{B_{max}} = \frac{\phi}{B_{max}(1-\phi)+1} \qquad 2.69$$

B/B_{max} increases monotonically with ϕ from 0 at $\phi = 0$ to 1 at $\phi = 1$, with curvature related to the magnitude of B_{max}. Figure 2.13 shows this relationship for the solid combustion scenario, showing both the simplified model and the data of Matsui et al. Again, the model compares well with experimental data.

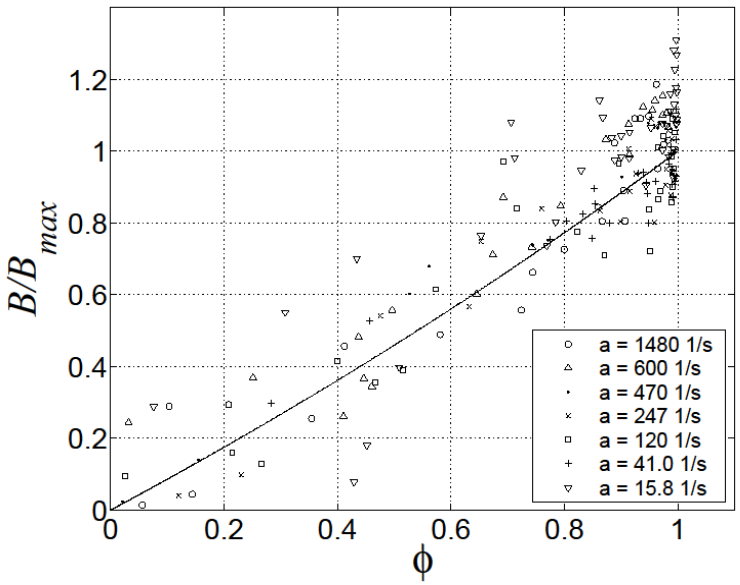

Figure 2.13: B/B_{max} vs. ϕ, experimental data and model prediction.

In the low mass transfer limit, valid for solid combustion scenarios, $B_{max} \ll 1$, and the term $B_{max}(1-\phi)$ is much less than 1. B/B_{max} is therefore nearly linear in ϕ, and we obtain the important relation

$$\frac{B}{B_{max}} \approx \phi \tag{2.70}$$

Both the data and model in Figure 2.13 show this relationship. Physically, this relationship means that the mass transfer by blowing is negligible, and the important balance is between reaction and diffusion.

The existence of a relationship between B and ϕ shows why it is unnecessary to include ϕ in the definition of the Damkohler number, as the dependence of B reduces from $B = func(\phi, \theta)$ to $B = func(\theta)$. The elimination of ϕ from the formulation for B is done by isolating ϕ in Equation 2.50:

$$\begin{aligned} B = \frac{\dot{m}_g''}{h_m} &= \frac{r\left[\rho_g Y_{O_2,w} A_{O_2} exp\left(-\frac{E_{a,O_2}}{\bar{R}T_w}\right)\right]}{h_m} \\ &= B_{max}\frac{\rho_g A_{O_2} exp\left(-\frac{E_{a,O_2}}{\bar{R}T_w}\right)}{h_m}(1-\phi) \end{aligned} \tag{2.71}$$

We now define one final Damkohler number,

$$\overline{Da} = \frac{\rho_g A_{O_2} exp\left(-\frac{E_{a,O_2}}{\bar{R}T_w}\right)}{h_m} \tag{2.72}$$

which is very similar to that defined by Matsui et al. We obtain the result

$$\frac{B}{B_{max}} = \overline{Da}(1-\phi) \tag{2.73}$$

Substituting using Equation 2.70 gives the final result

$$\frac{B}{B_{max}} \approx \frac{\overline{Da}}{1+\overline{Da}} \tag{2.74}$$

This is an extremely useful result because it defines the B number explicitly and exclusively in terms of a nondimensional Damkohler number. Equation 2.74 is plotted with the simplified model and the experimental data of Matsui et al. in Figure 2.14. As

shown, the simplification of Equation 2.74 introduces minimal error to the results of the simplified model and allows the B number to be determined by only one variable, T_w. Furthermore, T_w is generally available from experiments, so the B number and hence the recession rate for a surface are now easily obtainable from measurement of only the wall temperature.

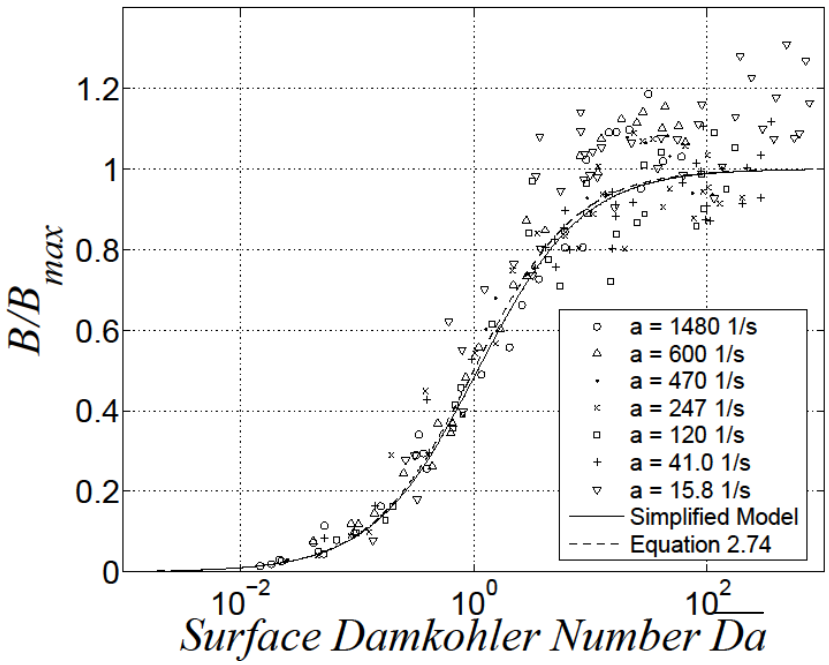

Figure 2.14: B/B_{max} vs $\overline{Da}$, along with Equation 2.74.

We again identify three regimes by examination of Figure 2.14: a diffusionally controlled regime for $\overline{Da} \gtrapprox 10^2$, a kinetically controlled regime for $\overline{Da} \lessapprox 10^{-2}$, and a transition regime for $10^{-2} \lessapprox \overline{Da} \lessapprox 10^2$. From these results, we see that $\overline{Da}$ is a very good choice for the Damkohler number for solid combustion. It centers the curve around $\overline{Da} = 1$, which is pleasing, and more importantly, it is a product of the governing equations and hence has more foundation than a Damkohler number created to collapse experimental data.

In the case of Matsui et al., the correct form of the Damkohler number was chosen ($Da^* = Da^*(T_w)$ only) without addressing the governing equations. The previous analysis shows why this form is correct and explains why it was so successful in collapsing experimental data. Slightly modifying Da^* to obtain $\overline{Da}$ shifts the curve to obtain the more elegant result centered around $\overline{Da} = 1$.

A result similar to Equation 2.74 was obtained by [20] for the combustion of carbon spheres. The result was obtained by merging asymptotic expressions for the diffusionally and kinetically controlled regimes.

2.2.4.3 Energy Balance Considerations

The simple $\overline{Da}$ model (Equation 2.74) was obtained from Equations 2.60 and 2.61a without consideration of the energy balance, Equation 2.61b, which we examine now. Nondimensionalizing $\overline{Da}$ in terms of θ and ϕ gives

$$\overline{Da} = Da_M(\theta+1)^{-1} exp\left(\frac{-\gamma}{\theta+1}\right) \tag{2.75}$$

Inserting this with the $\overline{Da}$ model into Equation 2.61b gives

$$-\theta + \frac{Da}{Da_M}\left(\frac{Da_M(\theta+1)^{-1} exp\left(\frac{-\gamma}{\theta+1}\right)}{1 + Da_M(\theta+1)^{-1} exp\left(\frac{-\gamma}{\theta+1}\right)}\right) H + \frac{\alpha \dot{q}''_{ext}}{hT_\infty} - \frac{\varepsilon\sigma {T_\infty}^3}{h}\left[(\theta+1)^4 - \left(\frac{T_{surr}}{T_\infty}\right)^4\right] = 0 \tag{2.76}$$

which is in terms of one variable, θ. The solution to the problem may now be reduced to the solution of one extremely implicit equation for θ, with other quantities of interest such as B, $\dot{m}''_g$, and $Y_{O_2,w}$ calculated afterwards.

2.2.4.4 Extension to Reentry Scenario

The conclusions obtained in the previous analysis have important consequences for the reentry scenario. The simplified model is adjusted to simulate the reentry scenario by setting $\dot{q}''_{ext}$ to zero and by varying the freestream temperature to represent shock heating of the freestream gases. Although dissociation of O_2 and N_2 will occur in realistic scenarios, qualitative results are obtained by continuing to consider only the

single oxidation reaction used previously. Figure 2.15 shows curves for B vs. T_w with varying h, generated by varying T_∞ over a wide range. Also shown is the equilibrium solution generated in Appendix A using the ACE code.

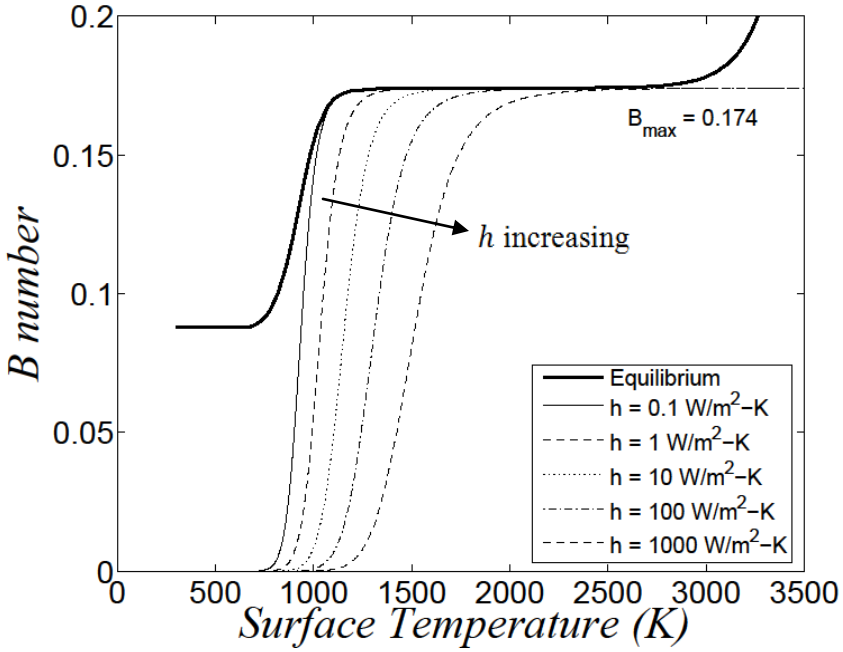

Figure 2.15: B vs. T_w for reentry scenario with varying values of h and T_∞.

First, let us consider the case in which the equilibrium and finite rate solutions converge, which is the limit as $h \to 0$. This case is approximated by the curve for $h = 0.1$ W/m^2-K. Figure A1 in Appendix A shows that carbon monoxide ceases to be generated around 1000 K; this is accounted for by both the kinetic and equilibrium models. However, the equilibrium model replaces the product carbon monoxide with carbon dioxide, and a new, nonzero plateau at $B = 0.087$ occurs. This is not accounted for in the kinetic model because only the reaction to form CO is considered, and the B number goes to zero. The kinetic model should therefore not be used in this case below temperatures of around 1000 K because its physics has not been validated below this temperature.

As the heat transfer coefficient increases, the kinetic and equilibrium results diverge. The kinetic curves fall off from the equilibrium result as kinetically controlled behavior takes over, and for the same surface temperature, the equilibrium model always produces a higher value of B than the kinetic model. Thus, at low temperatures and high h, the equilibrium model overpredicts the recession rate. It is important to note that the equilibrium solution produces only one value for B for a given T_w, but the kinetic model produces a range of values between zero and B_{max} for a given T_w as h is varied. It should also be noted that the kinetic model does not reproduce the sublimation behavior beginning around 2700 K because this reaction is not modeled.

The nonequilibrium behavior of the kinetic model curves in Figure 2.15 can be collapsed using the Damkohler number, $\overline{Da}$, as shown in Figure 2.16. Also shown is the $\overline{Da}$ model, Equation 2.74, which is almost indistinguishable from the curves for the simplified model. It is now apparent that the low temperature behavior can be described completely in terms of $\overline{Da}$, as can the transition to equilibrium behavior.

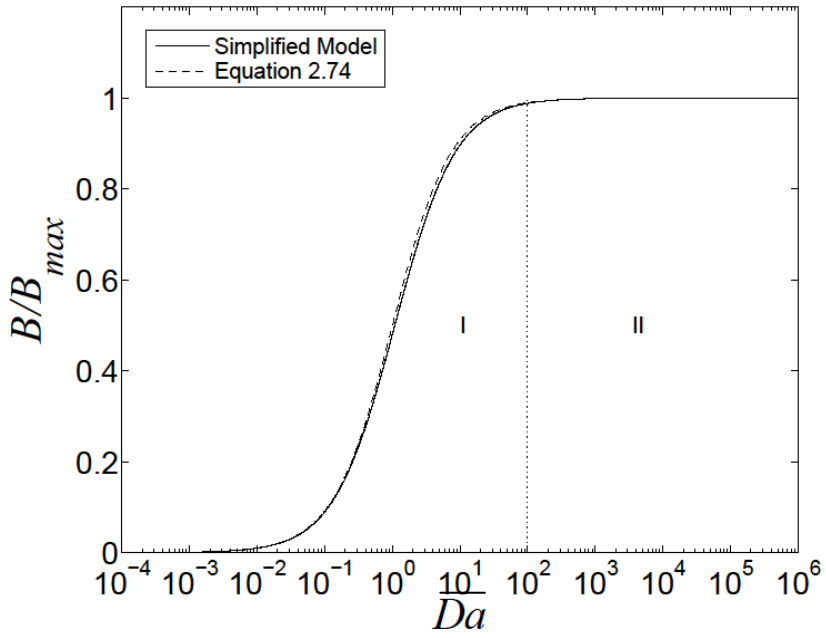

Figure 2.16: Reentry scenario collapsed in terms of $\overline{Da}$, showing kinetically controlled regime (I) and diffusionally controlled regime (II).

Using these results, we can identify three regions in ablating systems. The first, for $\overline{Da} \lesssim 10^2$ in this context, is the kinetically controlled regime, where the B number is related to T_w by Equation 2.74 and the specific (T_w, B) pair is determined based on the overall energy balance, Equation 2.61b or 2.76. The second region, for $\overline{Da} \gtrsim 10^2$ but with T_w low enough that sublimation does not occur, is the diffusionally controlled regime, where $B = B_{max}$, the equilibrium value. For simple scenarios such as graphite combustion, where the equilibrium constant $K_P \to \infty$, this is a constant, as shown in Figure 2.15. In this region, $B/B_{max} = 1$, and Equation 2.61b reduces to

$$-\theta + \frac{Da}{Da_M} H + \frac{\alpha \dot{q}''_{ext}}{hT_\infty} - \frac{\varepsilon \sigma {T_\infty}^3}{h}\left[(\theta+1)^4 - \left(\frac{T_{surr}}{T_\infty}\right)^4\right] = 0 \qquad 2.77$$

which is just a polynomial equation for θ. The third region, not shown in Figure 2.16, is the sublimation controlled regime, where T_w is high enough for carbon to sublimate. This reaction was not included in the simplified model, and thus cannot be described in terms of Damkohler numbers for surface oxidation. It should be noted that the definition of the kinetically controlled regime here differs from that for Figure 2.14. In the context of ablation, it makes sense to talk about kinetically controlled behavior as any behavior that deviates from equilibrium behavior due to Damkohler number effects, so the kinetically controlled regime for ablation includes both the kinetically controlled and transition regimes of Figure 2.14.

While peak heating during a reentry trajectory is generally in the diffusion or sublimation controlled regime, much of the heating up or cooling down phases on either side of peak heating may contain Damkohler numbers low enough to enter the kinetically controlled regime. During these time periods, which may add up to a significant portion of the total flight time, an equilibrium model will overpredict B and thus overpredict the total recession rate, leading to overdesign of systems in which overall weight is a very important parameter. It is therefore valuable and important to consider the behavior within the kinetically controlled regime. The behavior of the system in this regime is governed by Equations 2.74 through 2.76. Reorganization of Equation 2.76 reveals the nondimensional groups which govern behavior in the kinetically controlled regime:

$$-\theta + Da\left(\frac{(\theta+1)^{-1}exp\left(\frac{-\gamma}{\theta+1}\right)}{1/Da_M + (\theta+1)^{-1}exp\left(\frac{-\gamma}{\theta+1}\right)}\right)H + \frac{\alpha\dot{q}''_{ext}}{hT_\infty} - \frac{\varepsilon\sigma{T_\infty}^3}{h}\left[(\theta+1)^4 - \left(\frac{T_{surr}}{T_\infty}\right)^4\right] = 0 \quad \text{2.78a}$$

$$H = 1 + \left[\left(\frac{c_{p,O_2}T_\infty}{\Delta i_{comb,O_2}}(\theta+1) - \frac{c_{p,O_2}T_{ref}}{\Delta i_{comb,O_2}}\right) - (1+r)\left(\frac{c_{p,CO}T_\infty}{\Delta i_{comb,O_2}}(\theta+1) - \frac{c_{p,CO}T_{ref}}{\Delta i_{comb,O_2}}\right)\right] \quad \text{2.78b}$$

These groups are the Damkohler numbers Da and Da_M, the nondimensional activation energy γ, the ratio of external heat flux to convective heat transfer $\alpha\dot{q}''_{ext}/hT_\infty$, the ratio of surface radiation exchange to convective heat transfer $\varepsilon\sigma{T_\infty}^3/h$, the ratio of the surroundings temperature to the freestream temperature T_{surr}/T_∞, and terms relating sensible enthalpy to the enthalpy of combustion of the form $c_pT/\Delta i_{comb,O_2}$. We can therefore say that in the kinetically controlled regime for ablating graphite, the temperature of the ablating surface, and thus the mass loss rate, are governed by

$$\dot{m}'' = \dot{m}''\left(Da, Da_M, \gamma, \frac{\alpha\dot{q}''_{rad}}{hT_\infty}, \frac{\varepsilon\sigma{T_\infty}^3}{h}, \frac{T_{surr}}{T_\infty}, \frac{c_pT}{\Delta i_{comb,O_2}}\right) \quad \text{2.79}$$

2.2.4.5 Extension to More Complex Systems

The graphite oxidation case discussed in this work is simple enough to lend itself to analytical treatment, but most applications of engineering interest are more complex and may include physics such as internal pyrolysis, multiple surface reactions, and mechanical erosion. As demonstrated in section 2.1.1, these scenarios are still describable in terms of energy, mass, momentum, and species conservation equations, but analytical results and simple scaling-type laws are often very difficult to obtain. Appendix C includes an attempt to begin analytical treatment of more complex systems. The approach has not been validated, and the author is not sure if the results are correct. The information in Appendix C should therefore be treated with skepticism and has been included as a reference and starting point in case future work is done in this area.

2.3 CONCLUSIONS

The transition between diffusionally controlled and kinetically controlled behavior in thermochemically ablating systems can be described successfully in terms of the B number and the Damkohler number. In particular, use of the Damkohler number $\overline{Da}$ formulated herein leads to the simple relationship $B/B_{max} = \overline{Da}/(1 + \overline{Da})$ for solid carbon oxidation by molecular oxygen. This result fits data from solid carbon combustion experiments very well.

In the reentry scenario, a value of $\overline{Da} \approx 10^2$ marks the transition between the diffusionally controlled and kinetically controlled regimes for graphite ablators in the absence of sublimation. Above this value, equilibrium models are appropriate for ablation analysis, but below this value, they will significantly overpredict the recession rate.

In the kinetically controlled regime for graphite oxidation, the surface temperature and recession rate are governed by the following nondimensional parameters: Da, Da_M, γ, $\alpha\dot{q}''_{rad}/hT_\infty$, $\varepsilon\sigma{T_\infty}^3/h$, T_{surr}/T_∞, and $c_pT/\Delta i_{comb,O_2}$. Opportunity exists for future work in investigating those parameters not addressed herein, such as $\alpha\dot{q}''_{rad}/hT_\infty$, and $\varepsilon\sigma{T_\infty}^3/h$, in order to gain more understanding of the nonequilibrium behavior of thermochemically ablating systems.

Chapter 3: Mechanical Erosion in Thermochemically Degrading Systems

Although purely thermochemical modeling of ablating TPS systems is sufficient in many reentry scenarios, there is a collection of scenarios for which mechanical forces may cause the removal of solid particles, augmenting the overall recession rate. For these scenarios, purely thermochemical modeling is inadequate for describing the system, and models for mechanical erosion, or spallation, must be implemented.

The participation of mechanical forces in the degradation of ablative thermal protection systems has been observed since the adoption of these systems in the late 1950s. A considerable amount of observational and experimental evidence has accumulated since then to support this early hypothesis, and a large body of experimental and theoretical work now exists indicating that under the proper flight conditions, mechanical spallation produces a non-negligible contribution to the overall surface recession rate. This work has been produced not only by NASA and its collaborators but also by scientific organizations in other nations.

Experimental evidence for spallation was presented by Schneider et al. in 1968 [21], wherein an ablation test was performed for carbon phenolic under conditions of high surface shear and compared to a thermochemical erosion model. In this analysis it was found that purely chemical erosion contributed only one third of the total material erosion and that a thermo-chemo-mechanical erosion model compared reasonably well with test data. In 1982, Lundell [22] performed gasdynamic laser tests on carbon phenolic at NASA Ames Research Center and measured the total and spallation-only mass loss rates. These data were correlated and applied to two Jovian atmospheric re-entry simulations, and modeling predicted that the mass loss rates due to spallation would be 7.4% and 10% of the thermochemical loss rates. In 1999, Yoshinaka et al. [23] performed ablation tests on carbon phenolic at the Japan Ultra-high Temperature Material Research Center and at the National Aerospace Laboratory. Using spectroscopic measurements, they identified carbonaceous species in the external flow field and

attributed their presence to spallation, not diffusion. Later, in 2004, Raiche et al. [24] performed similar tests on PICA at NASA Ames Research Center and observed that a He-Ne laser beam is attenuated inside the shock layer in the presence of an ablating material. Park [25] attributed this behavior to the presence of spalled particles in the freestream and determined a range of likely spallation rates based on heat flux; these rates are non-negligible compared to thermochemical erosion rates.

In response to the discovery of the spallation phenomenon, numerous mechanical erosion models have been proposed based on the idea of high frequency small particle removal [26-28] and the low frequency ejection of large particle bundles [21, 29]. A particularly instructive example is given by Schneider et al., in which spallation is proposed to occur for carbon phenolic by thermal or internal pressure fracture between composite layers and the subsequent removal of these individual layers by internal pressure and aerodynamic shear forces. An experiment was performed in which a rotor was used to periodically subject a set of test cylinders of carbon phenolic to high heat flux and surface shear stress. The experiment was then simulated using the constructed thermo-chemo-mechanical ablation model, and the results were compared to the collected experimental data. The purely thermochemical model was shown to significantly underpredict the recession rate, while the thermo-chemo-mechanical model agreed well with the data. The validated model was then used to simulate a realistic re-entry scenario. In this situation, spallation contributed significantly to the overall recession rate, more than doubling the total amount of material removed.

Mechanical erosion models have historically been material-specific, and because the mechanical erosion mechanism is very dependent upon the geometry of the TPS material, some loss of generality is unavoidable in modeling. In this chapter, we attempt to explore the mechanical erosion mechanism as broadly as possible. First, the effect of mechanical loss in a chemically eroding system is investigated generally by considering a simple solid combustion reaction with grinding, and generally expectable behaviors are identified. Next, a model for the mechanical erosion rate is proposed and incorporated into the ablation model developed in section 2.1.2, and conclusions are drawn. Finally, a

physics-based mechanical erosion model is developed and coupled to the ablation model, and the inclusion of mechanical erosion in thermochemically ablating systems is explored in depth.

3.1 SOLID COMBUSTION WITH GRINDING

The process of mechanical erosion in the reentry scenario is extremely complex, and it is useful to begin exploration of the process by identifying general trends in a more simplified thermo-chemo-mechanical ablation scenario. We consider a solid material subject to a prescribed radiative heat flux $\dot{q}''_{ext}$ and a mechanical grinding process on the surface, and we consider the steady-state mass loss of this material, which loses mass due to chemical reaction and mechanical erosion at a rate $\dot{m}''_{tot} = \dot{m}''_{chem} + \dot{m}''_{mech}$. It is assumed that the surface temperature is high enough for diffusionally limited combustion to occur, in which case $\dot{m}''_{chem} = h_m B_{max}$.

At steady state, the energy equation for the solid with a total mass loss rate of $\dot{m}''_{tot}$ is

$$\frac{d^2T}{dx^2} + \frac{\dot{m}''_{tot} c_p}{k}\frac{dT}{dx} = 0 \tag{3.1}$$

The energy balance across the surface, neglecting the enthalpy of the oxidizer and product gases relative to the enthalpy of combustion Δi_{comb}, is

$$\dot{q}''_{ext} + \dot{m}''_{chem}\Delta i_{comb} = -k\frac{dT}{dx}\bigg|_{x=0} \tag{3.2}$$

Rearrangement of this equation gives the boundary condition at $x = 0$:

$$\frac{dT}{dx}\bigg|_{x=0} = -\left[\frac{\dot{q}''_{ext} + h_m B_{max}\Delta i_{comb}}{k}\right] \tag{3.3a}$$

Additionally, the solid is assumed semi-infinite, so the second boundary condition is

$$\lim_{x\to\infty} T = T_o \tag{3.3b}$$

where T_o is the temperature of the thermally unaffected solid.

The solution to this equation is

$$T - T_o = \left[\frac{\dot{q}''_{ext} + h_m B_{max} \Delta i_{comb}}{(h_m B_{max} + \dot{m}''_{mech}) c_p}\right] exp\left(-\frac{c_p}{k}(h_m B_{max} + \dot{m}''_{mech})x\right) \qquad 3.4$$

Solution curves for different values of $\dot{m}''_{mech}$ are shown in Figure 3.1. It can be seen that, when increasing the value of $\dot{m}''_{mech}$, the total mass loss rate increases, the surface temperature decreases, and the thickness of the thermal penetration depth decreases $(\delta_t \sim k/\dot{m}''_{tot} c_p)$. We will look for the preservation of these features in more complex modeling in the following sections.

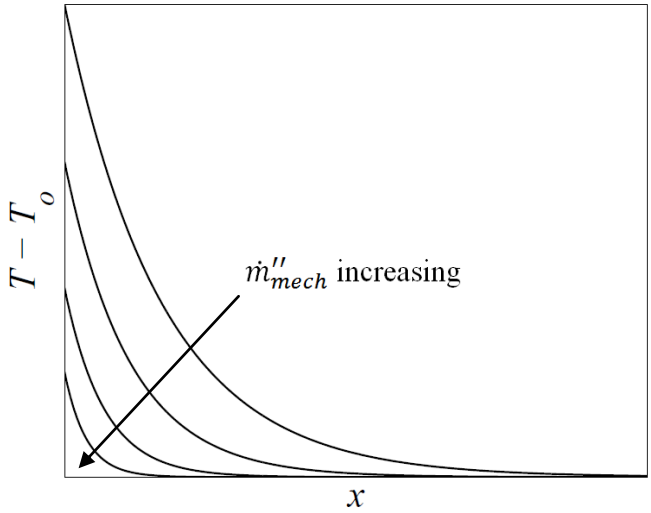

Figure 3.1: Solid temperature profiles for solid combustion with grinding.

3.2 A PROTOTYPE FOR MECHANICAL EROSION MODELING IN A REENTRY SCENARIO

The next step towards a physics-based model for spallation in a reentry scenario is to propose a prototype model for mechanical erosion and observe its effects on the system. This model, while not based directly on physics at the surface of the ablator, is still useful for observing in general the response of the system to the new phenomenon.

The proposed model for mechanical erosion defines the erosion rate as

$$\dot{m}''_{mech} = \tau^* A_{mech} exp\left(-\frac{T_{mech}}{T_w}\right) \qquad 3.5$$

where τ^* is the dimensionless ratio of the surface shear stress to a reference shear stress ($\tau^* = \tau_s/\tau_{ref}$), A_{mech} is a preexponential factor, and T_{mech} is a characteristic temperature for mechanical erosion. Thus, the proposed model states that the erosion rate depends linearly on surface shear stress (because increased surface drag can break off larger pieces of material) and on surface temperature in an Arrhenius fashion (because increased surface temperature could lead to a decrease in material strength).

This model is introduced into the graphite oxidation problem discussed in section 2.1.2. The oxygen mass balance is unchanged from Equation 2.23:

$$h_m\left(Y_{O_2,w} - Y_{O_2,\infty}\right) + \dot{m}''_{O_2} r Y_{O_2,w} + \dot{m}''_{O_2} = 0 \qquad 2.23$$

The energy balance (Equation 2.24) now includes enthalpy terms for spallation flux at the wall and at the transferred substance state:

$$\begin{aligned} -h(T_w - T_\infty) + \dot{m}''_{O_2} i_{O_2}\big|_w - \dot{m}''_{O_2}(1+r) i_{CO}|_w + \left[\dot{m}''_{O_2} r + \dot{m}''_{mech}\right] i_v|_T \\ - \dot{m}''_{mech} i_C|_w + \alpha \dot{q}''_{ext} - \varepsilon\sigma\left({T_w}^4 - {T_{surr}}^4\right) = 0 \end{aligned} \qquad 3.6$$

Nondimensionalization of these equations results in the following for the mass and energy balances, respectively:

$$-\phi + Da_M \frac{(1-\phi)}{(\theta+1)} exp\left(\frac{-\gamma}{\theta+1}\right)\left(B_{max}(1-\phi)+1\right) = 0 \qquad 3.7a$$

$$\begin{aligned} -\theta + Da \frac{(1-\phi)}{(\theta+1)} exp\left(\frac{-\gamma}{\theta+1}\right) H + \frac{\alpha \dot{q}''_{ext}}{hT_\infty} \\ - \frac{\varepsilon\sigma {T_\infty}^3}{h}\left[(\theta+1)^4 - \left(\frac{T_{surr}}{T_\infty}\right)^4\right] - Sp\ exp\left(\frac{-\gamma_{sp}}{\theta+1}\right) H_{sp} = 0 \end{aligned} \qquad 3.7b$$

where

$$\gamma_{sp} = \frac{T_{sp}}{T_\infty}, \qquad H_{sp} = \frac{c_{p,C}[T_\infty(\theta+1) - T_T]}{\Delta i_{comb,O_2}}, \qquad Sp = \frac{\tau^* A_{sp}}{hT_\infty/\Delta i_{comb,O_2}}$$

The parameters γ_{sp} and H_{sp} are similar to their counterparts γ and H in the oxidation reaction, and Sp may be called a spallation number and loosely indicates the ratio between mass loss by spallation and heat transport by convection.

The nondimensionalized equations (3.7) were solved for a reentry scenario, with $\dot{q}''_{ext}$ set to zero and T_∞ varied over a wide range. The kinetic parameters for oxidation

provided by Matsui et al. [17] were used, and the mechanical erosion parameters A_{mech} and T_{mech} were adjusted so that the rates of mass loss by spallation and oxidation would be approximately equal at $\tau^* = 1$. The final values used for these parameters are A_{mech} = 0.1 kg/m^2-s and T_{mech} = 1500 K.

To report the results for mass loss with mechanical erosion, it is necessary to clarify the description of the B number. The B number, as defined for the low mass transfer limit, is

$$B = \frac{\dot{m}_g''}{h_m} \qquad 2.50$$

The total mass loss $\dot{m}_{tot}''$ is the sum of the mass loss in the gas phase due to oxidation ($\dot{m}_g''$) and the mass loss in the solid phase due to spallation ($\dot{m}_{mech}''$), so we may define B numbers for the separate and total mass loss rates as

$$B_{tot} = \frac{\dot{m}_{tot}''}{h_m}, \qquad B_{ox} = \frac{\dot{m}_g''}{h_m}, \qquad B_{sp} = \frac{\dot{m}_{mech}''}{h_m} \qquad 3.8$$

It follows that $B_{tot} = B_{ox} + B_{sp}$.

Results for ablation in the reentry scenario are shown in Figure 3.2. Results are given for ablation neglecting and including spallation with $\tau^* = 1$. Figure 3.2a clearly shows, for the case without spallation, the transition from kinetically controlled behavior at low freestream temperatures to diffusionally controlled behavior at high freestream temperatures. The same qualitative results appear when including spallation, except that the mass loss due to oxidation is augmented by the mechanical loss.

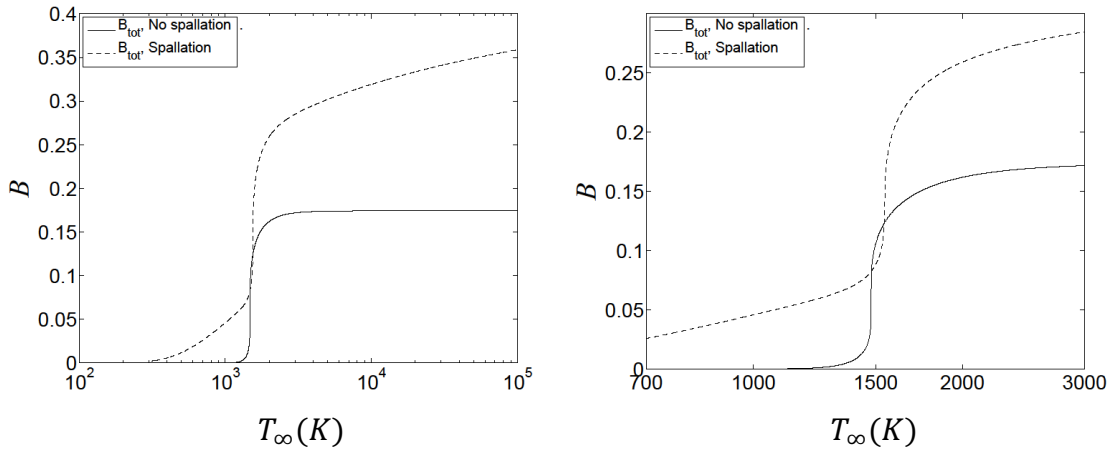

Figure 3.2: (a) B number for ablation with and without mechanical erosion; (b) Detail of oxidation transition regime, showing intersection of curves.

Based on the formulation of $\dot{m}''_{mech}$ and its place in the governing equations, it is reasonable to expect that B_{tot} with spallation will always be greater than or equal to B_{tot} without spallation, and this is true for nearly the entire range of T_∞ tested. However, as shown in Figure 3.2b, there is a small region around T_∞ = 1500 K where B_{tot} with spallation is actually lower than B_{tot} without spallation. The reason for this can be determined from Figure 3.3, which plots T_∞ versus T_w for ablation with and without spallation. The jump in T_w for both curves around T_∞ = 1500 K is due to the rapid increase in B_{ox} in the transition to diffusionally controlled behavior, which provides a large enthalpy source to the system through the enthalpy of combustion.

The curves in Figure 3.3 are very close together, but the one including spallation is shifted slightly to the right of the one without spallation. This is because, as indicated in Equation 3.7b, the spallation term is an energy sink, which means that a slightly lower value of T_w is obtained for a given value of T_∞ when spallation is included versus when it is neglected. This "lag" in T_w as T_∞ increases is insignificant except during the transition to diffusionally controlled behavior, where B_{ox} increases greatly across a small T_w range. In this way, mechanical erosion can actually result in a lower B_{tot} because it delays the transition to diffusively limited behavior in B_{ox} to slightly higher values of T_∞.

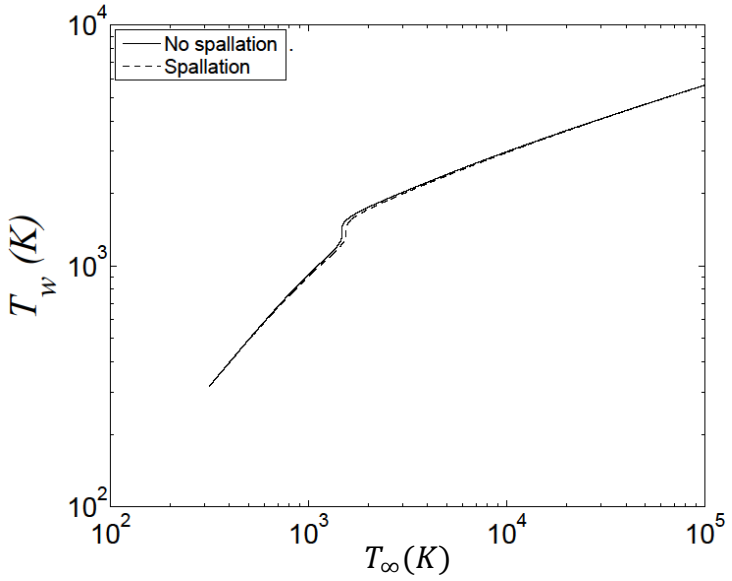

Figure 3.3: T_∞ versus T_w for ablation with and without spallation.

It is also useful to plot results in terms of the wall temperature, which often allows better collapse of information (in terms of $\overline{Da}$ in section 2.2.4, for example). Figure 3.4 plots B_{tot} versus T_w for the system with and without spallation, along with the individual contributions for B_{ox} and B_{sp} for the case including spallation. Because B_{ox} is not dependent upon the rate of spallation, the B_{ox} curve with spallation is identical to the B_{tot} curve without spallation. When stated in terms of T_w, it is obvious that B_{tot} is a summation of the separate contributions of oxidation and spallation, as indicated by Equations 3.8.

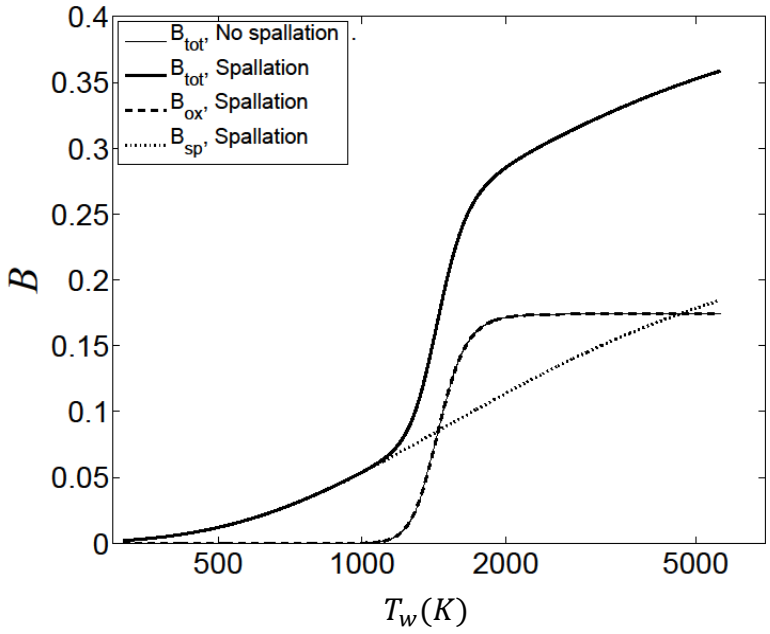

Figure 3.4: B number versus T_w for ablation with and without mechanical erosion. The B_{ox} curve with spallation is identical to the B_{tot} curve without spallation

Finally, results are plotted in Figure 3.5 in terms of $\overline{Da}$, which is the appropriate parameter for nondimensionalization. The curves for B_{ox} collapse, and the transition range within $10^{-2} \lesssim \overline{Da} \lesssim 10^{2}$ is again identified. Although the collapse of B_{ox} curves in terms of $\overline{Da}$ for all reentry scenarios is expected, the collapse of B_{sp} curves is not. $\overline{Da}$ was derived without regard for spallation and thus does not take into account variation in terms such as Sp and γ_{sp}. It is possible that collapse will occur for another nondimensional number that considers spallation, but since this model for spallation is inferior to the one derived in the following subsection, its exploration is presently concluded.

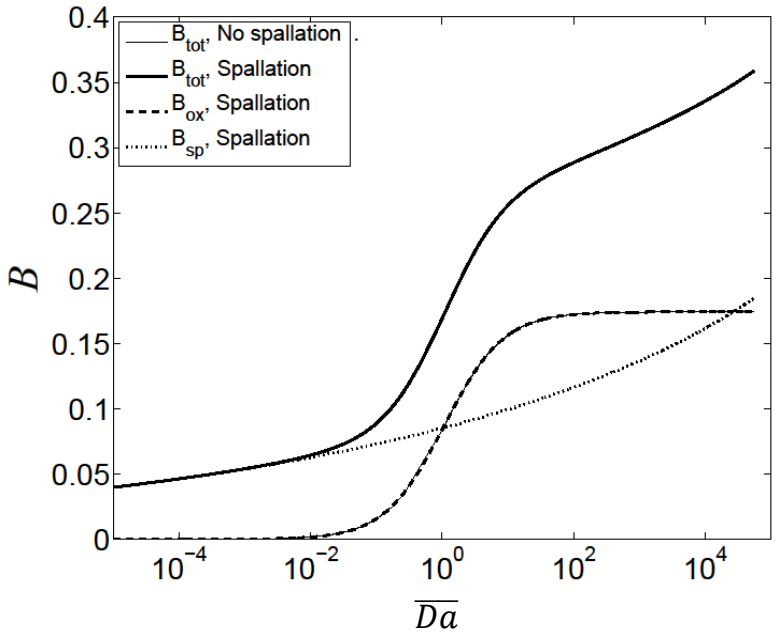

Figure 3.5: B number versus $\overline{Da}$ for ablation with and without mechanical erosion.

The previous study is valuable in that it confirms that the surface temperature decreases in the presence of spallation, and it identifies the possibility of a reduced recession rate in the presence of spallation. These considerations will be kept in mind in the following subsection, where a physics-based model for mechanical erosion is developed.

3.3 A Physics-Based Model for Mechanical Erosion

We now develop a physics-based model for mechanical erosion in a thermochemically ablating system at steady state. Critical to this undertaking is an understanding of the mechanisms by which mechanical erosion occurs and their differences from those of purely thermochemical erosion.

The mechanisms for thermochemical erosion (internal pyrolysis, surface oxidation, surface sublimation) are largely independent of the morphology of the decomposing solid, depending on thermodynamic properties of the surface (temperature, pressure), parameters associated with the external flow (transfer coefficients, gaseous

species concentrations), and kinetic parameters. Thermochemically eroding systems can therefore be homogenized in most cases and spoken of without careful inspection of the morphological changes occurring as degradation proceeds. In mechanically eroding systems, on the other hand, the degradation mechanisms are strongly dependent upon the morphology of the solid, and changes in material properties and geometry have a large effect on the erosion rate of the system. In fact, gross changes in these factors are often necessary for the transition of a non-mechanically eroding system to a mechanically eroding one. In some cases, these changes are brought about by thermochemical erosion itself, as in the formation of a brittle, porous char at the surface of a TPS.

In addition to the morphology of the system, mechanical erosion rates are also dependent upon the state of stress of the system, which is determined by both internal and external loading. This loading results from viscous drag within and across the solid and is consequently highly dependent upon geometry as well. For TPS systems, we can therefore think of the mechanical erosion mechanism as the following: thermochemical erosion leads to significant morphological changes in geometry and material properties, which makes the solid susceptible to high- or low-frequency fracture caused by internal or external loading. Specifically, in reentry scenarios, thermochemical erosion can be caused by internal pyrolysis, surface oxidation of char, and surface sublimation of char. These processes lead to changes in elastic and strength properties, thermal fracture, etching of matrix and fibers, and changes in porosity and permeability. The altered and weakened solid is then subjected to frictional forces along the surface and drag forces associated with outflow of pyrolysis gases, which lead finally to the removal of solid particles.

With the wide variety of reentry scenarios and numerous TPS materials available, the range of possible sequences leading to spallation is vast. Historically, a particular combination of material and environmental conditions has been chosen, and the spallation mechanism developed. We discuss three unique analytical approaches presently for a fiber-reinforced matrix, a particle-reinforced matrix, and a homogeneous matrix, and we then develop a new model for a popular ablative composite, PICA.

3.3.1 Classic Models for Mechanical Erosion

An early successful model for mechanical erosion was proposed by Schneider et al. [21] in 1968, who modeled a charring carbon phenolic material. They proposed that mechanical erosion for this material occurs as discrete ejections of large material layers. First, the bonds between individual sheets of carbon fiber are fractured by internal mechanical stresses, and the free layers are then removed by drag forces. Fracture of layers is assumed to occur due to the superposition of radial and tangential thermal stresses and normal stress caused by the outflow of pyrolysis gases. The cantilevered fiber layers are removed by surface drag and pressure loads from outflowing pyrolysis gases. This model is useful in that it accounts for several physical factors and was validated experimentally, but it is of limited use to the present analysis because it is inherently transient, with material shedding periodically due to the buildup of a thick, fragile fractured layer.

A different model was proposed by Ziering and DiCristina [26] in 1972, who modeled a particle reinforced composite. In this model, a particle and the surrounding matrix are assumed to recede simultaneously due to thermochemical erosion, with the matrix receding faster than the particle. The particle becomes increasingly exposed as the matrix recedes, and eventually is removed by aerodynamic drag. The mass removed at this time is compared to the original mass of the particle to determine the fraction of particle mass removed by mechanical erosion. This model is good in that it addresses the simultaneous erosion of matrix and reinforcement, but its geometry is very idealized and it is difficult to extend the model to more realistic scenarios.

A final model was proposed by Dimitrienko [28] in 1999, who modeled several different classes of materials, including homogeneous, particle reinforced, and fiber reinforced materials. For the homogeneous materials, the material is assumed to undergo volumetric ablation and no surface reactions, and it recedes due to loss of material from the surface that has become porous enough to be removed by aerodynamic drag. Volumetric ablation results in a porous solid consisting of a network of thin beams, and the thickness of the beams at the surface is fixed to be the critical value for fracture by

drag. In this way, a steady recession rate is determined by prescribing the critical beam cross-sectional area at the surface. This is extremely valuable in that it shows a way in which a steady recession rate can be formulated, but the description of the material geometry (and other descriptions for the geometry of reinforced composites) seems too simplistic.

In developing the following model, the two pieces of prior work that were the most helpful were the models of Schneider et al. and Dimitrienko. Both models were very helpful in that they both show how thermochemical erosion produces the weakened state necessary for mechanical removal of particles. The primary difference between the two models is that the model of Schneider et al. must be transient (because mechanical erosion is assumed to occur as the periodic growth and shedding of a weakened char layer) and that of Dimitrienko is steady (the critical state of stress at the surface sets the overall recession rate). Because our entire modeling framework so far is built around the quasi-steady state assumption, the modeling methodology of Schneider et al. is of limited use. The steady formulation of Dimitrienko is more valuable in this case because it demonstrates modeling that fits well within our framework.

However, the modeling of Dimitrienko also has shortcomings. The primary shortcoming is that the success of the modeling relies heavily on an assumption of how the microstructural geometry evolves as thermochemical degradation proceeds. A unit cell is formulated consisting of the material surrounding a single pore. The failure mode of this unit cell is identified, and the cell is assumed to be removed completely when failure occurs. In the real system, the pores will not be uniform and the failure event will not be as repeatable as the model requires. For this model to be more valuable, the irregularity of the pores and random nature of fracture must be addressed.

3.3.2 A Model for Mechanical Erosion of PICA with In-Depth Oxidation of Fibers

With the successes and shortcomings of the aforementioned models in mind, we develop an alternative model for mechanical erosion. Unfortunately, due to the high sensitivity of the mechanical erosion mechanism to geometry, we must sacrifice some generality and specify a material for analysis. Due to its current widespread use in

ablation scenarios, we choose to model phenolic impregnated carbon ablator (PICA), which consists of a randomly oriented carbon fiber preform surrounded by a phenolic matrix, as shown in Figure 3.6. When the material pyrolyzes in depth, the matrix is almost entirely consumed, leaving behind the carbon fiber preform and possibly some residual char. We assume that pyrolysis occurs deep enough within the material that the matrix is completely gone near the surface, and oxidation occurs on the exposed, intact fiber preform.

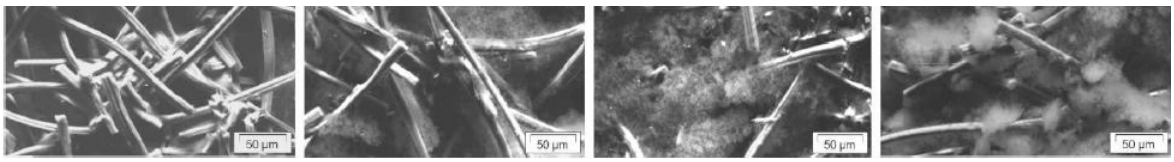

Figure 3.6: SEM micrographs of PICA undergoing in-depth and surface thermochemical ablation. Left to right: surface, char, pyrolysis zone, virgin material. Taken from [30].

Traditional ablation models, such as the one described in section 2.1, would assume that the oxidation of the carbon preform fibers, which leads to recession of the surface, occurs at the surface in a region of infinitesimal thickness. An important observation was made by Lachaud et al. [31] and Lachaud et al. [32], who observe that for a porous material such as PICA charred preform, the gaseous oxidizer may penetrate to some depth within the surface, and the idea of a global surface oxidation rate is inadequate to describe the oxidation process. In such a system, oxidation may take place over a region whose thickness is large compared to the effective fiber length (which may be thought of as the average distance between two contact points on a fiber), as shown in Figure 3.7a. The entire effective length of the fiber is then subject to oxidation, and the diameter decreases along the entire length. The rate of oxidation will in general be a function of depth, but for sufficiently large oxidation depths or sufficiently small effective fiber lengths, the mass loss rate across any effective length is roughly constant, and the diameter recedes uniformly. We then may expect to see oxidation as in Figure 3.7b, where an exposed fiber is reduced to roughly the same diameter along its entire effective length. This thinning reduces the bending stress the fiber can support without

fracturing, and we may imagine that fibers are removed by the external flow after sufficient thinning. This is the basis of the new proposed mechanical erosion model: oxidation of carbon fibers occurs to a finite depth within the surface of the solid, and the thinning of fibers within this depth allows them to be removed by a sufficiently strong external flow.

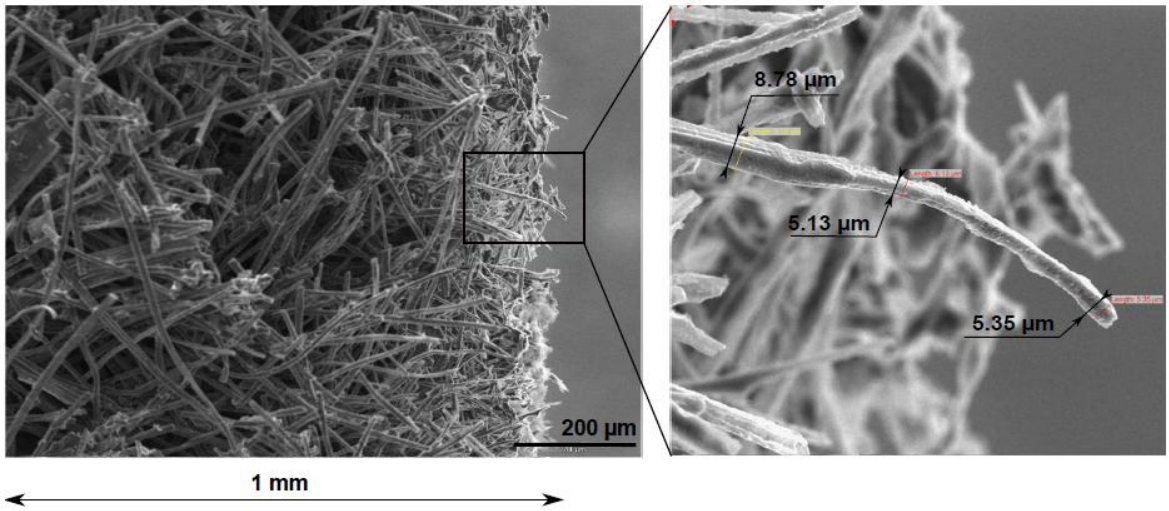

(a) (b)

Figure 3.7: SEM micrographs of carbon preform (a), with evidence of fiber thinning (b). Taken from [32].

We may model this erosion mechanism quantitatively by developing conservation laws for the average fiber diameter, bulk solid volume fraction, and the oxidizer. These conservation laws were previously derived by Lachaud et al. in [31], and the work therein has been the starting point for the current exploration. Following the derivation, the conservation laws are nondimensionalized and solved numerically. A useful approximate solution is obtained for the degradation behavior of the porous PICA-type solid with or without mechanical erosion, and this relation is incorporated into reentry modeling in section 3.3.3.

3.3.2.1 Conservation Laws

First, we derive the conservation law for the average fiber diameter. While this equation is derived for a single fiber oriented perpendicular to the surface, the result is the same for a fiber not perpendicular to the surface. More importantly, since the fiber effective length is expected to be much smaller than the oxidation penetration depth, it also indicates the evolution of the average fiber diameter at any point within the solid.

Figure 3.8 shows an infinitesimal control volume for a fiber element, where x is the coordinate direction perpendicular to the surface (positive into the solid, with $x = 0$ at the surface), ρ_s is the density of the carbon fiber, v_s is the recession velocity of the surface, and d is the fiber diameter (or average fiber diameter). The surface mass loss rate $\dot{m}''_{C,*}$ is the mass loss rate of carbon per unit surface area of the fiber, which differs from the mass loss rate per unit area of the TPS surface as defined in section 2.1.1. This loss rate is formulated as

$$\dot{m}''_{C,*} = r\dot{m}''_{O_2,*} = r\rho_g Y_{O_2} A_{O_2,*} exp\left(-\frac{E_{a,O_2,*}}{RT_w}\right) \qquad 3.9$$

where ρ_g and Y_{O_2} are the local gas density and oxygen concentration within the porous solid, and $A_{O_2,*}$ and $E_{a,O_2,*}$ are Arrhenius parameters for mass loss from the fiber surface. The stoichiometric fuel-air ratio r is $r = \nu_C W_C / \nu_{O_2} W_{O_2}$, and $\dot{m}''_{O_2,*}$ is the mass consumption rate of oxygen per unit surface area of fiber. In this derivation we assume that only the oxidation reaction of Equation 2.20 takes place. Also, it is assumed that the thermal penetration depth is much larger than the oxidation penetration depth, so the temperature throughout the entire oxidation region is approximately the wall temperature T_w. Figure 3.8 indicates that at steady state a balance must exist between convection of the fiber and oxidation of the fiber. From this, we obtain the following differential equation for the variation of average fiber diameter (in case of confusion, the term on the left is the quantity $\frac{1}{2}\rho_s v_s$ multiplied by the first derivative of the diameter, d, with respect to x):

$$\frac{1}{2}\rho_s v_s \frac{d}{dx}(d) = \dot{m}''_{C,*} \qquad 3.10$$

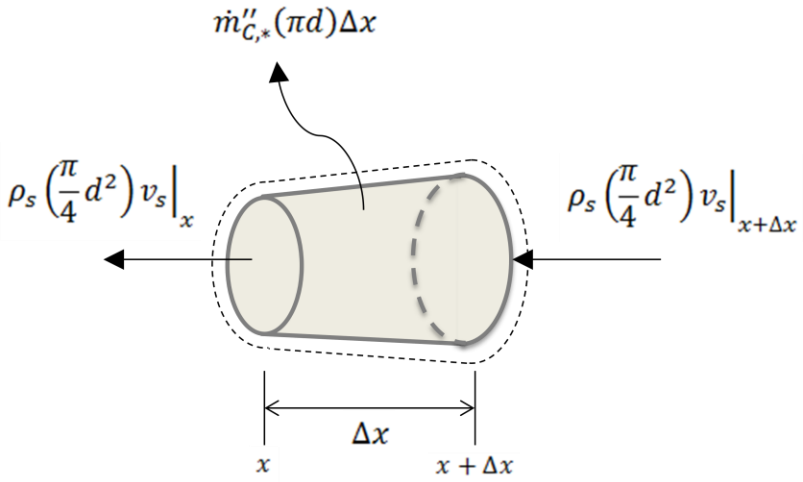

Figure 3.8: Control volume for an infinitesimal fiber element.

The infinitesimal control volume for global conservation of mass within the homogenized porous solid is shown in Figure 3.9, where φ is the solid volume fraction (volume inhabited by solid carbon per total volume), A is an arbitrary unit of area, and $\dot{m}'''_C$ is the volumetric consumption rate of solid carbon. This is related to $\dot{m}''_{C,*}$ by

$$\dot{m}'''_C \Delta V = \dot{m}''_{C,*} \Delta A_{s,f} \tag{3.11}$$

where ΔV is an arbitrary unit of volume and $\Delta A_{s,f}$ is the surface area of carbon fibers within that volume. The two mass loss rates are then related by

$$\frac{\dot{m}'''_C}{\dot{m}''_{C,*}} = \frac{\Delta A_{s,f}}{\Delta V} = \frac{\Delta A_{s,f}}{\Delta V_f}\frac{\Delta V_f}{\Delta V} = \frac{\pi d l}{\pi \frac{d^2}{4} l}\varphi = 4\frac{\varphi}{d} \tag{3.12}$$

where ΔV_f is the volume of carbon fibers within the volume ΔV. The differential equation for the solid volume fraction, obtained from Figure 3.9, is then

$$\frac{d}{4\varphi}\rho_s v_s \frac{d\varphi}{dx} = \dot{m}''_{C,*} \tag{3.13}$$

where, in case of confusion, the term on the left is the quantity $\frac{d}{4\varphi}\rho_s v_s$, which contains the variables d and φ, multiplied by the first derivative of φ with respect to x.

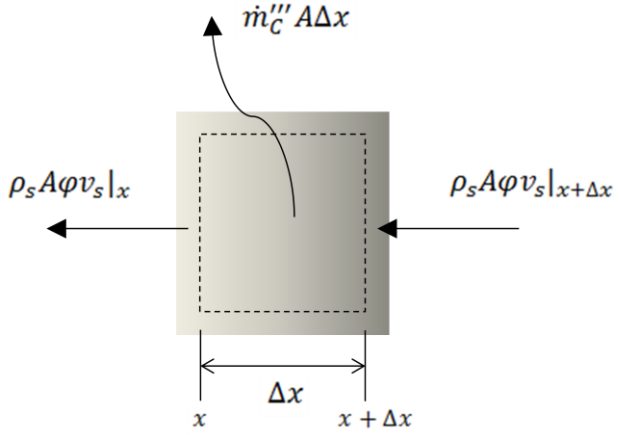

Figure 3.9: Control volume for an infinitesimal unit in the homogeneous porous solid.

Equations 3.10 and 3.13 can be combined to obtain a relationship between d and φ. Eliminating $\dot{m}_{C,*}''$, integrating, and using the fact that d and φ take their unoxidized values d_o and φ_o as $x \to \infty$, we obtain

$$\frac{\varphi}{\varphi_o} = \left(\frac{d}{d_o}\right)^2 \tag{3.14}$$

Finally, the conservation of oxygen within the porous solid is examined. Figure 3.10 shows the relevant processes for an infinitesimal control volume, where u is the average velocity of outflowing gas within the solid and D_{eff} is the effective diffusivity of the porous medium, defined as

$$D_{eff} = D(1-\varphi)\frac{\delta}{\tau} \tag{3.15}$$

where D is the gas phase diffusivity, δ is the constrictivity, and τ is the tortuosity. In general, D_{eff} will be a function of x because of the variability of φ (Equation 3.13), but we will assume for simplicity that D_{eff} is constant throughout the porous solid. The outflowing gas contains both the pyrolysis gas and the net mass flux released by oxidation. Because oxidation now occurs throughout a finite thickness of material, u will thus also be a function of x. For simplicity, it is assumed that u is constant, or that only the pyrolysis gas flux is appreciable. Figure 3.10 shows that at steady state a balance

exists between diffusion of oxygen into the solid and the combined effect of consumption and blowing out of the solid.

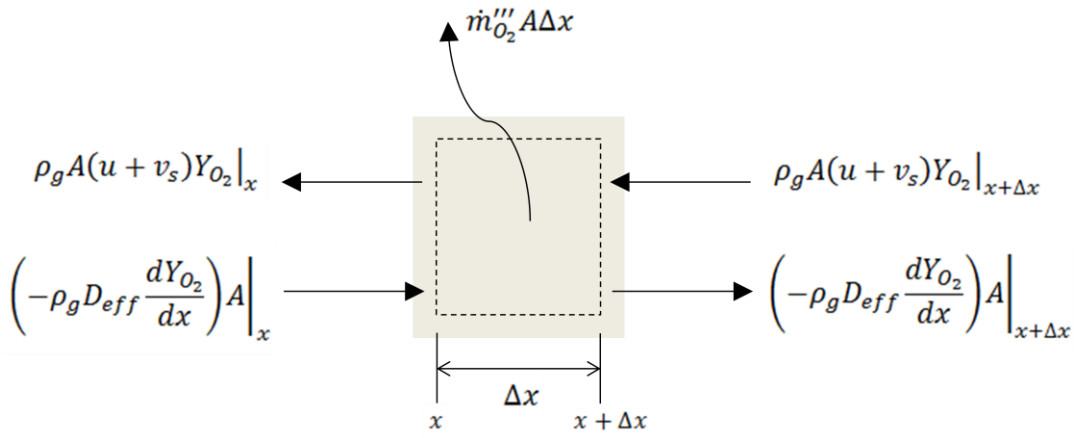

Figure 3.10: Control volume for conservation of oxygen within porous solid.

Figure 3.10 yields the following equation for the conservation of oxygen within the porous solid:

$$\frac{d^2Y_{O_2}}{dx^2} + \frac{(u+v_s)}{D_{eff}}\frac{dY_{O_2}}{dx} - \frac{4\varphi_o k_f}{D_{eff}{d_o}^2}Y_{O_2}d = 0 \qquad 3.16$$

This is a convection diffusion equation with a sink term. In Equation 3.16, since the temperature within the oxidation zone is assumed to be constant, the Arrhenius terms are grouped into an overall reactivity $k_f = A_{O_2,*}exp\left(-E_{a,O_2,*}/RT_w\right)$ for convenience.

3.3.2.2 Nondimensionalization

Useful information can be extracted from the governing equations through nondimensionalization. First, we perform a scaling analysis on Equation 3.16 to determine the correct scale for the oxidation penetration depth. Looking at this equation, we see that the fundamental balance must be between diffusion and consumption, as the convection term may not be present if u is zero and v_s is very small. Thus, if the scale of Y_{O_2} is $Y_{O_2,w}$ (the surface concentration) and the scale of x is δ_{ox} (the oxidation penetration

depth), then we neglect the convection term and obtain the following scaling result for δ_{ox}:

$$\frac{\delta_{ox}}{d_o} \sim \left(\frac{k_f}{D_{eff}/\varphi_o d_o}\right)^{-1/2} \tag{3.17a}$$

The term in parentheses is another type of Damkohler number, relating reaction rate to diffusion within the porous medium. We thus define a Damkohler number for oxidation, Da_{ox}, as

$$Da_{ox} = \frac{4k_f}{D_{eff}/\varphi_o d_o} \tag{3.17b}$$

and define the penetration depth as

$$\frac{\delta_{ox}}{d_o} = {Da_{ox}}^{-1/2} \tag{3.17c}$$

The factor of 4 in Equation 3.17b is included for future convenience.

Performing scaling on Equation 3.10 gives

$$v_s \sim r\frac{\rho_g}{\rho_s} Y_{O_2,w} \left(\frac{k_f D_{eff}}{\varphi_o d_o}\right)^{1/2} \tag{3.18a}$$

which identifies a characteristic velocity for the recession rate (v_{ch}) as

$$v_{ch} = r\frac{\rho_g}{\rho_s} Y_{O_2,w} \left(\frac{k_f D_{eff}}{\varphi_o d_o}\right)^{1/2} \tag{3.18b}$$

It is now possible to nondimensionalize the governing equations. This is done using the following nondimensional quantities:

$$x^* = \frac{x}{\delta_{ox}}, \qquad d^* = \frac{d}{d_o}, \qquad {Y_{O_2}}^* = \frac{Y_{O_2}}{Y_{O_2,w}}, \qquad {v_s}^* = \frac{v_s}{v_{ch}}, \qquad u^* = \frac{u}{v_{ch}} \tag{3.19}$$

The result for Equation 3.16 is

$$\frac{d^2 {Y_{O_2}}^*}{d{x^*}^2} + g^*(u^* + {v_s}^*)\frac{d{Y_{O_2}}^*}{dx^*} - d^* {Y_{O_2}}^* = 0 \tag{3.20a}$$

where

$$g^* = \frac{1}{2}\frac{\rho_g}{\rho_s}\frac{\hat{r} Y_{O_2,w}}{\varphi_o} \tag{3.20b}$$

We expect that $v_s^* \approx 1$, and using data for the Stardust reentry scenario from [31], we obtain $g^* \approx 10^{-4}$ and $u^* \approx 10^4$. Thus, in practical scenarios, it is reasonable to neglect convection caused by the bulk motion of the solid, but it may not be possible to neglect blowing in all cases. Neglecting v_s^* in Equation 3.20a and combining g^* and u^* into a single nondimensional term gives the final form for the oxygen conservation equation:

$$\frac{d^2 Y_{O_2}^*}{dx^{*2}} + U\frac{dY_{O_2}^*}{dx^*} - d^* Y_{O_2}^* = 0 \qquad 3.21$$

where

$$U = \frac{1}{2}u\left(\frac{d_o}{\varphi_o k_f D_{eff}}\right)^{1/2} \qquad 3.22$$

Using the nondimensional quantities (Equation 3.19) in Equation 3.10 gives, for the average diameter,

$$\frac{dd^*}{dx^*} = \frac{1}{v_s^*} Y_{O_2}^* \qquad 3.23$$

3.3.2.3 Thermochemical Degradation of a Porous Solid

We will now solve Equations 3.21 and 3.23, which describe the thermal degradation of a porous solid. In this subsection, mechanical erosion will be neglected in order to better explain the thermochemical behavior. For the moment, we will also neglect blowing within the solid by setting $U = 0$, but we will reincorporate it later.

Boundary conditions for Equation 3.21 are as follows:

$$\lim_{x^* \to \infty} Y_{O_2}^* = 0 \qquad 3.24a$$

$$Y_{O_2}^*\big|_{x^*=o} = 1 \qquad 3.24b$$

This says that oxygen is completely consumed deep within the solid, and the surface concentration $Y_{O_2,w}$ is assumed at the surface. In reality, the surface concentration must be determined by incorporating the porous solid model into the mass and energy balances for the ablating system. However, the solutions to the two regions may be solved separately by nondimensionalizing the oxygen concentration within the solid using the surface concentration (as has been done). This decouples the porous solid model from

the gas side transport modeling and allows its solution to be determined without knowledge of the gas phase.

Equation 3.23, which is a first order ODE, actually has two boundary conditions:

$$\lim_{x^* \to \infty} d^* = 1 \qquad 3.25a$$

$$d^*|_{x^*=0} = 0 \qquad 3.25b$$

Equation 3.25a says that past the oxygen penetration zone d assumes its non-degraded value d_o. Equation 3.25b says that, for the surface to recede at steady state, the fibers must be completely consumed by oxidation when they reach the surface at $x = 0$. The extra boundary condition (Equation 3.25b) now requires that ${v_s}^*$, the nondimensional recession rate, cannot be specified independently and is determined by the solution of Equations 3.21 and 3.23 with boundary conditions 3.24 and 3.25. That is, for a steady state solution, there is a unique value of the recession rate for a given set of differential equations and boundary conditions. This agrees with intuition.

Equations 3.21 and 3.23 were solved numerically with boundary conditions 3.24 and 3.25 and $U = 0$. The resulting profiles for ${Y_{O_2}}^*$ and d^* are shown in Figure 3.11, and the resulting value for ${v_s}^*$ is

$$For\ d^*|_{x^*=0} = 0, U = 0: \qquad {v_s}^* = 1.22 \qquad 3.26a$$

This is a very important result because it gives the overall recession rate v_s, the quantity of most interest in ablation problems, once the characteristic velocity v_{ch} is calculated. Because v_s is normalized by the characteristic velocity to obtain ${v_s}^*$, it makes sense that ${v_s}^*$ should be of order 1.

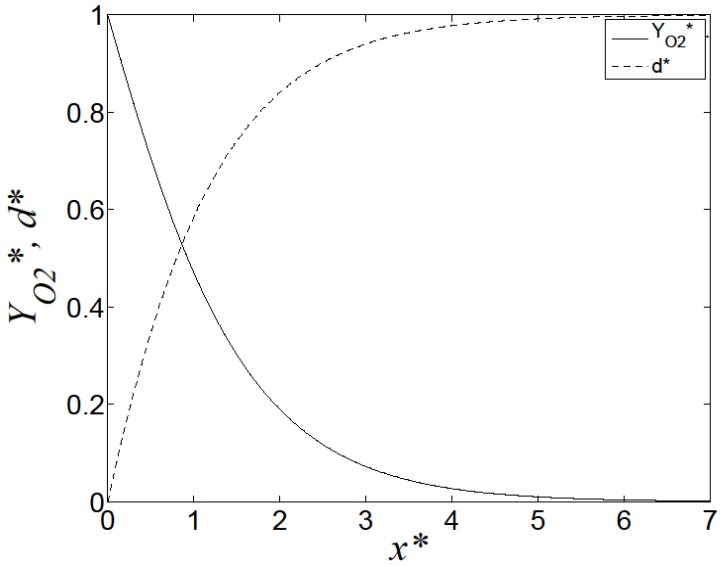

Figure 3.11: Numerical solution for $Y_{O_2}{}^*$ and d^* with $U = 0$.

Figure 3.11 shows that the scale for δ_{ox} is correct; the reaction zone penetrates to roughly $x^* = 5$, or $x = 5\delta_{ox}$. The shape of the profiles is also what would be expected for a diffusion/sink problem.

For U greater than 0, results are as shown in Figure 3.12. As blowing increases, the reaction zone is driven out of the solid as the diffusion of gas is increasingly opposed by advection. The value of $v_s{}^*$ is affected greatly by the presence of blowing, as shown in Figure 3.13, which plots values of $v_s{}^*$ versus U obtained from the numerical ODE solution along with a useful approximate solution, which will be detailed shortly. For $U \lesssim 10^{-1}$, the value of $v_s{}^*$ is essentially constant, but for $U \gtrsim 1$, $v_s{}^*$ is attenuated severely. Thus, for porous systems in oxidizing environments, the recession rate $(v_s{}^*)$ can be reduced by outflowing gas. In the reentry scenario, blowing of pyrolysis gases is normally deemed beneficial because it decreases transport coefficients by thickening the boundary layer. This analysis shows an added benefit, namely the ability of pyrolysis gases to resist the penetration of the oxidizer into the porous char. Written succinctly, this result is

$$For\ d^*|_{x^*=0} = 0, U > 0: \qquad v_s{}^* < 1.22 \qquad 3.26b$$

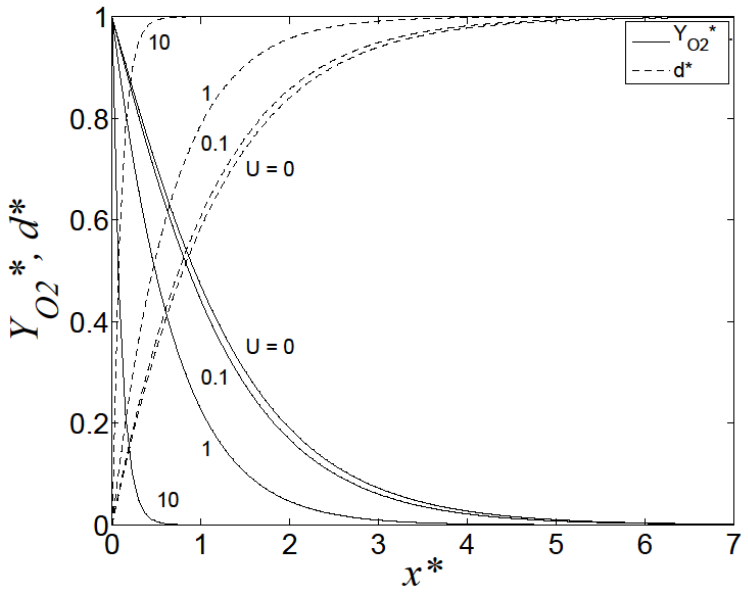

Figure 3.12: Numerical solutions for $Y_{O_2}{}^*$ and d^* with variable U.

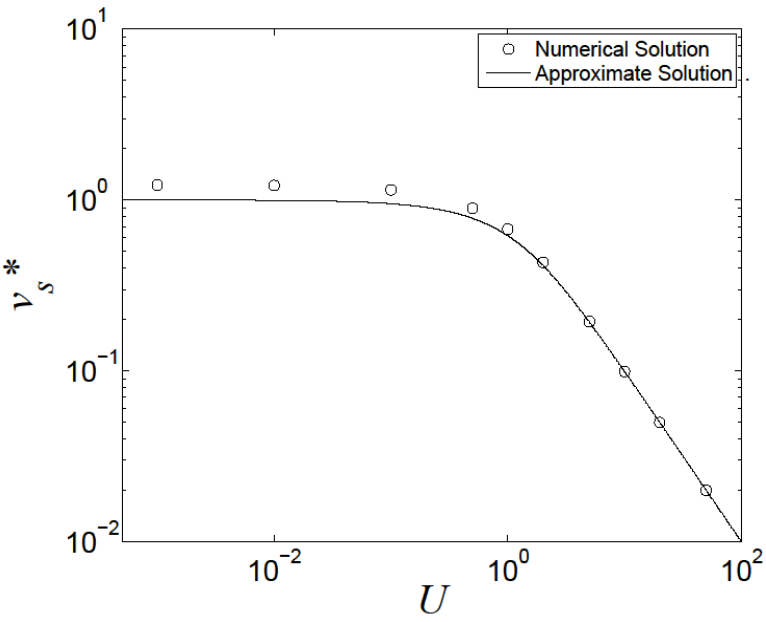

Figure 3.13: $v_s{}^*$ versus U, showing attenuation of $v_s{}^*$ at high U.

Although the system of ordinary differential equations governing oxidation within the porous solid is nonlinear (because of the third term in Equation 3.21) and has no

analytical solution, a useful approximate solution can be obtained by linearizing Equation 3.21. Setting $d^* = 1$ in this equation gives a second order linear ODE for ${Y_{O_2}}^*$,

$$\frac{d^2{Y_{O_2}}^*}{dx^{*2}} + U\frac{d{Y_{O_2}}^*}{dx^*} - {Y_{O_2}}^* = 0 \qquad 3.27$$

The solution to this equation, after applying boundary conditions 3.24, is

$${Y_{O_2}}^* = exp\left[-\left(\frac{U+\sqrt{U^2+4}}{2}\right)x^*\right] \qquad 3.28$$

Incorporating this into Equation 3.23 yields the ODE

$$\frac{dd^*}{dx^*} = \frac{1}{{v_s}^*}exp\left[-\left(\frac{U+\sqrt{U^2+4}}{2}\right)x^*\right] \qquad 3.29$$

whose solution, with boundary condition 3.25a, is

$$d^* = 1 - \frac{1}{{v_s}^*}\left(\frac{2}{U+\sqrt{U^2+4}}\right)exp\left[-\left(\frac{U+\sqrt{U^2+4}}{2}\right)x^*\right] \qquad 3.30a$$

The application of boundary condition 3.25b determines the form of ${v_s}^*$:

$${v_s}^* = \frac{2}{U+\sqrt{U^2+4}} \qquad 3.31$$

This gives the solution for d^* as

$$d^* = 1 - exp\left[-\left(\frac{U+\sqrt{U^2+4}}{2}\right)x^*\right] \qquad 3.30b$$

The approximate solutions of Equations 3.28 and 3.30b are plotted along with their respective numerical solutions in Figure 3.14. The approximate solutions follow the actual solutions very well, and accuracy actually improves as U increases. Equation 3.31 is an important result, and it is included in Figure 3.13 along with the numerical results. This explicit equation gives an excellent approximation to ${v_s}^*$ for design purposes without requiring the solution of the nonlinear system of ODEs. When $U = 0$, Equation 3.31 gives ${v_s}^* = 1$, which is very close to the result of 1.22 given by Equation 3.26a.

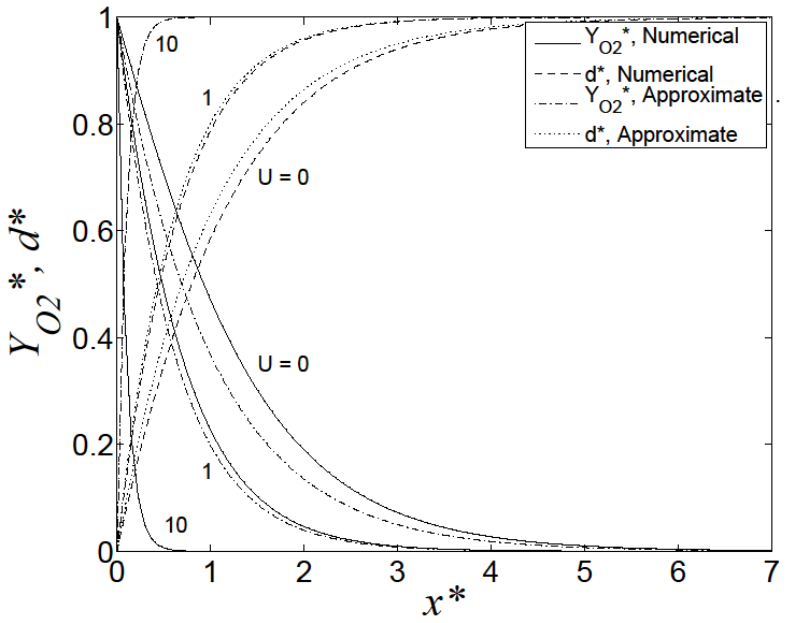

Figure 3.14: Numerical and approximate solutions for $Y_{O_2}{}^*$ and d^*.

3.3.2.4 Thermochemical Degradation of a Porous Solid with Mechanical Erosion

We now turn to the incorporation of mechanical erosion into an oxidizing porous solid. In the previously derived model, the diameters of the carbon fibers are reduced by oxidation, and at the surface they are reduced all the way to zero, which is the definition of the surface in this solid. However, reason dictates that in the presence of aerodynamic loading, fibers of effective length Δ at the surface will not survive all the way to $d = 0$ but will break off at some critical diameter, d_{cr}, at which the stress at the base of each fiber is equal to the critical stress for fracture. We can then imagine that at steady state we would expect to find fibers near the surface of diameter approaching d_{cr} but no fibers of diameter less than d_{cr}. This leads to a way to incorporate mechanical erosion into the existing model, namely fixing the value for average diameter at the surface to be equal to the critical diameter d_{cr}. Defining $d_c{}^* = d_{cr}/d_o$, the boundary condition 3.25b becomes

$$d^*|_{x^*=0} = d_c{}^* \qquad 3.25c$$

This is the only adjustment that must be made to the governing equations and boundary conditions to incorporate spallation, and in fact allowing d_{cr} to go to zero recovers the

original boundary condition. From the point of view of global mass conservation for individual fibers, this model makes sense, because it says that a fiber approaches the oxidation zone at its original diameter d_o, undergoes mass loss by oxidation within the oxidation zone, and exits the surface in the solid phase in pieces with diameter d_{cr}. This technique of specifying a critical surface dimension was inspired by the steady-state model of Dimitrienko [28] mentioned earlier.

Initially, we simplify the problem by assuming that $U = 0$. Numerical solutions to Equations 3.21 and 3.23 with boundary conditions 3.24, 3.25a, and 3.25c are shown in Figure 3.15. The profiles for ${Y_{O_2}}^*$ are only slightly affected by the changing boundary condition, and the shape of the d^* profiles remains the same even though the y-intercept changes. As with the variability in U, variability in ${d_c}^*$ has a large effect on ${v_s}^*$, as shown in Figure 3.16. The nondimensional recession rate ${v_s}^*$ is seen to increase monotonically with ${d_c}^*$ in the range studied, which makes intuitive sense. ${v_s}^*$ asymptotically approaches infinity as ${d_c}^*$ approaches one, which says that for weak fibers which oxidize very little before fracturing, an enormous amount of mass is lost at steady state. Therefore, in general,

$$For\ {d_c}^* > 0, U = 0: \qquad {v_s}^* > 1.22 \tag{3.26c}$$

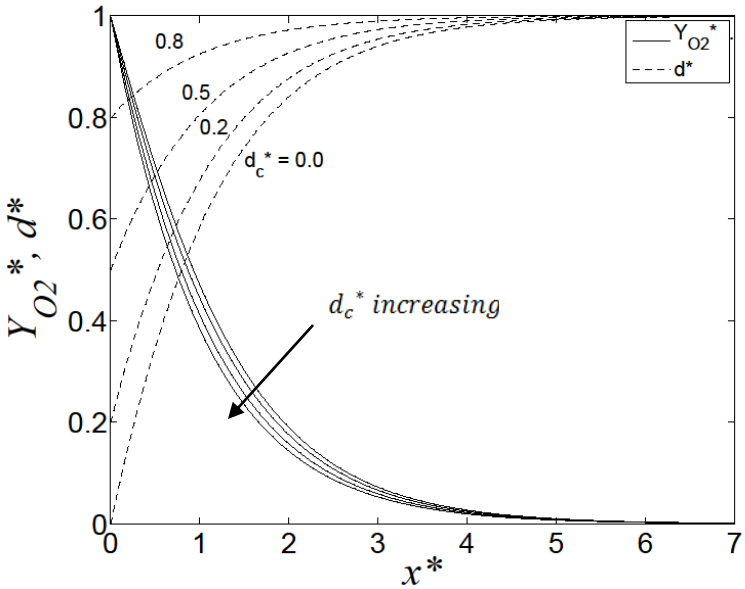

Figure 3.15: Numerical solutions for ${Y_{O_2}}^*$ and d^* with $U = 0$ and variable ${d_c}^*$.

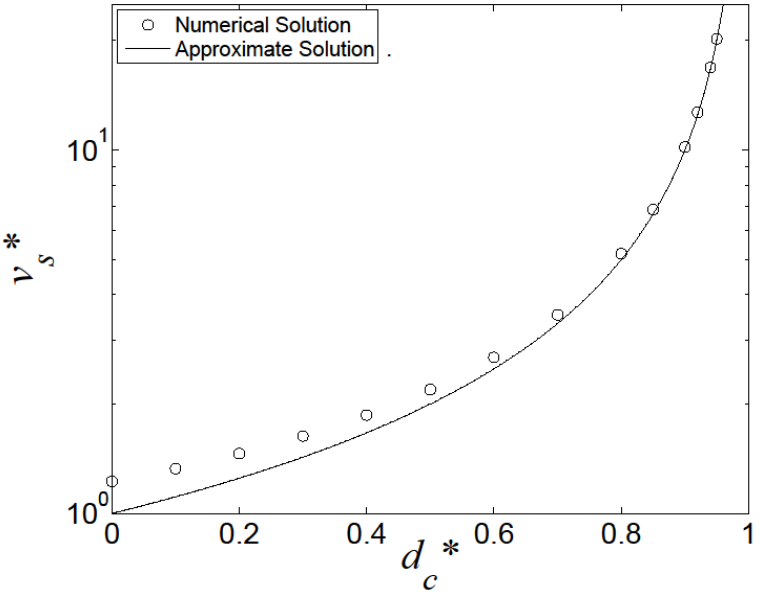

Figure 3.16: $v_s{}^*$ versus $d_c{}^*$ for degradation with $U = 0$.

As with the blowing scenario, a useful analytical approximation can be obtained by linearizing the governing equations. Applying boundary condition 3.25c to Equation 3.30a with $U = 0$ gives

$$v_s{}^* = \frac{1}{1 - d_c{}^*} \qquad 3.32$$

The solution for d^* is then

$$d^* = 1 - (1 - d_c{}^*)exp(-x^*) \qquad 3.30c$$

Equations 3.30c and 3.28 with $U = 0$ are shown in Figure 3.17 along with the numerical solutions. As with the blowing scenario, agreement is quite good, and accuracy improves as $d_c{}^*$ increases. Equation 3.32 is another useful result, and it is plotted in Figure 3.16. Like Equation 3.31, it allows good estimation of the recession rate without solving the governing equations numerically.

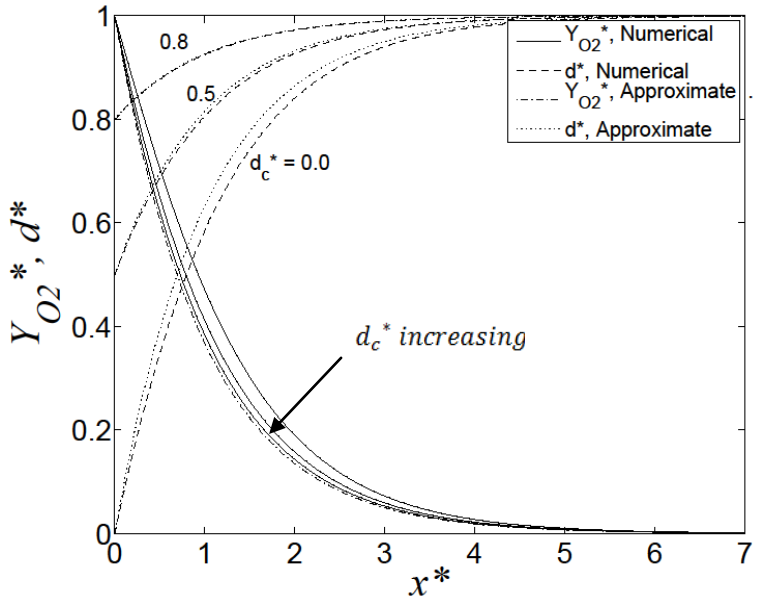

Figure 3.17: Numerical and approximate solutions for $Y_{O_2}{}^*$ and d^*, with $U = 0$ and $d_c{}^*$ varying.

The final step is to combine the effects of blowing and mechanical erosion. Again, an analytical approximation is available, and applying boundary condition 3.25c to Equation 3.30a gives

$$v_s{}^* = \left(\frac{1}{1 - d_c{}^*}\right)\left(\frac{2}{U + \sqrt{U^2 + 4}}\right) \qquad 3.33$$

which incorporates both the mechanical erosion and blowing results. The final form for d^* is

$$d^* = 1 - (1 - d_c{}^*)exp\left[-\left(\frac{U + \sqrt{U^2 + 4}}{2}\right)x^*\right] \qquad 3.30d$$

Equation 3.33 is plotted in Figure 3.18 along with values obtained numerically. Agreement is extremely good for high values of $d_c{}^*$ and U and still reasonably good everywhere else. Equation 3.33 is an extremely valuable result because it allows the determination of the recession rate v_s in terms of only three parameters: v_{ch}, $d_c{}^*$, and U. Also, as will be shown in the following subsection, it presents information in a form that is extremely convenient for incorporation into the existing ablation code.

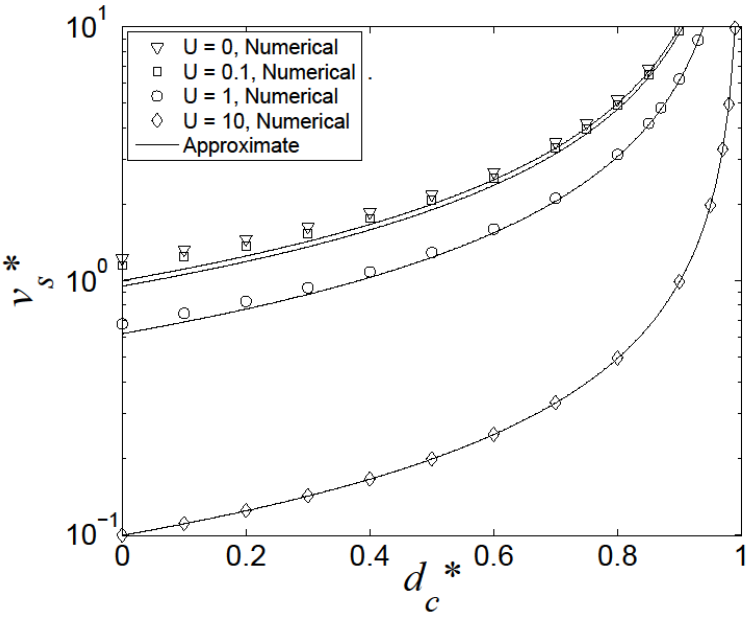

Figure 3.18: Numerical and approximate results for dependence of $v_s{}^*$ on $d_c{}^*$ and U.

3.3.3 Incorporation of Porous Solid Degradation Model into Existing Ablation Model

The result of modeling in the preceding section (Equation 3.33) will now be incorporated into the existing ablation model. To do this, we will make an adjustment to the definition of the mass consumption rates to account for oxidation and spallation of the porous medium. Then, the governing equations of the ablation model will be modified and examined, and a physically based model for determining $d_c{}^*$ will be developed. Finally, the complete thermo-chemo-mechanical erosion model will be exercised and examined.

3.3.3.1 Adjustment of the Mass Loss Formulation Based on the $v_s{}^*$ Model

The total mass consumption rate of carbon for the graphite oxidation reaction considered in section 2.1.2 (without spallation) was

$$\dot{m}''_{tot} = r\rho_g Y_{O_2,w} A_{O_2} exp\left(-\frac{E_{a,O_2}}{RT_w}\right) \qquad 3.34$$

The preceding analysis allows a new definition of this mass flux based on $v_s{}^*$:

$$\dot{m}''_{tot} = \rho_s \varphi_o v_s = \rho_s \varphi_o v_{ch} {v_s}^* \quad (3.35)$$

Using the definition of v_{ch} produces

$$\dot{m}''_{tot} = r\rho_g Y_{O_2,w} \left(\left[\frac{D_{eff}\varphi_o}{d_o} \right] \times \left[A_{O_2,*} exp\left(-\frac{E_{a,O_2,*}}{RT_w} \right) \right] \right)^{1/2} {v_s}^* \quad (3.36)$$

This result says that the overall reactivity of a porous TPS material, from the macroscopic point of view of the receding surface, is the geometric mean of the intrinsic fiber reactivity k_f and a second reactivity equal to $D_{eff}\varphi_o/d_o$, which represents transport within the porous medium. The overall reactivity can thus be limited by either slow reaction kinetics or slow transport within the porous medium.

In the pursuit of a mass loss rate which is as similar to that in section 2.1.2 as is possible, we manipulate Equation 3.36 to obtain

$$\dot{m}''_{tot} = r\rho_g Y_{O_2,w} \left(\frac{D_{eff}\varphi_o}{d_o} A_{O_2,*} \right)^{1/2} exp\left(-\frac{\left(E_{a,O_2,*}/2\right)}{RT_w} \right) {v_s}^* \quad (3.37)$$

Redefining the macro-scale preexponential $\left(A_{O_2}\right)$ and activation energy $\left(E_{a,O_2}\right)$ as

$$A_{O_2} = \left(\frac{D_{eff}\varphi_o}{d_o} A_{O_2,*} \right)^{1/2} \quad (3.38a)$$

$$E_{a,O_2} = \frac{E_{a,O_2,*}}{2} \quad (3.38b)$$

we obtain the following form for the total carbon mass loss rate:

$$\dot{m}''_{tot} = r\rho_g Y_{O_2,w} A_{O_2} exp\left(-\frac{E_{a,O_2}}{RT_w} \right) {v_s}^* \quad (3.39)$$

This is identical to the previous expression except for the addition of ${v_s}^*$, which may now be viewed as a correction factor to the mass loss rate to account for blowing within the porous medium and for spallation.

In the energy balance for the ablation model which accounts for mechanical erosion (Equation 3.6), it is necessary to know the amount of the total mass lost which is lost in the gas phase through oxidation $\left(\dot{m}''_g\right)$ and through spallation $(\dot{m}''_{mech})$. To do this we define variables ${v_{ox}}^*$ and ${v_{mech}}^*$ such that

$$\dot{m}_g'' = \dot{m}_{tot}'' \frac{{v_{ox}}^*}{{v_s}^*} = r\rho_g Y_{O_2,w} A_{O_2} exp\left(-\frac{E_{O_2}}{RT_w}\right) {v_{ox}}^* \quad 3.40a$$

$$\dot{m}_{mech}'' = \dot{m}_{tot}'' \frac{{v_{mech}}^*}{{v_s}^*} = r\rho_g Y_{O_2,w} A_{O_2} exp\left(-\frac{E_{O_2}}{RT_w}\right) {v_{mech}}^* \quad 3.40b$$

A relationship between ${v_s}^*$, ${v_{ox}}^*$, and ${v_{mech}}^*$ must be found. First, we know that $\dot{m}_g''$ is the integral of the volumetric consumption rate of carbon ($\dot{m}_C'''$) within the porous solid:

$$\dot{m}_g'' = \int_{x=0}^{\infty} \dot{m}_C''' dx = \int_{x=0}^{\infty} \frac{4\varphi_o d}{{d_o}^2} \dot{m}_{C,*}'' dx \quad 3.41$$

Substituting for $\dot{m}_g''$ and $\dot{m}_{C,*}''$ from Equations 3.40a and 3.9 respectively gives

$$r\rho_g Y_{O_2,w} A_{O_2} exp\left(-\frac{E_{O_2}}{RT_w}\right) {v_{ox}}^* = \int_{x=0}^{\infty} \frac{4\varphi_o d}{{d_o}^2} r\rho_g Y_{O_2} A_{O_2,*} exp\left(-\frac{E_{O_2,*}}{RT_w}\right) dx \quad 3.42$$

Nondimensionalizing this equation gives the result

$${v_{ox}}^* = 2\int_{x^*=0}^{\infty} d^* {Y_{O_2}}^* dx^* \quad 3.43$$

Next, global conservation of mass for a single fiber says that the mass lost by oxidation is equal to the difference between the original mass and the spalled mass:

$$\rho_s \left(\frac{\pi}{4} {d_o}^2\right) v_s - \rho_s \left(\frac{\pi}{4} {d_{cr}}^2\right) v_s = \int_{x=0}^{\infty} \dot{m}_{C,*}'' (\pi d) dx \quad 3.44$$

Nondimensionlizing this equation gives

$${v_s}^* [1 - ({d_c}^*)^2] = 2\int_{x^*=0}^{\infty} d^* {Y_{O_2}}^* dx^* \quad 3.45$$

Eliminating the integral term between Equations 3.43 and 3.45 yields

$${v_{ox}}^* = {v_s}^* [1 - ({d_c}^*)^2] \quad 3.46$$

Another relationship is available from global conservation of mass, which states:

$$\dot{m}_{tot}'' = \dot{m}_g'' + \dot{m}_{mech}'' \quad 3.47$$

Substituting using Equations 3.39 and 3.40 gives

$${v_s}^* = {v_{ox}}^* + {v_{mech}}^* \quad 3.48$$

Eliminating ${v_{ox}}^*$ using Equation 3.46 yields

$${v_{mech}}^* = {v_s}^* ({d_c}^*)^2 \quad 3.49$$

Equations 3.46 and 3.49 allow all mass loss rates to be computed independently. These will now be incorporated into the existing ablation model.

3.3.3.2 Adjustment of Governing Equations of Ablation

Using Equations 3.39, 3.40a, and 3.40b to define $\dot{m}''_{tot}$, $\dot{m}''_{g}$, and $\dot{m}''_{mech}$ in Equations 2.23 and 3.6, and nondimensionalizing the result, we obtain

$$-\phi + Da_M \frac{(1-\phi)}{(\theta+1)} exp\left(\frac{-\gamma}{\theta+1}\right) {v_{ox}}^* \left(B_{ox,max}(1-\phi)+1\right) = 0 \tag{3.50a}$$

$$-\theta + Da \frac{(1-\phi)}{(\theta+1)} exp\left(\frac{-\gamma}{\theta+1}\right) \left[H{v_{ox}}^* - H_{sp}{v_{mech}}^*\right] + \frac{\alpha \dot{q}''_{ext}}{hT_\infty} - \frac{\varepsilon\sigma {T_\infty}^3}{h}\left[(\theta+1)^4 - \left(\frac{T_{surr}}{T_\infty}\right)^4\right] = 0 \tag{3.50b}$$

where

$$B_{ox,max} = rY_{O_2,\infty}, \qquad H_{sp} = \frac{rc_{p,C}[T_\infty(\theta+1) - T_T]}{\Delta i_{comb,O_2}}$$

Because we now must consider the three different B numbers formulated in Equation 3.8, the distinction is made that $B_{ox,max}$ is the maximum value associated with purely thermochemical degradation.

The three B numbers are now formulated as

$$B_{ox} = \frac{\dot{m}''_g}{h_m} = B_{ox,max} Da_M \frac{(1-\phi)}{(\theta+1)} exp\left(\frac{-\gamma}{\theta+1}\right) {v_{ox}}^* \tag{3.51a}$$

$$B_{tot} = \frac{\dot{m}''_{tot}}{h_m} = B_{ox,max} Da_M \frac{(1-\phi)}{(\theta+1)} exp\left(\frac{-\gamma}{\theta+1}\right) {v_s}^* = B_{ox}\frac{{v_s}^*}{{v_{ox}}^*} \tag{3.51b}$$

$$B_{sp} = \frac{\dot{m}''_{mech}}{h_m} = B_{ox,max} Da_M \frac{(1-\phi)}{(\theta+1)} exp\left(\frac{-\gamma}{\theta+1}\right) {v_{mech}}^* = B_{ox}\frac{{v_{mech}}^*}{{v_{ox}}^*} \tag{3.51c}$$

Simplifying Equations 3.50 using Equations 3.51 yields

$$-\phi + \frac{B_{ox}}{B_{ox,max}}\left(B_{ox,max}(1-\phi)+1\right) = 0 \tag{3.52a}$$

$$-\theta + \frac{Da}{Da_M}\frac{B_{ox}}{B_{ox,max}}\left[H - H_{sp}\frac{{v_{mech}}^*}{{v_{ox}}^*}\right] + \frac{\alpha \dot{q}''_{ext}}{hT_\infty} - \frac{\varepsilon\sigma {T_\infty}^3}{h}\left[(\theta+1)^4 - \left(\frac{T_{surr}}{T_\infty}\right)^4\right] = 0 \qquad 3.52b$$

It is apparent from Equation 3.52b that the surface temperature will decrease in the presence of spallation because the term including H_{sp} is an enthalpy loss term. However, because the enthalpy of combustion is generally much larger than sensible enthalpy terms, we expect that $H \gg H_{sp}$ and the temperature decrease will be very slight. Only when ${v_{mech}}^* \gg {v_{ox}}^*$ and the mass loss due to spallation is very high do we expect to see significant reduction in the surface temperature.

Finally, $\overline{Da}$ is adjusted to obtain

$$\overline{Da} = Da_M(\theta+1)^{-1} exp\left(\frac{-\gamma}{\theta+1}\right){v_{ox}}^* \qquad 3.53$$

3.3.3.3 A Model for Determining ${d_c}^*$

The new spallation model in the ablation code is parameterized completely by U, which is available from pyrolysis submodeling, and ${d_c}^*$, which is hitherto undefined. In this subsection we derive a model for ${d_c}^*$ based on the interaction of the ablating surface with the external flow field.

We assume that the carbon fiber preform is a weave of carbon fibers, randomly oriented, homogeneous and isotropic. For the randomly woven mass, each carbon fiber will contact a large number of other fibers, and the average distance between two adjacent points of contact on any fiber is called the effective length, Δ. Although each complete fiber should be modeled as a multispan beam, we simplify the problem and consider each effective length of fiber, or subfiber, to be fixed at both points of contact, except for the subfibers at the surface, which are modeled as cantilevered beams fixed at only one end. Because the effective length is expected to be much smaller than the oxygen penetration depth, each subfiber is assumed to have a constant diameter equal to the average diameter at its location. Each subfiber at the surface is loaded by drag from the external flow, and it is assumed to break at its base when the stress there equals the

flexural strength of the carbon fiber. What must now be obtained is a representation for the effective subfiber length Δ and the aerodynamic loading of the subfibers at the surface.

We model the random array of fibers in the unoxidized state as a three-dimensional grid, with one unit cell shown in Figure 3.19. The initial solid volume fraction φ_o is then

$$\varphi_o = \frac{3V_{fiber}}{V_{total}} = \frac{3\left(\frac{\pi}{4}{d_o}^2\right)\Delta}{\Delta^3} = \frac{3\pi}{4}\left(\frac{d_o}{\Delta}\right)^2 \qquad 3.54$$

This assumes that the aspect ratio Δ/d_o is large, so that the overlap of the fibers at the corners is negligible. This relation defines Δ as

$$\frac{\Delta}{d_o} = \left(\frac{3\pi}{4\varphi_o}\right)^{1/2} \qquad 3.55$$

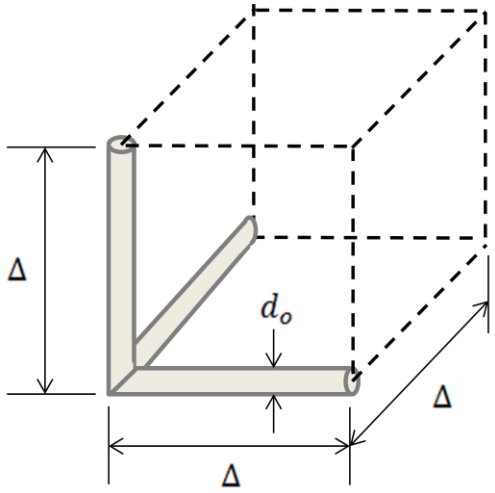

Figure 3.19: Unit cell for carbon fiber preform.

The overall force distribution and associated freebody diagram for a subfiber at the surface is shown in Figure 3.20. The bending moment at the base of the subfiber is

$$M = F_d l_{bend} \sin\theta \qquad 3.56$$

where l_{bend} is the point of application of the drag force. Defining $r_{bend} = l_{bend}/\Delta$ this becomes

$$M = F_d \Delta r_{bend} \sin\theta \tag{3.57}$$

The maximum stress in the fiber at the base is

$$\sigma = \frac{32M}{\pi d^3} = \frac{32F_d \Delta r_{bend} \sin\theta}{\pi d^3} \tag{3.58}$$

When $d = d_{cr}$, the stress equals the ultimate flexural strength, or

$$\sigma_u = \frac{32F_d \Delta r_{bend} \sin\theta}{\pi {d_{cr}}^3} \tag{3.59}$$

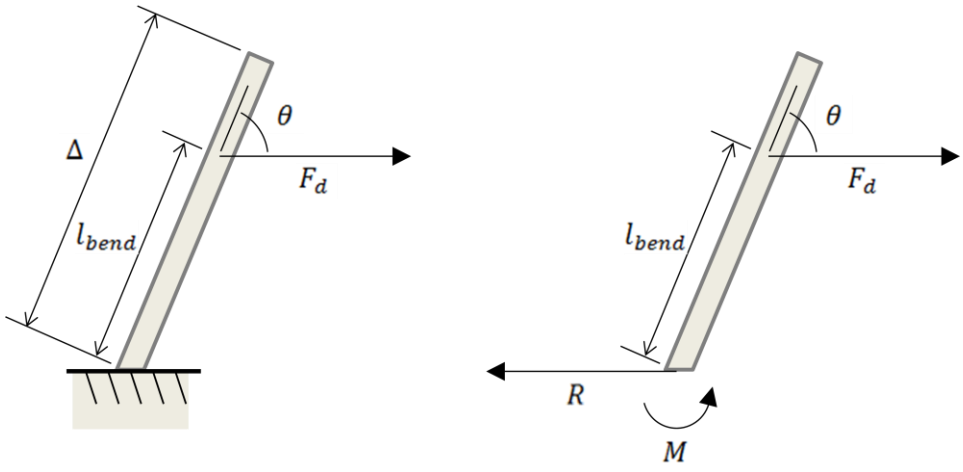

(a) (b)

Figure 3.20: Force distribution on subfiber at ablating surface (a), with accompanying freebody diagram (b).

We assume that the macroscopic friction drag on the ablating surface is the sum of the drag forces acting on the individual exposed subfiber protuberances. The drag on an individual subfiber can then be formulated by determining the amount of the overall surface friction drag (which is available experimentally) that each subfiber contributes. We assume that the surface drag is distributed entirely onto the first layer of subfibers, which are those modeled as cantilevered beams. While the external flow may penetrate past this first layer, it is reasonable to expect that the first layer contributes at least the majority of the overall drag force, and we will assume that it contributes all of it in this model.

Looking at the unit cell of Figure 3.19, we see that the macroscopic drag force generated by a surface element of area Δ^2 is the sum of the drag forces F_d on three subfibers. In terms of the macroscopic surface shear stress τ_s (which is experimentally measurable), this can be stated as

$$\tau_s \Delta^2 = 3F_d \tag{3.60}$$

Equation 3.59 then becomes

$$\frac{\sigma_u}{\tau_s} = \frac{32 r_{bend} \sin\theta}{3\pi} \left(\frac{\Delta}{d_o}\right)^3 \left(\frac{d_o}{d_{cr}}\right)^3 \tag{3.61}$$

Substituting for Δ/d_o using Equation 3.55 and defining a nondimensional drag ratio $\sigma_d = \tau_s/\sigma_u$ we obtain

$$\sigma_d{}^{-1} = \frac{32 r_{bend} \sin\theta}{3\pi} \left(\frac{3\pi}{4\varphi_o}\right)^{3/2} d_c{}^{*-3} \tag{3.62}$$

Rearranging for $d_c{}^*$ yields

$$d_c{}^* = \sigma_d{}^{1/3} \varphi_o{}^{-1/2} \left[4 r_{bend} \sin\theta \, (3\pi)^{1/2}\right]^{1/3} \tag{3.63}$$

It is assumed that the fibers are randomly oriented, so that θ has a uniform distribution on the interval $\left[0, \frac{\pi}{2}\right]$. The average value of θ is then $\frac{\pi}{4}$, which gives an average value for $\sin\theta$ of $\frac{\sqrt{2}}{2}$. The final result is

$$\begin{aligned} d_c{}^* &= C \sigma_d{}^{1/3} \varphi_o{}^{-1/2} \\ C &= \left[2 r_{bend} (6\pi)^{1/2}\right]^{1/3} \end{aligned} \tag{3.64}$$

The value of r_{bend} is difficult to determine because of the complexity of the flowfield at the ablating surface. It is expected that r_{bend} will be between $1/2$ and 1, and values of C for $r_{bend} = 1/2$, $2/3$, and 1 are 1.63, 1.80, and 2.01 respectively. We choose an intermediate value of $C = 1.8$ for the forthcoming work.

The variability of $d_c{}^*$ with σ_d and φ_o is shown in Figure 3.21. As the initial solid volume fraction decreases for a given σ_d, the required reduction in diameter decreases. Likewise, if the surface shear stress increases for a given φ_o, the required reduction in diameter also decreases.

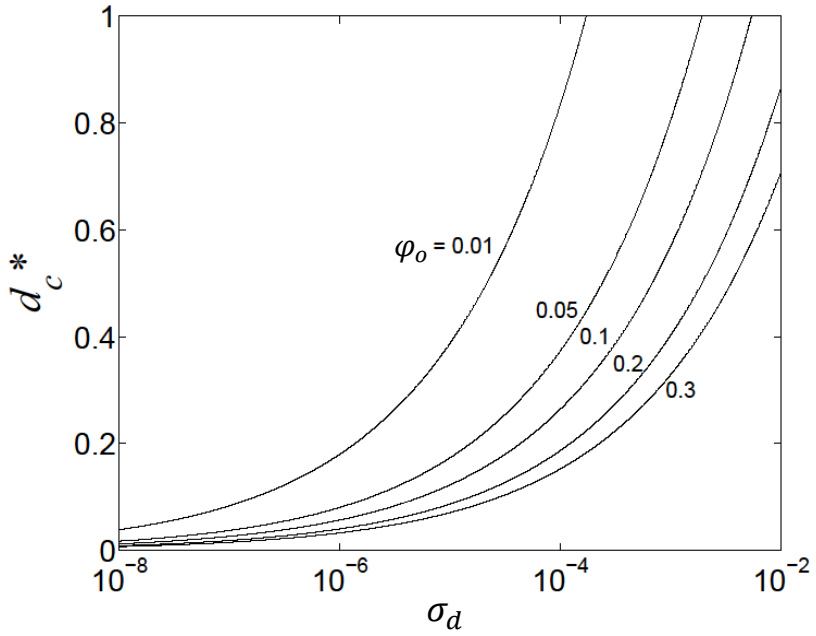

Figure 3.21: Dependence of d_c^* upon σ_d and φ_o.

3.3.3.4 Exploration of Mechanical Erosion in a Reentry Scenario

Finally, the newly developed model for thermo-chemo-mechanical erosion of PICA is tested on a realistic reentry trajectory: the return of the Stardust Sample Return Capsule (SRC). The Stardust vehicle performed a flyby on the comet Wild-2, collected samples from the comet's coma, and returned to earth at a reentry velocity of around 12.9 km/sec, which is currently the fastest reentry velocity ever attempted [30]. The SRC was protected by PICA and had geometry as shown in Figure 3.22. Of interest to the current analysis is the geometry of the nose region, which has a radius $R_n = 0.2202$ m. The curved nose merges smoothly into a cone after 30.5° from the vehicle's longitudinal axis.

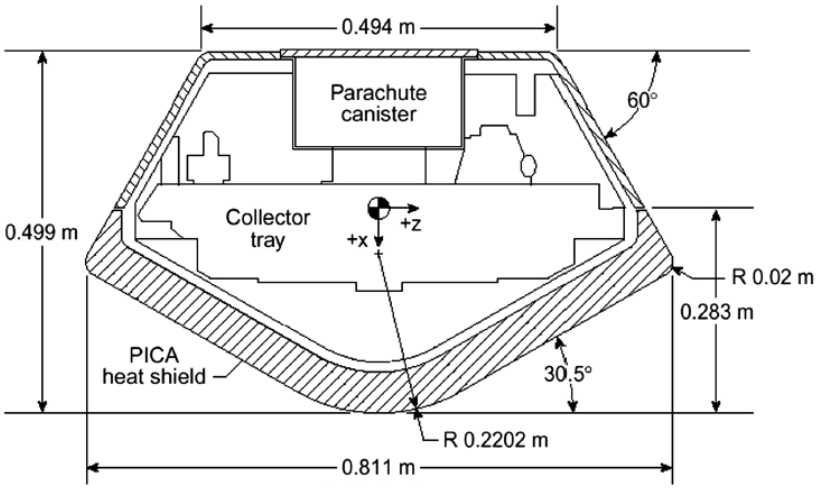

Figure 3.22: Geometry of Stardust SRC, reproduced from [33].

We simulate the point on the trajectory at an altitude of 71 km, where the freestream Knudsen number is 0.001 and the flow is in the continuum regime. This scenario was modeled by Boyd et al. [33] using direct simulation Monte Carlo (DSMC) and continuum computational fluid dynamics methods, and their results will be compared to the current calculation.

We wish to locate the region on the TPS with the highest shear stress, which will produce the highest mechanical erosion rate. In the stagnation region, we expect that the shear stress will be zero at the stagnation point and will rise as distance from the stagnation point increases. Once the cone portion is reached, the flow behaves as a boundary layer on a flat plate with a favorable pressure gradient, in which case the boundary layer may thin, thicken, or remain the same thickness. Because mechanical erosion is not a widely addressed problem, it is very difficult to locate information regarding the shear stress across the face of the Stardust SRC. However, Wilmoth et al. [34] performed DSMC calculations on the SRC at a Knudsen number of 0.136 (slip regime) and determined that the shear stress rises from a low value across the rounded nose to assume an approximately constant value along the conical face of the ablator. While this cannot be used to prescribe the shear stress in a continuum flow, it gives an indication that the shear stress achieves its maximum value at the edge of the nose region

and is roughly constant thereafter. We will therefore analyze the point at the edge of the nose region, which is the interface between the nose and cone portions of the SRC.

The task is now to estimate the shear stress, τ_w, at the edge of the nose region. This can be done using the Reynolds analogy, which states that in scenarios in which the thermal and velocity boundary layers are similar, heat and momentum transfer are analogous and can be determined from one another. The Reynolds analogy is, generally,

$$\frac{C_h}{C_f} = fcn(Pr, geometry) \tag{3.65}$$

where C_h is the Stanton number, C_f is the coefficient of friction, and Pr is the Prandtl number. We define the Stanton number and coefficient of friction according to the preshock freestream velocity U_∞ as

$$C_h = \frac{h}{\rho_\infty c_p U_\infty} \tag{3.66a}$$

$$C_f = \frac{\tau_w}{\frac{1}{2}\rho_\infty {U_\infty}^2} \tag{3.66b}$$

The Reynolds analogy is very dependent upon pressure gradient, so the rounded nose of the SRC presents a problem.

Blottner [35] performed finite difference calculations for heat transfer and shear on an axisymmetric hyperboloid and determined the effect of geometry on the Reynolds analogy. He observed that near the vertex of the hyperboloid, the ratio C_h/C_f is highly variable, but as the hyperboloid approaches its asymptotes, the ratio C_h/C_f is approximately equal to one, and the Reynolds analogy holds. Therefore, since the SRC should have boundary layer behavior similar to that of the hyperboloid, we assume that the Reynolds analogy does not hold in the nose region of the SRC and does hold at the edge of the nose and along the cone. The ratio C_h/C_f is of order 1 when the Reynolds analogy holds, so for the coming calculation we assume

$$\frac{C_h}{C_f} = \frac{hU_\infty}{2c_p\tau_w} \approx 1 \tag{3.67}$$

It now remains to calculate h, which is also required for the convective heat transfer term in the energy balance. Anderson [36] collects heat transfer results for a variety of round nosed objects, including an unswept cylinder (Koppenwallner [37], experimental data), a hemisphere cylinder (Kemp et al. [38], experimental data and theory), and the axisymmetric hyperboloid already discussed (numerical solution). Heat transfer data are also available for Stardust in [33] and [34]. These results are collapsed in Figure 3.23 in terms of $Nu_{R_n}/Nu_{R_n,o}$, which is the ratio of the local Nusselt number to the stagnation point Nusselt number (the Nusselt number in this sense is defined as $Nu_{R_n} = 2hR_n/k$). The noise in the results from [35] and [34] is due to the difficulty of extracting data from the available plots.

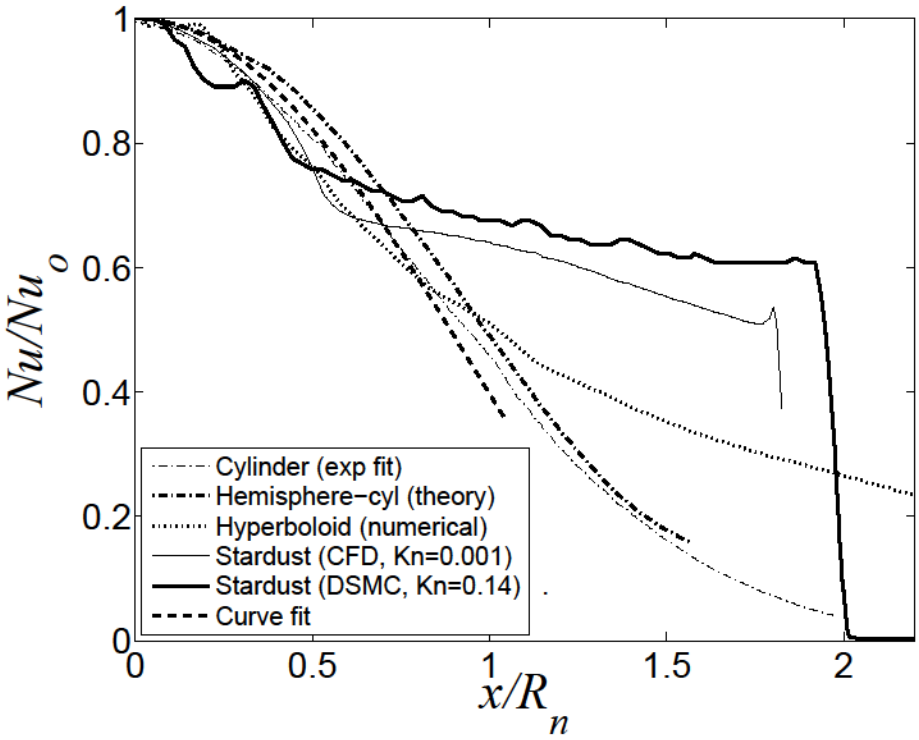

Figure 3.23: $Nu_{R_n}/Nu_{R_n,o}$ for several round-nosed bodies, with approximate curve fit.

Figure 3.23 shows that all round-nosed shapes have similar behavior in the nose regions. When the geometry begins to deviate from the rounded nose geometry (along the cone for Stardust and near the asymptotes for the hyperboloid) the curves diverge from the results for simple shapes like the unswept cylinder. We are interested in the region at the edge of the SRC's rounded nose ($x/R_n = 0.53$), which still behaves approximately like the unswept cylinder. Beckwith and Gallagher [39] give a curve fit for the Nusselt number along an unswept cylinder, which is adjusted slightly for this work. The adjusted curve fit is shown in Figure 3.23 and is stated as follows:

$$\frac{Nu_{R_n}}{Nu_{R_n,o}} = cos^{3/2}\left(\frac{x}{R_n}\right) \tag{3.68}$$

The final step is to calculate the stagnation point heat transfer coefficient. A classic model was developed by Fay and Riddell [40] and has been simplified by [41] and [1] for the current stagnation point scenario. The stagnation point heat transfer coefficient h_o is modeled as

$$h_o = \frac{0.537\sqrt{2}}{Pr^{0.6}} c_p \left(\rho_{e,st}\mu_{e,st}\right)^{0.4} \left(\rho_w \mu_w\right)^{0.1} \left(\frac{1}{R_n}\sqrt{\frac{2\left(p_{e,st} - p_\infty\right)}{\rho_{e,st}}}\right)^{1/2} \tag{3.69}$$

where the subscript st refers to the stagnation values of properties at the postshock boundary layer edge.

Other minor modeling adjustments are as follows. Property values are propagated from the preshock gas (freestream, subscript ∞) to the postshock gas (boundary layer edge, subscript e) using the standard shock relations which can be found in most fluid mechanics textbooks [42]. For heat transfer in compressible flow, the adiabatic wall temperature is used to account for the effects of viscous dissipation in boundary layer heat transfer. The adiabatic wall temperature, T_{aw}, is defined as

$$T_{aw} = T_e + r\frac{{U_e}^2}{2c_p} \tag{3.70}$$

where r is called the recovery factor and is approximately equal to $Pr^{1/2}$. The effects of compressibility can be incorporated into the simplified model by replacing T_∞ by T_{aw} in the mass and energy balances (Equations 3.52), the definitions of ϕ and θ, and the

definition of the Damkohler number Da. Additionally, Lachaud et al. [31] indicate that the oxidation of carbon fibers by only molecular oxygen (Equation 2.20) is a reasonable approximation near the stagnation region of the SRC, and this assumption is used here.

We are now in a position to simulate thermo-chemo-mechanical ablation of the Stardust SRC at a point at the beginning of the conical section. This simulation models the same scenario as that of Boyd et al., who model the point along the trajectory at an altitude of 71 km, where the capsule velocity is 12,063 m/sec, or $Ma_\infty = 40$. Boyd et al. do not model the decomposition of the ablator, only the flowfield around the capsule, and thus do not give sufficient information to characterize the ablation of PICA. Lachaud et al. [31] also model the Stardust SRC, and they analyze the peak heating condition, which is close to the condition analyzed by Boyd et al. Information not given by Boyd et al. (such as D_{eff}, φ_o, d_o) is taken from Lachaud et al. for their slightly different scenario, which is similar enough for the current approximate analysis. The flexural strength of carbon fibers is estimated from Fitzer and Manocha [43]. Nominal values for all parameters used in the model are tabulated in Table B.3 in Appendix B.

The simplified model compares reasonably well to the results of the more advanced simulation, considering its limitations. Table 3.1 shows results for the wall temperature and surface heat flux produced by the simplified model and by Boyd et al. Also shown is a steady state recession rate estimated from the results of Lachaud et al. [31], who performed direct numerical simulation on PICA, modeling the individual fibers and the matrix, at the Stardust peak heating condition ($T_w = 3360$ K).

Table 3.1: Comparison of simplified model to literature simulations.

Parameter	Simplified Model	Literature Numerical Simulation
T_w	3070 K	2700 K [33]
$\dot{q}''_{surf}$	4.1 MW/m^2	5.5 MW/m^2 [33]
v_s	0.02 mm/sec	0.005 mm/sec [31]

The total B for the simulation was calculated to be 0.064, which puts the system in the kinetically controlled regime. This makes sense because the reactivity of carbon

fibers is lower than that of the graphite ablator examined earlier. The ratio of B_{sp} to B_{tot} is 0.0014, so spallation mass loss is 0.1% of the total mass loss, which is negligible. We may therefore conclude that mechanical erosion by the removal of small carbon fiber particles was not important in the Stardust reentry process, which is a testament to the durability of PICA. This result is somewhat anti-climactic, and it is tempting to propose that the calculated surface shear stress, 296 Pa, was too low, and that the Reynolds analogy was used incorrectly. We may address this issue briefly through comparison to the shear stress calculations of Wilmoth et al. in the slip regime. Reformulating our description of the Reynolds analogy (Equation 3.67) gives

$$\frac{C_h}{C_f} = \frac{\dot{q}''_{surf} U_\infty}{2 c_p \tau_w (T_{aw} - T_w)} \approx 1 \qquad 3.71$$

Assuming that the freestream velocity, specific heat, and temperature difference are roughly the same between the calculations of Wilmoth et al. and the current calculation (a very rough assumption), the ratio of the surface heat flux to the shear stress should be similar (or at least within an order of magnitude). This ratio for Wilmoth et al. is $\dot{q}''_{surf}/\tau_w = 15$ kW/N, and for the simplified model it is $\dot{q}''_{surf}/\tau_w = 13.5$ kW/N. These values are within the same order of magnitude, so the shear stress calculated for the simplified model is reasonable.

In order to better understand the thermo-chemo-mechanical erosion of the porous PICA, the freestream velocity was varied over a wide range. Varying U_∞ from 3,000 m/s to 15,000 m/s (around the nominal value of 12,063 m/s used thus far) produced wall temperatures ranging between 1,000 K and 3,500 K, approximately. Values for B_{tot}, B_{ox}, and B_{sp} for this temperature range are shown in Figure 3.24a. Throughout the whole range, mechanical erosion produces a negligible amount of mass loss, and the B_{tot} and B_{ox} curves are essentially identical. The Stardust scenario is also indicated as a single point (circle). Figure 3.24b plots the B numbers in terms of $\overline{Da}$, along with the simple $\overline{Da}$ model (Equation 2.74). This shows that, due to the low reactivity of carbon fibers (as given by Lachaud et al. [31]), PICA is in the kinetically controlled regime throughout this scenario.

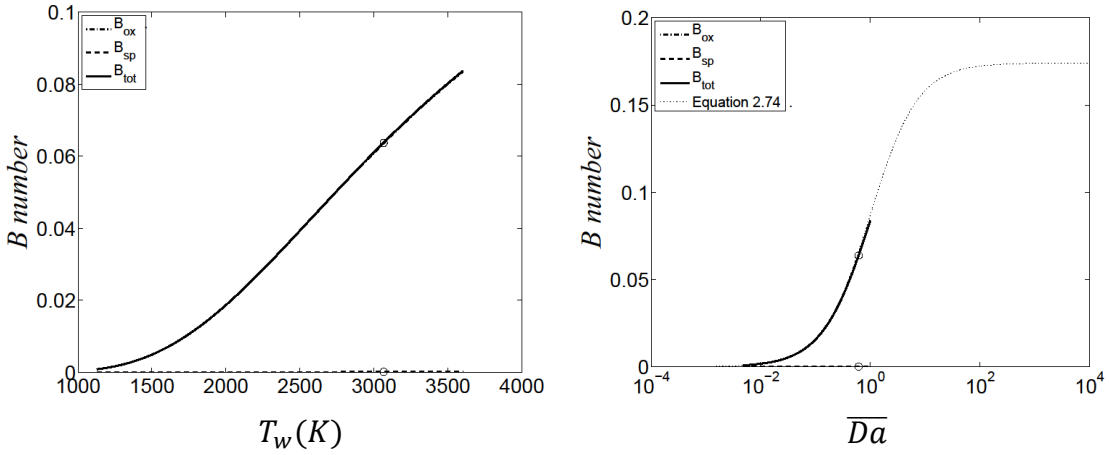

(a) (b)

Figure 3.24: B number values for a range of values of T_w (a) and $\overline{Da}$ (b).

Figure 3.25 plots the variation of the oxygen penetration depth, δ_{ox}, calculated from Equation 3.17c, with the wall temperature. Also plotted is the subfiber length Δ, calculated from Equation 3.55. For this case, with $d_o = 10$ μm and $\varphi_o = 0.1$, the subfiber length is 48 μm. In order for the oxidation model to be valid, the subfiber length must be much smaller than the oxygen penetration depth, so that the diameter of each subfiber is approximately constant. This ratio, δ_{ox}/Δ, gives the number of affected subfibers, and it is also shown in Figure 3.25. It is clear that this assumption is valid for the Stardust simulation, for all reentry velocities below that of Stardust, and for a small range of higher velocities.

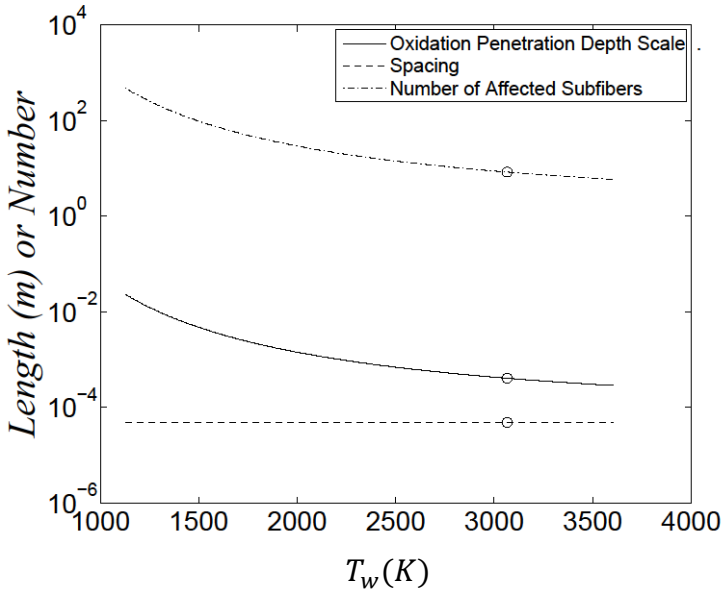

Figure 3.25: Variation of oxygen penetration depth with T_w, along with number of affected subfibers.

Finally, Figure 3.26 shows the recession rate as a function of wall temperature. As expected, higher reentry velocities, and thus higher wall temperatures, result in significantly higher recession rates for PICA.

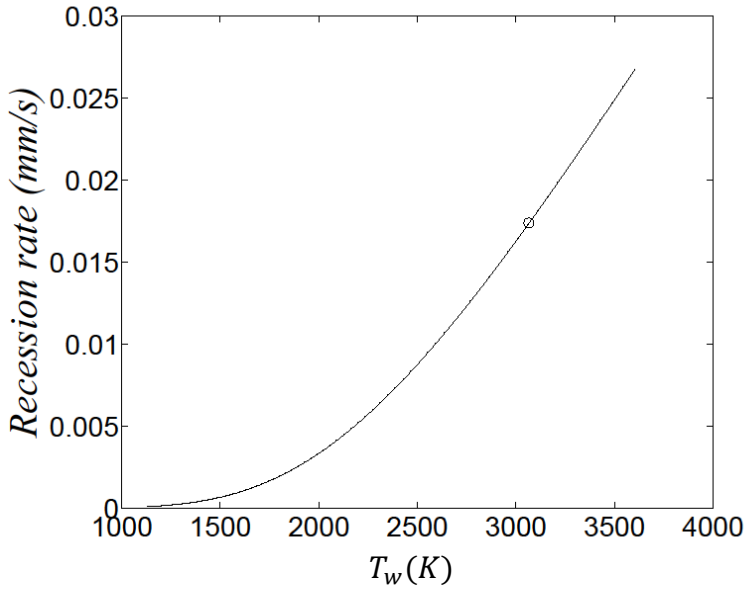

Figure 3.26: Recession rate versus T_w for reentry conditions similar to that of Stardust.

The preceding analysis shows that, although mechanical erosion was not important in the Stardust reentry scenario, the thermo-chemo-mechanical erosion model developed is a good predictor of the behavior of PICA in reentry scenarios. Even the simplified model produced respectable quantitative results, and one imagines that more complex modeling of surface chemistry, pyrolysis, and aerothermochemistry will produce better quantitative results. Of particular importance is the introduction of the porous solid model into the quasi-steady-state formulation, which accounts for the effects of a finite thickness oxidation zone, blowing of pyrolysis gases, and mechanical erosion of fibers at the surface. All of these effects are relevant to materials with a carbon fiber preform in a phenolic matrix, such as PICA.

This model shows that mechanical erosion is not important for PICA. This has been confirmed by both postflight evaluation of the Stardust SRC (Stackpoole et al. [30]) and by arc jet tests of PICA in high shear environments (Driver et al. [44] and Driver et al. [45]). Even for the highest expectable values of surface shear stress (600 Pa [44]), the current model shows negligible mechanical erosion. The reason for this is the extremely high strength of carbon fibers [43], the relatively dense packing of these fibers in the preform (which reduces the effective fiber length), and the relatively low surface shear stress obtainable with gaseous boundary layer flows. It is worth noting that the strength of carbon fibers after oxidation damage has not been investigated extensively. As Figure 3.7b indicates, the oxidized surface of a fiber is rough and pitted, and the defects developed may reduce the fiber's flexural strength considerably. It is possible that experimental determination of the strength of oxidized carbon fibers would increase the contribution of mechanical erosion of PICA to a non-negligible level, but based on experimental results elsewhere in the literature, it is still likely to remain small. All things considered, PICA has come to the forefront of ablative TPS materials for a number of reasons, including its low density and durability in thermochemical erosion. To this list we now add the following: its excellent resistance to mechanical erosion in oxidizing environments.

In the pursuit of a material which is susceptible to mechanical erosion and fits the previously derived model, other ablative TPS materials were considered. Unfortunately, no material currently available fits the model requirements, as materials with glass or silicone fibers do not undergo oxidation. However, the currently developed model may be useful in the future, since flexible TPS materials with weaker carbon fibers are plausible for use in balloon-type thermal protection systems. It could also be useful in a scenario in which mechanical grinding replaces boundary layer drag on the surface, in which case the shear stress applied to the surface will be orders of magnitude higher. The model may also be adapted to reactions other than carbon oxidation; the framework and methodology developed are not dependent upon the reaction modeled.

3.4 CONCLUSIONS

Mechanical erosion of thermochemically ablating systems has been modeled from several points of view. Mechanical erosion was investigated from the point of view of a grinding problem and with an arbitrarily defined spallation mass loss rate. Finally, a physics based mechanical erosion model was proposed for PICA, in which oxidation of bare carbon fibers makes them susceptible to breakage by an external flow. Only the removal of individual carbon fiber segments was considered in the model; the ejection of large chunks of carbon fibers by thermal fracture or pyrolysis gas pressure was not considered. The model was created by deriving conservation equations for oxygen and for average fiber diameter within a thin zone at the surface of a porous carbon preform in the presence of outflowing pyrolysis gases and a shearing boundary layer flow. These equations were solved numerically, and an approximate solution was discovered that states the overall recession rate explicitly in terms of a nondimensional pyrolysis gas blowing velocity and a nondimensional critical diameter at the surface.

The mechanical erosion model was incorporated into the existing carbon oxidation model, and an effective fiber reactivity was observed which combines the dependencies of chemical kinetics and transport within the porous medium. This model was then applied to the Stardust SRC reentry scenario and was shown to produce acceptable agreement with more advanced calculations.

The model developed in this chapter illustrates a system in which mechanical erosion is brought about by thermochemical erosion, so the mechanical loss of mass is dependent upon the rate at which thermochemical erosion proceeds. In this situation, the mechanical erosion rate was determined through mechanical considerations, but the driving behavior of mass loss was governed by thermochemical effects, and mechanical effects provided an adjustment to the thermochemical mass loss formulation. There exist situations, however, in which mechanical effects are the driving mass loss mechanism, and thermochemical considerations provide an adjustment. For instance, for a lattice structure subject to high loading and slow thermochemical erosion, we expect that mass loss will occur mostly as large chunks fractured from the surface, and very little mass will be lost in the gas phase. Thermochemical erosion may affect the properties or create defects in the surface of the material, but the driving behavior of mass loss is the fracture of a framed structure. In this case, the governing equations for mass loss are those that describe the stress distribution through the structure and the fracture mechanics of the material, rather than the mass and energy balances and chemical rate equations used in the current work.

From a design point of view, it is essential to determine what is actually important in the system. There can be situations where mechanical effects augment a chemical erosion model, chemical effects augment a mechanical erosion model, and where the dominant behavior must be understood by considering both physical domains. In this case, a model has been developed for thermochemical erosion in which mechanical effects provide an augmentation to the overall recession rate. This is certainly not the only mass loss mechanism, as work has been done on the ejection of large chunks for TPS materials [21, 29]. The author hopes that the current work will contribute to the understanding of systems in which thermochemical erosion precipitates mechanical erosion and looks forward to seeing work in which the relative importance of chemical and mechanical processes differs from that studied herein.

The Stardust simulation showed that mechanical erosion of fibers at the surface which is precipitated by thermochemical mass loss is not an important mass loss

mechanism for PICA. This has been confirmed elsewhere in the literature [30, 44, 45]. Even though the model proves itself to be nonessential in the design of systems utilizing PICA, the mechanism of mechanical removal of particles as a result of thermochemical degradation should not be dismissed. Materials may be developed in the future which sacrifice the mechanical durability of PICA for advantages elsewhere, and the methodology developed here may prove useful. Also, the mechanical removal of thermochemically degraded solid particles is not the exclusive territory of TPS materials. As we shall see in the following chapter, the methodology developed here extends naturally into the realm of wildland fire modeling, where the mechanical removal of thermochemically degraded mass is of great importance.

Chapter 4: Firebrand Generation in Wildfires

The interplay between thermochemical and thermomechanical degradation mechanisms is not exclusive to ablative TPS materials. As we shall see in this chapter, this feature is present in an entirely different realm of study: the generation of brands in a wildland fire front.

The lofting of embers, or brands, from large-scale wildland fires is an important mechanism in the spreading of these fires. For fires in which brands are not produced, such as liquid pool fires or fires over solids which do not undergo mechanical erosion, the flame spread rate may be described by wind-opposed or wind-aided flame spread models [46-47], in which the virgin fuel is heated to the pyrolysis or ignition temperature by radiation from the flame. In these models, flame spread occurs as a movement of the flame front due to the gradual heating of the adjacent fuel. For fires which produce brands, the flame spread process is not as simple, because lofted brands may be carried far ahead of the preheat region and start spot fires. These spot fires cause the fire to spread more quickly than traditional flame spread models predict, and it is therefore essential to account for flame spread due to brand lofting in large-scale fires.

Brand lofting may be thought of as a three-stage process. In the first stage, brands are generated within the parent fire by mechanical removal of particles due to interaction with the flow of the fire plume. In the second stage, the brands are transported upwards within the plume and carried to a high altitude by the buoyant flow of the plume. In the third stage, the brands exit the plume and are carried by wind (whose mean velocity is roughly horizontal) ahead of the flame front and deposited on the ground. Throughout the whole process, each brand is pyrolyzing and losing mass, and depending on the type of fuel and the initial dimensions of a brand, it will either burn out harmlessly in the air or survive the lofting process and land with sufficient mass and thermal energy to start a spot fire.

Because the brand transport process is so complicated, accurate modeling of each stage is necessary in order to obtain a model with valuable predictive capabilities. Much analysis has been done on the plume lofting and wind propagation stages of the lofting

process [48-53], and significant experimental work has been done to characterize the size and number distribution of brands generated and their effects on fire spread [54-57], but relatively little has been done on the generation of brands within the parent fire. This work focuses on that stage, creating a model for the breakage of brands from branching structures due to interaction with the fire plume. This is done by addressing the structure of wildland fuels, the thermochemical degradation process for branching elements, and the aerodynamic loading on an individual branch within the fire. With these three pieces, we develop a methodology which makes it possible to determine the population of brands which is able to be lofted, which can be used as an input to a suitable lofting and propagation model. To demonstrate the utility of the brand generation model, it is then coupled to a simplified version of a plume and propagation model created by Woycheese et al. [48-49], and the complete model is used to predict the mass distribution and propagation distance of embers in a wildland fire case study.

4.1 STRUCTURE OF WILDLAND FUELS

For fuels which have dendritic or branching geometries, such as wildland vegetation, body forces and shear loading produce stresses on exposed protuberances, making them susceptible to breakage. The distribution of mass in an unburned vegetative fuel is an important starting point for the thermomechanical breakage analysis developed later, so we must begin the development of the brand generation model by analyzing the size and number distribution of branching elements in a tree or bush.

The typical approach for modeling branching vegetative structures in the literature is based on fractal geometry and self similarity, which was first articulated by Mandelbrot [58] and has been incorporated into computational methods for generating realistic tree structures by researchers such as Collin et al. [59], whose work focuses on modeling realistic trees for applications such as flame propagation, fire retardant distribution through a tree canopy, and photosynthesis. Self similarity of a structure says that a fundamental unit of structure exists within the system that is repeated at all scales, so that the structure appears the same at all scales. For botanical trees, this fundamental unit is a single branch which gives birth to a set of smaller branches; this type of behavior is

clearly present at all scales within a botanical tree. Mandelbrot observes that while botanical trees are not perfectly self similar, the assumption that they are self similar in the higher order stages of branching is appropriate. Because the trunk and first stages of branches are too large to be lofted in any realistic time, the assumption of self similarity is appropriate for the higher order branched structures that are the focus of this investigation.

The modeling approach of Collin et al., for deciduous trees specifically, is to assume that the wildland fuel packet consists of I branching stages of cylindrical fibers of diameter D_i and length L_i, as shown in Figure 4.1. It is assumed that the branching stages are self similar, so that both the diameter ratio between successive branching stages (D_{i+1}/D_i) and the aspect ratio $A = L_i/D_i$ are constant with respect to i. It is assumed that each branch element terminates in a junction which gives birth to a specified number of branches for the next stage. The branching ratio n_{i+1}/n_i, where n_{i+1} and n_i are the number of branches in the child and parent stages respectively, is a whole number greater than 1 and is constant with respect to i.

The current model follows the approach of Collin et al. and uses a deciduous tree model with a constant diameter ratio and constant aspect ratio. It is assumed that each branching process is a bifurcation process, where one branch divides into exactly two smaller branches. Additionally, the limbs of the tree are assumed to have no defects and are assumed to not taper, and it is assumed that the trees of interest have lost their leaves and consist of cylindrical fibers only. The geometry of leaves differs greatly from that of branches, and their behavior during thermal degradation and lofting is very different from that of branches and requires additional modeling not addressed here. There are many examples of wildfires that arise in the plains regions of the United States (e.g., in Texas) during the winter season when grasses have cured and trees have lost their leaves. As such, the assumption of leafless trees is not outrageous. Finally, it is assumed that the material of the tree branch is homogeneous. In reality, a tree branch is a composite structure consisting of strong heartwood at the core and generally weaker sapwood at the

exterior. We neglect this composite structure and treat each branch as a homogeneous member with spatially constant properties.

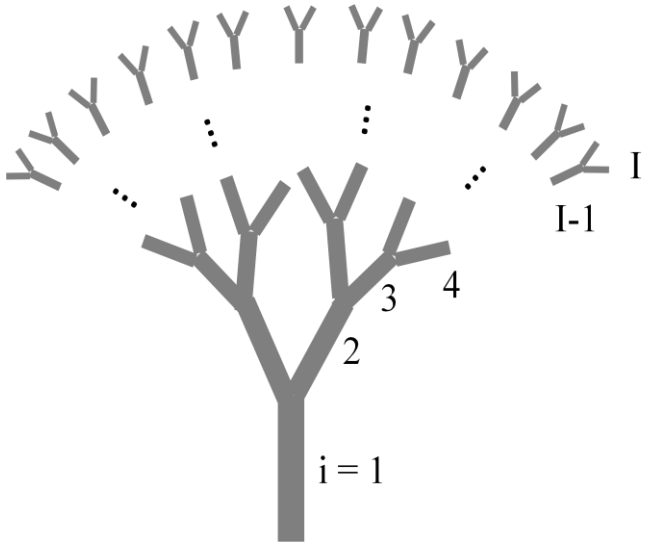

Figure 4.1: Fractal model for branching vegetation wildland fuel packet.

The trajectory and life expectancy for any particular lofted brand is highly dependent upon its initial geometry. Because the available range of geometries for branching wildland fuels is vast, it is important to estimate the distribution of mass and branch sizes for a wildland fuel packet in order to assess its ember lofting potential in a wildfire scenario. The fractal self similarity assumption provides a means to determine the distribution of mass at different levels of branching within a tree. The ratio of mass, m, between two successive stages of branching is

$$\frac{m_{i+1}}{m_i} = \frac{\rho_s V_{i+1}}{\rho_s V_i} = \frac{\rho_s \left[n_{i+1} \left(\frac{\pi}{4} {D_{i+1}}^2 \right) L_{i+1} \right]}{\rho_s \left[n_i \left(\frac{\pi}{4} {D_i}^2 \right) L_i \right]} \qquad 4.1$$

where ρ_s is the solid density and V is the branch volume. Using the aspect ratio A we obtain

$$\frac{m_{i+1}}{m_i} = \frac{\rho_s \left[n_{i+1} \left(\frac{\pi}{4} {D_{i+1}}^2 \right) A D_{i+1} \right]}{\rho_s \left[n_i \left(\frac{\pi}{4} {D_i}^2 \right) A D_i \right]} = \left(\frac{n_{i+1}}{n_i} \right) \left(\frac{D_{i+1}}{D_i} \right)^3 \qquad 4.2$$

Mandelbrot reports that although the diameter ratio D_{i+1}/D_i varies greatly among different species of trees, a generally acceptable value is $D_{i+1}/D_i = 2^{-1/2} \approx 0.71$. Using this and the bifurcation ratio $n_{i+1}/n_i = 2$, we obtain

$$\frac{m_{i+1}}{m_i} = 2\left(2^{-\frac{1}{2}}\right)^3 = 2^{-\frac{1}{2}} \approx 0.71 \qquad 4.3$$

Equation 4.3 suggests that the amount of mass in a stage of branching decreases as the stage's nominal diameter decreases. Recall that this analysis is made for trees with no leaves and a splitting ratio of 2. With leaves, or with a different splitting ratio, one imagines that the mass scaling would be quite different.

4.2 BRAND GENERATION MODEL

With the distribution of mass within a bush or tree known, we now explore the brand generation process by developing a model for a single branch fiber which may be applied to all fibers in the system. The essence of the brand generation model is the idea that, before degradation, fibers are too strong to be removed by environmental forces (as nature intends), but as degradation proceeds, the fibers are weakened enough that they may be removed by external forces. As mass loss associated with thermal degradation occurs for the fibers, their geometry and strength properties may be changed to a point at which fracture occurs, and lofted brands are produced. The thermo-mechanical breakage of branching fibers is modeled by addressing separately the thermal degradation of cellulosic fuels and the aerodynamic loading of components within a fire plume.

4.2.1 Thermochemical Degradation of Branching Vegetative Fuels

For cellulosic elements in a large scale fire, two thermal degradation processes may occur: pyrolysis and oxidation. The first process, pyrolysis, is a chemical reaction at elevated temperature that changes virgin organic matter into a carbonaceous char and gaseous products. Pyrolysis is a volumetric mass loss process, and the gases produced are exhausted from the solid, leaving behind a material with a higher percentage of carbon. During this process, there is a decrease in density and strength of the element, as

well as a reduction in the element's overall dimensions and possibly significant deformation or twisting.

The second process, oxidation, is a chemical reaction that occurs at higher temperatures than pyrolysis and is a reaction between the carbonaceous char and oxygen to produce carbon dioxide or carbon monoxide. Because it requires the presence of gas-phase oxygen, pyrolysis is a surface mass loss process in which material is removed from the surface of the solid, so the surface of the solid recedes with no significant changes to density or strength.

Thermochemical degradation thus proceeds by two different mass loss processes which occur generally in series. Oxidation requires the formation of a carbonaceous char by pyrolysis, but it is possible that surface oxidation may begin before in depth pyrolysis is completely finished. However, for simplicity and because we expect the temperature around a plant to rise monotonically as the flame front approaches, we assume that pyrolysis and oxidation occur exactly in series, and breakage may occur due to either the decrease in strength associated with pyrolysis or the subsequent thinning of fibers due to oxidation. Each of these failure mechanisms must be considered sequentially. The pyrolysis process is modeled to determine whether or not fracture is possible due to pyrolysis only, and if it is not, the time varying mass loss due to oxidation is modeled with post-pyrolysis properties fixed.

Both the evolution of properties through pyrolysis and the time varying oxidation process are modeled in the following subsections. In the subsequent section, this knowledge is combined with an analysis of aerodynamic drag on the degrading fibers to determine if and when a breakage event occurs.

4.2.1.1 Pyrolysis Modeling

As stated, pyrolysis is the conversion of virgin organic matter into carbonaceous char and gas. One possibility for modeling the pyrolysis process is to use an Arrhenius model, with kinetic parameters determined through thermogravimetric analysis (TGA). This has been done with success for several different types of wood by Vovelle et al. [60], who performed TGA in nitrogen on fir, poplar, oak, and cellulose and determined

the associated kinetic parameters. They observed that the pyrolysis of wood consists of two steps; the first step is the pyrolysis of hemicellulose and lignin around 520 K, and the second step is the pyrolysis of cellulose around 620 K. The overall pyrolysis process is modeled by accounting for both of these steps using their associated kinetic parameters.

Using the Arrhenius model, the time varying pyrolysis of each step (subscript $i = 1$ for the low temperature degradation of hemicellulose and lignin and $i = 2$ for the high temperature degradation of cellulose) may be modeled with the following differential equation:

$$\frac{dY_i}{dt} = A(1 - Y_i)^n exp\left(-\frac{E_a}{RT}\right) \qquad 4.4$$

where A is the preexponential factor, n is the reaction order, E_a is the activation energy, R is the universal gas constant, and T is the temperature of the solid. The parameter Y is a nondimensional mass for each step, defined as

$$Y_i = \frac{m_{o,i} - m}{m_{o,i} - m_{f,i}} \qquad 4.5$$

where m is the actual sample mass, $m_{o,i}$ is the mass of the sample at the beginning of each step, and $m_{f,i}$ is the mass of the sample at the end of each step. Vovelle et al. determine the kinetic parameters and the values $m_{o,i}$ and $m_{f,i}$ for each species of wood, assuming that the low temperature process occurs completely before the high temperature process is allowed to occur. This means that $m_{o,1}$ is the original mass of the sample before any degradation occurs (m_o), $m_{f,2}$ is the final mass of the sample after maximum mass loss has occurred (m_f), and $m_{f,1} = m_{o,2}$ is the intermediary value after full degradation of the first step and no degradation of the second step (m_{mid}).

Equation 4.4 with $i = 1, 2$ can be integrated for a prescribed time period and temperature to simulate a wildfire pyrolysis scenario. The time varying profiles for Y_1 and Y_2 can be combined as follows to determine the variation of the total mass with time:

$$m(t) = (m_o - m_{mid})(1 - Y_1(t)) + \left(m_{mid} - m_f\right)(1 - Y_2(t)) + m_f \qquad 4.6$$

The fraction of the original mass remaining is often more useful than the magnitude of the mass. This is obtained by dividing Equation 4.6 by m_o to obtain

$$\frac{m}{m_o} = \left(1 - \frac{m_{mid}}{m_o}\right)(1 - Y_1(t)) + \left(\frac{m_{mid}}{m_o} - \frac{m_f}{m_o}\right)(1 - Y_2(t)) + \frac{m_f}{m_o} \qquad 4.7$$

Figure 4.2 shows the evolution of m/m_o with time for different values of T. The kinetic parameters and values for m_{mid}/m_o and m_f/m_o are taken from Vovelle et al. for poplar. There are several different species of tree commonly referred to as poplar, some of which occupy a genus other than *Populus*. This fact will be important in later experimental investigation, but for now we use the results of Figure 4.2 to identify general trends in the pyrolysis of wood.

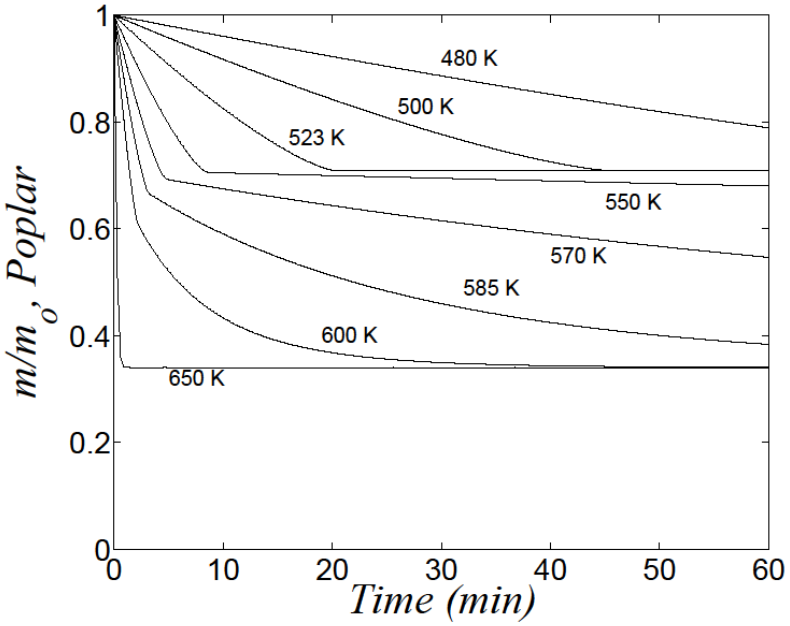

Figure 4.2: Pyrolysis of poplar at different temperatures.

The two steps of pyrolysis are clearly present. For temperatures below approximately 550 K, only the pyrolysis of hemicellulose and lignin is present, and the fraction of mass remaining approaches a value of 0.71. For higher temperatures, both reactions are present, and all curves approach a value of 0.34, which is the maximum mass loss possible for pyrolysis of poplar.

In a wildfire scenario, we expect much higher flame temperatures on the order of 1000 K and much shorter pyrolysis times on the order of minutes. Figure 4.3 shows this

type of scenario. The kinetics produced by Vovelle et al. indicate that for high temperatures, pyrolysis is essentially instantaneous, and full mass loss is achievable after only a few seconds. This mass loss rate is unrealistically high, however, because the analysis assumes that the sample temperature is brought instantaneously to the prescribed pyrolysis temperature. In reality, the sample is heated convectively and radiatively from the environment, and there is a characteristic time required for the sample to heat up to the temperature indicated in the simulation. To illustrate briefly, we may consider a cylindrical element heated convectively to have its interior significantly heated when the Fourier number ($Fo = \alpha t/R^2$) is roughly equal to 1. For a wooden element with thermal diffusivity $\alpha \approx 10^{-7}$ m^2/s and radius $R \approx 1$ cm, the time required to achieve a Fourier number of 1 is approximately 15 minutes. For an element with radius $R \approx 0.5$ cm, the heating time is approximately 4 minutes. There will therefore be a significant variation of the extent of pyrolysis with depth into the specimen and with initial diameter for a real wildfire scenario.

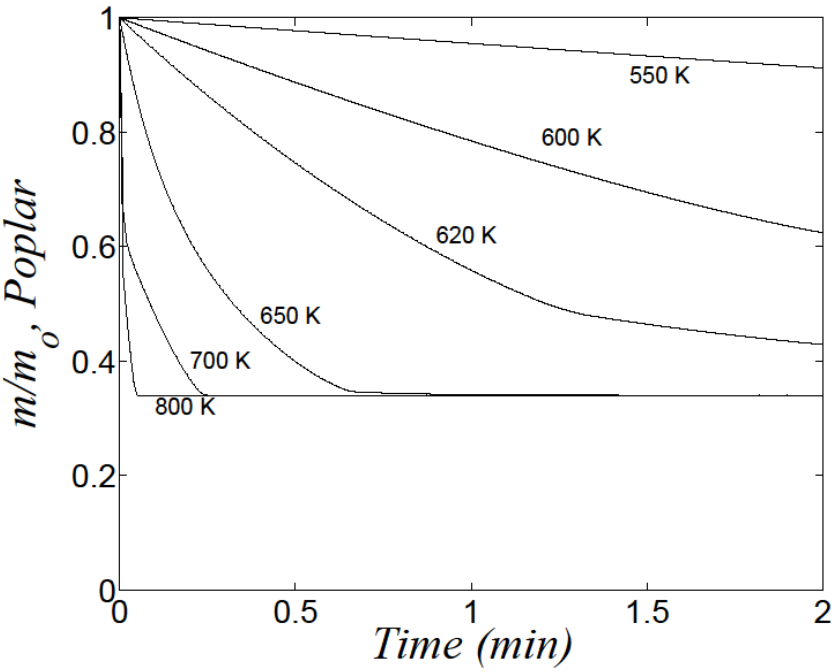

Figure 4.3: Pyrolysis of poplar at different temperatures simulating a wildfire scenario.

Although the pyrolysis process in a wildfire scenario is extremely complex and must include the considerations indicated above, understanding can be gained by investigating a lumped or uniformly degrading system, which is an appropriate assumption for the long time scales considered in Figure 4.2. This situation is much easier to characterize experimentally because the in depth spatial variations of density are not present and the fraction of mass lost or remaining is uniform throughout the sample and may be determined from only the initial and final sample mass. Because the kinetic model allows the pyrolysis of the system to be described in terms of the fraction of mass remaining (m/m_o) or the fraction of mass lost ($1 - m/m_o$), it is now possible to connect the kinetic pyrolysis model with experimental investigations. This is a very important connection to make for the complex system of wood pyrolysis.

The fraction of mass lost or remaining is a useful parameter provided by the kinetic model, but it is not the only quantity of interest in the brand generation model. We also wish to know how the sample's dimensions, density, and strength vary as a function of mass lost. These variations are extremely difficult, if not impossible, to obtain through analytical models for volume and strength change, but they are readily accessible through experiments. We may then find empirical relationships between these properties and the fraction of mass lost, and all properties are then available from the kinetic pyrolysis model.

To obtain the empirical relationships between dimensions, volume, density, flexural strength, and fraction of mass lost, a set of experiments was performed. The behavior of these properties through the pyrolysis process has been studied in some detail [61], but data for specific types of wood are not widely available.

The experiments performed consisted of drying and pyrolyzing sets of wooden dowel rods and testing their flexural strength using three-point bending tests. Yellow poplar (*Liriodendron tulipifera*) dowel rods of different diameters were chosen to approximate the behavior of branches in bending because their geometry is easily measured and the tolerances in their manufacture are generally good. As previously mentioned, there are several different types of wood referred to as poplar, so the kinetic

parameters used so far may not represent yellow poplar, but the two-step reaction should still be observed. Rods of nominal diameter 4.8 mm, 6.4 mm, and 7.9 mm were cut into pieces 20 cm long and divided into four testing groups, with a roughly equal number of rods of each diameter in each group. The first group was tested at ambient conditions (14 ˚C, 90% relative humidity), the second was tested after oven-heating at 101˚C for one hour, the third was tested after oven-heating at 250˚C for one hour, and the fourth was tested after oven-heating at 500˚C for 1.5 hours.

The four groups tested represent four key steps in the pyrolysis process for wood. The first group (control group) represents the undamaged state. The second group represents the completely dried state, where the wood has zero moisture content. The third group, heated at 250˚C, is hot enough that the first reaction (degradation of hemicellulose and lignin) can proceed fully but the second reaction (degradation of cellulose) cannot occur to any appreciable extent. It therefore represents the intermediary state (m_{mid}). The fourth group is hot enough that both reactions proceed fully, and the maximum mass loss state (m_f) is achieved.

The heating treatments carried out were successful in producing the four states desired. Oven-heating the second group resulted in mass loss due to evaporation of moisture but no significant mass loss due to pyrolysis; the dried rods were visually indistinguishable from the unheated rods. Oven-heating the third group resulted in mass loss due to both evaporation and pyrolysis; visual inspection showed that the rods had begun to carbonize. Oven-heating the final group resulted in a large amount of mass loss due to both evaporation and pyrolysis; visual inspection showed that the rods had undergone significant carbonization. The specimens heated to 101˚C and 250˚C both displayed a very slight decrease in volume due to heating, and they remained straight. The specimens heated to 500˚C, on the other hand, displayed a significant reduction in volume and underwent significant warping and bending. This suggests that a different chemical reaction occurs at high temperatures than at low temperatures, one that is capable of significantly changing the structure of the plant cell walls. Because cellulose provides the major structural component in cell walls, it makes sense that the second

reaction was capable of causing such significant shape changes, whereas the first reaction was not. Finally, all heated samples retained their surface features, indicating that no surface reactions occurred and that pyrolysis is indeed a volumetric mass loss process.

Three-point bending tests were performed on all samples to determine their flexural strength, as shown schematically in Figure 4.4. The span of the bending test was 17.8 cm, and the critical load for fracture was observed using either an analog or digital hanging scale.

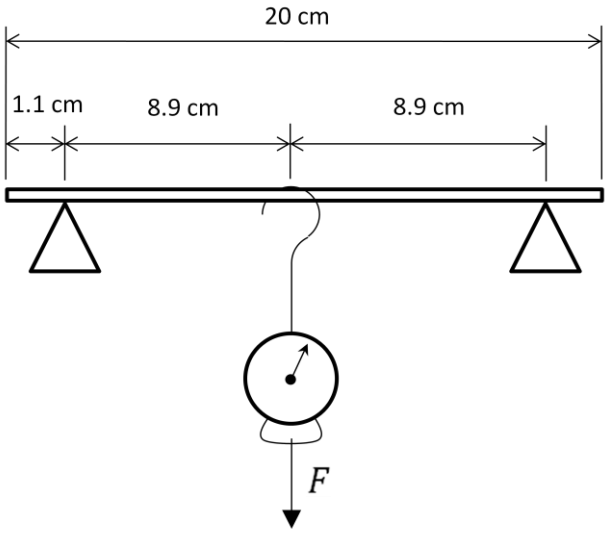

Figure 4.4: Setup for three-point bending tests.

The results of the heat treatments and three-point bending tests are shown in Table 4.1. Results are shown for mass fraction lost and for the ratio of a property value after the indicated treatment to the property value in an unheated state (subscript o). All values given are averages over all samples tested. The properties given are average diameter D_{avg} (the samples are slightly elliptical, so the average diameter is the mean of the maximum and minimum measured diameters), sample length L (no appreciable reduction in length was observed for the 101˚C and 250˚C samples, so their final lengths were not measured), density ρ, and flexural strength σ. All property ratios decrease as

the fraction of mass lost increases except for the strength of dried wood, which is actually stronger than the unheated wood, a result which was also observed by [61].

Table 4.1: Ratio of property value to initial value as a function of fraction of mass lost, along with slope of strength vs. density lines.

Treatment	Mass Fraction Lost	$\frac{D_{avg}}{D_{o,avg}}$	$\frac{L}{L_o}$	$\frac{V}{V_o}$	$\frac{\rho}{\rho_o}$	$\frac{\sigma}{\sigma_o}$	$\partial\sigma_{cr}/\partial\rho_s$ (kPa-m^3/kg)
14 ˚C	0.00	1.00	1.00	1.00	1.00	1.00	342
101˚C, 1 hr	0.061	0.99	1.00	0.97	0.97	1.21	372
250˚C, 1 hr	0.32	0.92	1.00	0.85	0.81	0.52	236
500˚C, 1.5 hr	0.78	0.67	0.86	0.39	0.57	0.091	25.2

It is also interesting to compare density and strength directly, as shown in Figure 4.5. Also shown is a data point from the literature [62] for unheated yellow poplar tested at 12% moisture content. Despite the experimental scatter, Figure 4.5 indicates a correlation between density and flexural strength. This correlation may be due partly to propagation of experimental uncertainty, but the trend appears to exist nonetheless. There is also a significant influence of heating history on density and strength, because the rods gain strength when dried and then lose strength when pyrolyzed. The correlation between density and flexural strength is strongly linear, and the slopes of the linear fits to the four groups of experimental data points (solid lines in Figure 4.5) are reported in Table 4.1.

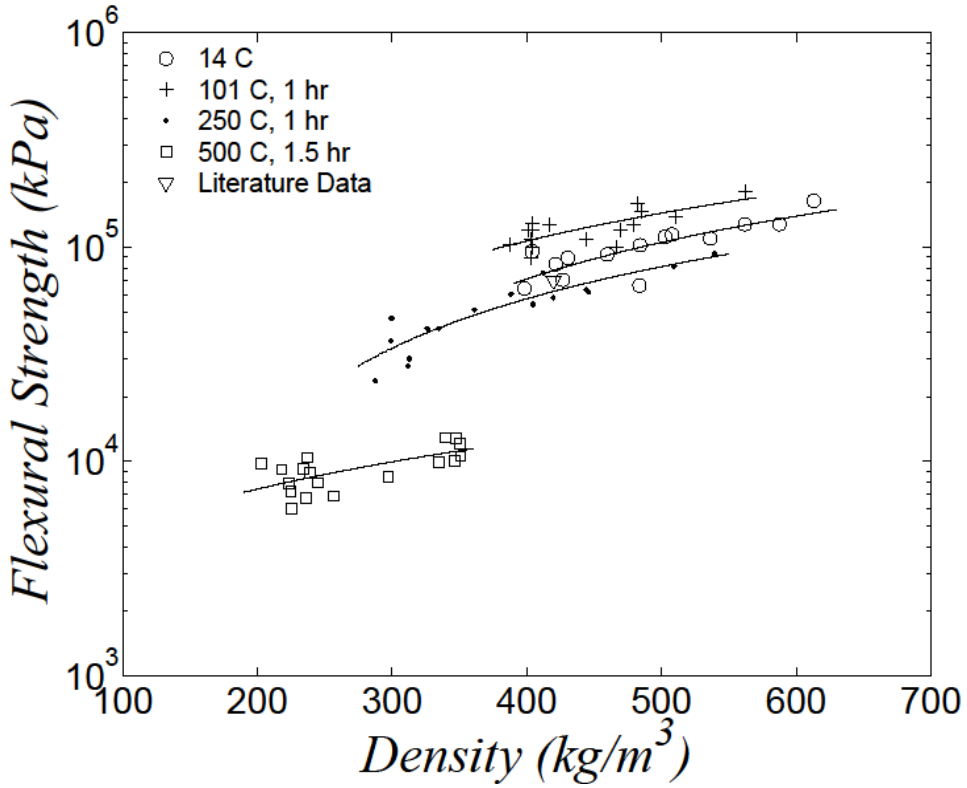

Figure 4.5: Strength and density data for three-point bending tests.

The four heat treatments tested represent the four most important points in the pyrolysis process for wood. For any other point in the pyrolysis process, linear interpolation can be performed using the data in Table 4.1 to obtain a reasonable estimate for properties of interest. This linear interpolation is shown in Figure 4.6. With Figure 4.6, it is now possible to determine values for diameter, length, volume, density, and strength based on the fraction of mass lost, and since the fraction of mass lost is available from the kinetic pyrolysis model, it is possible to determine the geometry, density, and strength of a sample if the pyrolysis time and temperature are given. This information is important for determining whether or not fracture of branches will occur from pyrolysis alone. If pyrolysis does not sufficiently weaken a branch, then this information becomes input for oxidation modeling, which is discussed next.

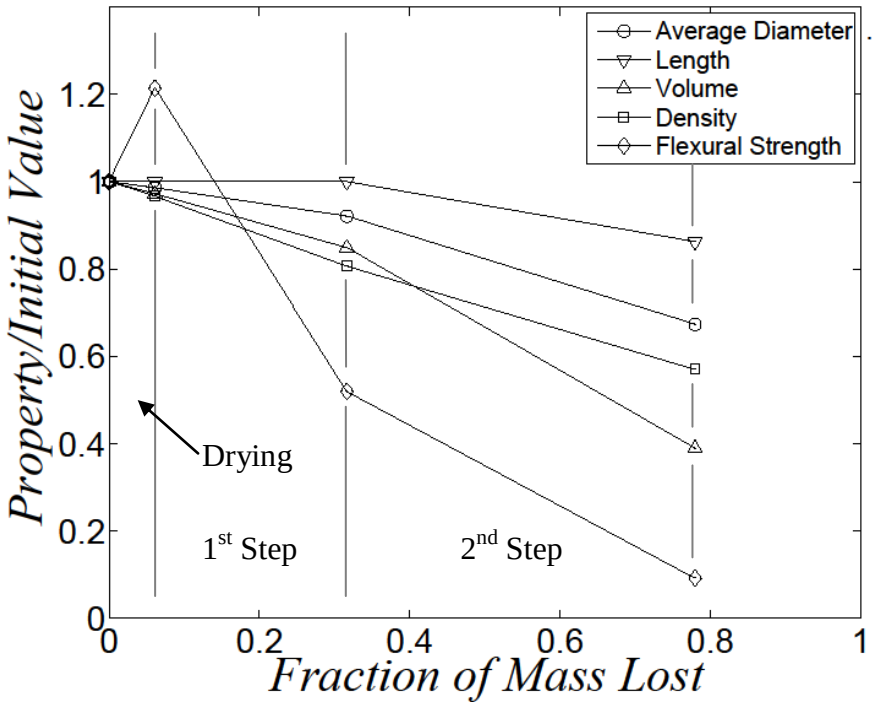

Figure 4.6: Linear interpolation of experimental data for properties in pyrolysis.

It is important to recall that the results of Figure 4.6 are strictly valid for yellow poplar only; a similar analysis is required for different species of trees. It is also important to recall that these results apply to samples without internal variations in temperature. For real wildfire scenarios, the pyrolysis process and calculation of resulting property values are much more complicated, but the preceding analysis is still valuable as a first-order estimation of these values.

4.2.1.2 Oxidation Modeling

If pyrolysis is insufficient for causing fracture of branch fibers, then the time varying loss of mass by oxidation must be modeled. As discussed, the oxidation process is a reaction between the carbonaceous char formed in pyrolysis and oxygen in the gas phase to produce gaseous carbon dioxide and carbon monoxide. Thus, mass is lost from the surface only, with the interior of the branch essentially unchanged.

For a cylindrical branch element undergoing surface oxidation which reduces the diameter while still attached to the tree, the rate of change of mass is equal to the rate of mass loss from the surface, or

$$\frac{dm}{dt} = -\dot{m}_s'' A_s \tag{4.8}$$

where $\dot{m}_s''$ is the mass loss rate per unit surface area and A_s is the surface area of the branch. In terms of the branch diameter, this is

$$\frac{1}{2}\rho_s \frac{dD}{dt} = -\dot{m}_s'' \tag{4.9}$$

Using the B number model, Equation 2.46, to model the mass loss rate, we have

$$\frac{1}{2}\rho_s \frac{dD}{dt} = -h_m ln(1+B) \tag{4.10}$$

Assuming that the Lewis number is equal to 1, so that $h_m = h/c_{p,a}$, where $c_{p,a}$ is the specific heat of air at constant pressure, and using the definition of the average Nusselt number to define h, we have

$$\frac{dD}{dt} = -2\frac{\overline{Nu_D}(k_a/D)}{\rho_s c_{p,a}} ln(1+B) \tag{4.11}$$

where k_a is the thermal conductivity of air. This simplifies to

$$\frac{dD}{dt} = -2\alpha_a \frac{\rho_a}{\rho_s}\frac{ln(1+B)}{D}\overline{Nu_D} \tag{4.12}$$

where α_a is the thermal diffusivity of air. Using Hilpert's [63] correlation for the Nusselt number,

$$\overline{Nu_D} = C\ {Re_D}^m Pr^{1/3} \tag{4.13}$$

where C and m are functions of the Reynolds number, Equation 4.12 simplifies to

$$\frac{dD}{dt} = -2C\alpha_a \frac{\rho_a}{\rho_s} ln(1+B)\left(\frac{U}{\nu_a}\right)^m Pr^{1/3} D^{m-1} \tag{4.14}$$

where U is the velocity of the plume flow and ν_a is the kinematic viscosity of air. Equation 4.14 is valid for any branch in which the velocity of the external flow changes with time. While the branch is oxidizing on the tree, we assume that the flow velocity is constant and integrate over the oxidation time t_{ox} from the initial diameter D_o to any later diameter D_{ox}, obtaining

$$D_{ox}{}^{2-m} - D_o{}^{2-m} = \left[-2(2-m)C\alpha_a \frac{\rho_a}{\rho_s} ln(1+B)\left(\frac{U}{\nu_a}\right)^m Pr^{1/3}\right] t_{ox} \qquad 4.15$$

The diameter ratio during oxidation on the tree, D_{ox}/D_o, is then expressed as a function of time as

$$\frac{D_{ox}}{D_o} = \left[1 - 2(2-m)\frac{\rho_a}{\rho_s} ln(1+B)\overline{Nu_{D_o}}\left(\frac{t_{ox}}{D_o{}^2/\alpha_a}\right)\right]^{\frac{1}{2-m}} \qquad 4.16$$

This is the diameter reduction possible for a given initial diameter, environment, and oxidation time. What must now be determined is whether or not this weakened state is sufficient to allow fracture by aerodynamic drag.

4.2.2 Aerodynamic Loading and Fracture

While degrading on the parent plant, any given branch i is subjected to a variety of loads, as shown in Figure 4.7a. As time passes, the shape and strength of a branch change through pyrolysis and oxidation until the point at which the critical flexural stress is reached by the loading, and the branch fractures at its attachment point and is carried into the plume. Each branch is subjected to the force of its own weight $F_{w,i}$ and a drag force $F_{d,i}$ exerted in the direction of the plume flow. It is assumed that the flow velocity is always opposite to the direction of the gravitational force, in accordance with the buoyant plume model. Additionally, each branch is subjected to bending moments and shear forces from the smaller branches $i+1$ in the subsequent stage of branching. It will be shown that these smaller branches are removed earlier than branch i, so that at the time of fracture branch i is subjected only to the force of its own weight and the drag force. The freebody diagram for a single branch, neglecting the contributions from the higher stages of branching, is shown in Figure 4.7b.

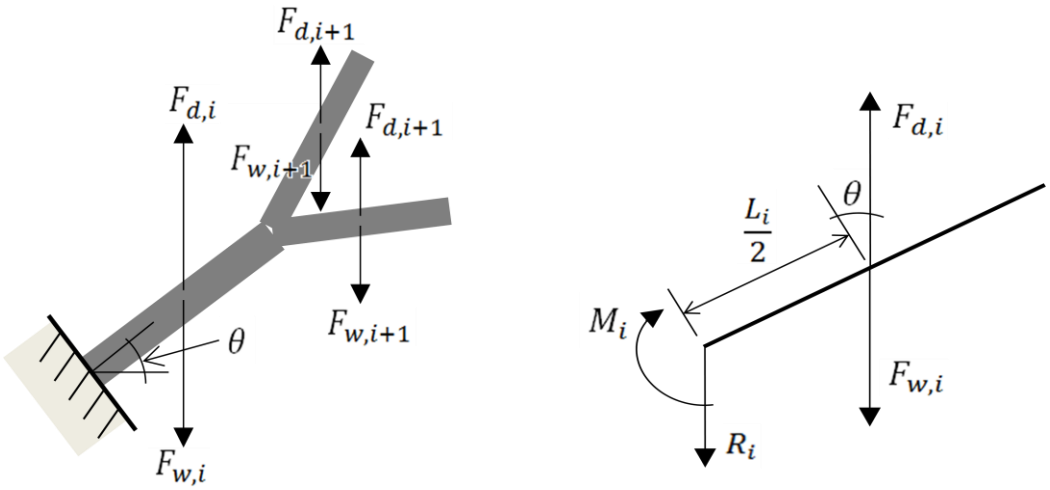

(a) (b)

Figure 4.7: Overall force distribution on branch i (a), and simplified freebody diagram (b) neglecting loading from branches in higher stages.

The bending moment at the base of branch i is

$$M_i = F_{d,i}\frac{L_i}{2}cos\theta_i - F_{w,i}\frac{L_i}{2}cos\theta_i \tag{4.17}$$

where θ is the angle of orientation between the branch and the direction perpendicular to the plume flow. Formulating the drag force in terms of the drag coefficient C_d and defining the weight force in terms of the branch density, we obtain

$$M_i = \frac{L_i}{2}cos\theta_i\left[\frac{1}{2}\rho_a U^2 C_d D_i L_i - \rho_s\frac{\pi}{4}{D_i}^2 L_i g\right] \tag{4.18}$$

The maximum flexural stress, σ, in the cylindrical branch subjected to M_i is

$$\sigma = \frac{32M_i}{\pi {D_i}^3} \tag{4.19}$$

Combining this with Equation 4.18 and dropping the subscript i gives

$$\sigma = \frac{8L^2 cos\theta}{\pi D^2}\left[\rho_a U^2 C_d - \frac{\pi}{2}\rho_s D g\right] \tag{4.20}$$

Using the aspect ratio $A = L/D_o$ and rearranging gives a polynomial for D/D_o:

$$\frac{\pi\sigma}{8A^2 cos\theta}\left(\frac{D}{D_o}\right)^2 + \frac{\pi}{2}\rho_s g D_o\left(\frac{D}{D_o}\right) - \rho_a U^2 C_d = 0 \tag{4.21}$$

If the critical flexural stress for the material is σ_{cr}, then the critical diameter for fracture, D_{cr}, at which the critical stress is achieved can be determined from

$$\frac{\pi\sigma_{cr}}{8A^2cos\theta}\left(\frac{D_{cr}}{D_o}\right)^2 + \frac{\pi}{2}\rho_s g D_o\left(\frac{D_{cr}}{D_o}\right) - \rho_a U^2 C_d = 0 \qquad 4.22$$

This equation can be rearranged to obtain

$$\left(\frac{D_{cr}}{D_o}\right)^2 + 2\left(\frac{2\rho_s g D_o A^2 cos\theta}{\sigma_{cr}}\right)\left(\frac{D_{cr}}{D_o}\right) - \left(\frac{\frac{8}{\pi}\rho_a U^2 C_d A^2 cos\theta}{\sigma_{cr}}\right) = 0 \qquad 4.23$$

We now define $\sigma_w = 2\rho_s g D_o A^2 cos\theta$ as the characteristic stress associated with weight and $\sigma_d = \frac{8}{\pi}\rho_a U^2 C_d A^2 cos\theta$ as the characteristic stress associated with drag, and the failure criterion can be expressed in simple nondimensional form as

$$\left(\frac{D_{cr}}{D_o}\right)^2 + 2\left(\frac{\sigma_w}{\sigma_{cr}}\right)\left(\frac{D_{cr}}{D_o}\right) - \left(\frac{\sigma_d}{\sigma_{cr}}\right) = 0 \qquad 4.24$$

The physically relevant root of this polynomial is

$$\frac{D_{cr}}{D_o} = \sqrt{\left(\frac{\sigma_w}{\sigma_{cr}}\right)^2 + \left(\frac{\sigma_d}{\sigma_{cr}}\right)} - \left(\frac{\sigma_w}{\sigma_{cr}}\right) \qquad 4.25$$

We are very interested in how the initial diameter of a branch affects the breakage process. It should be observed that D_o is contained only within σ_w/σ_{cr}, not within σ_d/σ_{cr}. For situations in which $\sigma_w \ll \sigma_{cr}$ or $\sigma_d/\sigma_{cr} \gg \sigma_w/\sigma_{cr}$, the dependence on initial diameter becomes negligible and we obtain the simple result

$$\frac{D_{cr}}{D_o} = \left(\frac{\sigma_d}{\sigma_{cr}}\right)^{1/2} \qquad 4.26$$

The expression for the time evolution of the oxidizing branch (Equation 4.16) can be nondimensionalized using σ_w to replace D_o in the right side of the equation. We choose values of $C = 0.683$ and $m = 0.5$ for the Hilpert correlation (valid for $40 < Re_D < 4000$) and obtain

$$\frac{D_{ox}}{D_o} = \left[1 - \frac{t_{ox}}{\tau}\left(\frac{\sigma_w}{\sigma_{cr}}\right)^{-3/2}\right]^{2/3} \qquad 4.27$$

which is valid whenever the diameter is greater than the critical diameter; the time constant τ is

$$\tau = \left[3C \frac{\rho_a}{\rho_s} ln(1+B) \left(\frac{U}{\nu}\right)^{1/2} Pr^{1/3} \alpha_a \left(\frac{2\rho_s g A^2 cos\theta}{\sigma_{cr}} \right)^{3/2} \right]^{-1} \qquad 4.28$$

We may use Equations 4.25 and 4.27 to determine when a breakage event occurs. For pyrolysis, Equation 4.27 is not used because mass is not lost from the surface. Instead, the kinetic pyrolysis model along with Figure 4.6 are used to determine the evolution of D, ρ_s, and σ_{cr} as pyrolysis proceeds (we have assumed that the change in length is negligible in this analysis). At each point in time, D_{cr} calculated using Equation 4.25 with the changing values of ρ_s and σ_{cr} is compared to the actual diameter D produced by pyrolysis. If the actual diameter ever becomes equal to the critical diameter, then the branch fractures due to pyrolysis only and is taken into the plume. If the actual diameter remains above the critical diameter during the entire pyrolysis process, then the branch remains attached and begins to undergo thermal degradation due to oxidation.

For the oxidation process, values for D_o, ρ_s, and σ_{cr} are fixed as those at the end of the pyrolysis process, and both Equations 4.25 and 4.27 are used. A breakage event is determined by the intersection of Equations 4.25 and 4.27. If D_{ox}/D_o is greater than D_{cr}/D_o, then the branch remains on the tree, but when t_{ox}/τ increases to the point that $D_{ox}/D_o = D_{cr}/D_o$, the branch fractures.

Figure 4.8 shows in nondimensional terms the behavior of the oxidation process by plotting D_{ox}/D_o and D_{cr}/D_o versus σ_w/σ_{cr} for different values of t_{ox}/τ and σ_d/σ_{cr} respectively. As previously noted, when σ_w/σ_{cr} is small, the weight of the branch is negligible and does not influence the state of stress; the value for D_{cr}/D_o becomes independent of σ_w/σ_{cr} and approaches the value given by Equation 4.26. At the other extreme, when σ_w/σ_{cr} approaches unity, the branch is so heavy that it is nearly about to fracture from the gravitational load alone. However, the analysis assumes that fracture occurs when a drag-induced moment that is opposite in direction to the weight-induced moment exceeds the weight-induced moment enough to subject the branch to the critical stress. As such, the branch must be oxidized to a smaller diameter ratio D_{cr}/D_o for

upward fracture to occur. As t_{ox}/τ increases (oxidation time increases for a given τ), the maximum initial diameter for which fracture occurs increases. It is important to note that the maximum value of σ_w/σ_{cr} for which fracture occurs increases monotonically with oxidation time for a given σ_d/σ_{cr} and τ, so small branches are always lost before large branches. This clarifies why it is reasonable to neglect the moments due to the branches in level $i+1$ in the moment balance on branch i.

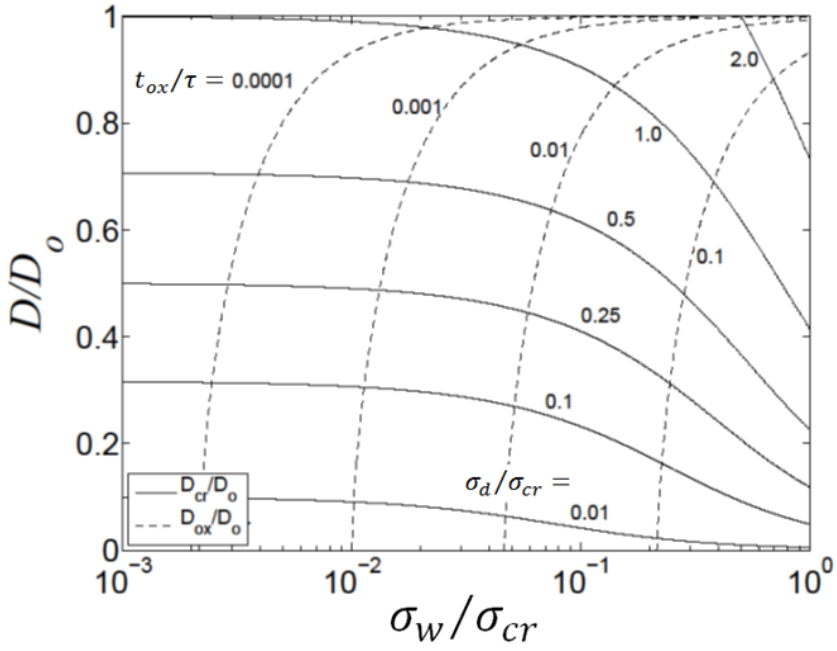

Figure 4.8: D_{cr}/D_o and D_{ox}/D_o versus σ_w/σ_{cr} for different values of σ_d/σ_{cr} and t_{ox}/τ.

The time available for pyrolysis and oxidation of a specific branch (t_{ox}) is dependent upon the thickness and rate of spread of the wildland fire flame front. Thus, t_{ox} is highly variable spatially and with the progression of the fire. Nonetheless, since small branches oxidize faster and are broken off more frequently than large branches, we expect more small branches to be lost than large branches in wildland fire scenarios. This agrees with observation.

This concludes the development of the brand generation model. For a given initial branch geometry and environmental scenario, the kinetic pyrolysis model and

Equations 4.25 and 4.27 may be used to determine whether or not a branch will be lofted and what its dimensions and density are at the time of lofting. What remains in providing a complete picture of brand lofting in wildfire scenarios is to use this information as a starting point for the lofting and propagation phases of ember spread. Adding modeling for these phases produces a suitable model for analyzing the ember lofting risks of different fuels in different wildfire scenarios.

4.3 BRAND LOFTING AND PROPAGATION MODEL

Once the brand is removed from the tree, it travels upwards through the plume, is ejected, and drifts back to earth. The following model for brand transport was developed by Woycheese et al. [48-49].

While traveling through the plume and drifting to earth, the brand is subjected to its weight force, which acts downwards,

$$\boldsymbol{F}_w = -mg\hat{\boldsymbol{k}} \tag{4.29}$$

and to a drag force, which acts in the direction of the relative velocity $\boldsymbol{W}$ of the flow to the brand,

$$\boldsymbol{F}_d = \frac{1}{2}\rho_a DLC_d|\boldsymbol{W}|^2\frac{\boldsymbol{W}}{|\boldsymbol{W}|} \tag{4.30}$$

Here it is assumed that the axis of the cylindrical brand is always perpendicular to the direction of $\boldsymbol{W}$. Conservation of brand momentum is therefore given by

$$\frac{d}{dt}(m\boldsymbol{V}) = \boldsymbol{F}_d + \boldsymbol{F}_w \tag{4.31}$$

where $\boldsymbol{V}$ is the absolute velocity of the brand.

Equation 4.31 can be broken into velocity components V_x and V_z (where the z direction is opposite to the gravitational force and the x direction is perpendicular to it) and simplified, giving

$$\frac{dV_x}{dt} = \frac{2}{\pi}\left(\frac{\rho_a}{\rho_s}\right)\frac{C_d}{D}|\boldsymbol{W}|W_x - \frac{2V_x}{D}\frac{dD}{dt} \tag{4.32a}$$

$$\frac{dV_z}{dt} = \frac{2}{\pi}\left(\frac{\rho_a}{\rho_s}\right)\frac{C_d}{D}|\boldsymbol{W}|W_z - \frac{2V_z}{D}\frac{dD}{dt} - g \tag{4.32b}$$

The rate of change of the diameter dD/dt is given by Equation 4.14, which is unchanged from the equation used for diameter change during pyrolysis on the tree, except that the velocity used is the relative velocity magnitude $|\boldsymbol{W}|$:

$$\frac{dD}{dt} = -2C\alpha_a \frac{\rho_a}{\rho_s} ln(1+B) \left(\frac{|\boldsymbol{W}|}{\nu_a}\right)^m Pr^{1/3} D^{m-1} \quad 4.33$$

The trajectory of the brands is determined by the definition of velocity:

$$\frac{dx}{dt} = V_x \quad 4.34a$$

$$\frac{dz}{dt} = V_z \quad 4.34b$$

Equations 4.32, 4.33, and 4.34 describe the evolution of the brand during lofting in the plume and during the descent. During the plume lofting, Equations 4.32a and 4.34a are unused, because the brand is assumed to ascend vertically. The relative velocity within the plume is $W_z = U_{plume} - V_z$, where U_{plume} is the absolute velocity of the air at the centerline of the plume. The plume velocity is determined using the McCaffrey plume model [64], which defines the centerline velocity as

$$U_{plume} = \kappa \left(\frac{z}{\dot{Q}^{2/5}}\right)^{\eta} \dot{Q}^{1/5} \quad 4.35$$

where $\dot{Q}$ is the heat release rate of the fire. The parameters κ and η are different for each of the three regions of the plume, with the transition between regions defined by a scaled height $z/\dot{Q}^{2/5}$ [m/kW$^{2/5}$]. For the continuous flame region $\left(z/\dot{Q}^{2/5} < 0.08\right)$, $\kappa = 6.8$ m$^{1/2}$/s and $\eta = 1/2$, for the intermittent flame region $\left(0.08 < z/\dot{Q}^{2/5} < 0.2\right)$, $\kappa = 1.9$ m/(kW$^{1/5}$s) and $\eta = 0$, and for the plume region $\left(z/\dot{Q}^{2/5} > 0.2\right)$, $\kappa = 1.1$ m$^{4/3}$/(kW$^{1/3}$s) and $\eta = -1/3$.

After the brand exits the plume, both the x and z components of Equations 4.32 and 4.34 are used. The relative velocity in the x direction is $W_x = U_{wind} - V_x$, where U_{wind} is the absolute velocity of the prevailing ambient wind, which is assumed to be spatially uniform and completely horizontal, and the relative velocity in the z direction is $W_z = -V_z$.

During the lofting process, the brand's diameter continues to decrease, and the length may change as it fragments into smaller pieces. The fragmentation process increases the mass loss rate of the brands because the longitudinal mass loss rate becomes non-negligible when the aspect ratio of the fragmenting brands becomes sufficiently small. Fragmentation effects have not been included in the present analysis because this work primarily focuses on the brand generation process.

4.4 CASE STUDY: EMBER GENERATION AND PROPAGATION IN A WILDLAND FIRE

The foregoing theory is used to construct a Monte Carlo simulation for brand generation and transport in a wildland fire. The mass evolution and transport of a single brand is modeled as follows. A branch of a prescribed material with prescribed initial geometry, density, and flexural strength is pyrolyzed and oxidized in a fire with heat release rate $\dot{Q}$. It is assumed that the wildfire propagates steadily as a front, so that the branch is pyrolyzing and oxidizing within the front for prescribed times t_{pyr} and t_{ox}. If at any point during pyrolysis or oxidation the diameter of the branch reaches D_{cr} (as defined by Equation 4.25), it fractures and is taken into the plume; if it does not reach D_{cr} during the prescribed times, it remains on the tree.

The lofted brands are taken into the plume and are assumed to begin their travel at the very top of the intermittent flame region. The oxidizing brands are carried upwards and ejected after some prescribed time t_{plume}. They then drift to the ground through a horizontal wind of prescribed velocity U_{wind}. If a brand returns to the ground with a diameter greater than zero, it is assumed to be of interest as a pilot to a potential spot fire.

As discussed, the pyrolysis process is extremely complex, and due to the large characteristic time for conduction within the wood, the extent of damage in any particular branch will vary as a function of radial location. It is therefore difficult to model the time varying pyrolysis process with confidence and compare the results with Equation 4.25, as described in section 4.2.2. In the absence of more advanced modeling, we will lump the pyrolysis process into an instantaneous event and determine a single value for post-pyrolysis density and strength, and we will assume negligible change in shape, so that the

initial diameter and length are preserved throughout pyrolysis. This single state will be used with Equation 4.25 to determine whether or not fracture can occur from pyrolysis alone.

It is assumed that the wildfire propagates over a field of yellow poplar trees which have the same nominal trunk diameter D_1 and the same number of branching stages I. We then wish to determine the size of embers lofted and the size of embers deposited for the branching network with initial branch diameters $D_1, D_2, \ldots, D_I$. It is anticipated that variations in the physical parameters defining this model might affect the predictions. In particular, the branch angle of orientation θ, the plume travel time t_{plume}, and the post-pyrolysis density and strength are assumed to be random. To handle these uncertainties, probability density functions are assigned to these variables and a 5000-case Monte Carlo simulation is performed for each nominal branch diameter. In the absence of detailed information about the angle of orientation for the branches, a uniform distribution is assumed between $\theta = 0$ and $\theta = \pi/2$. For flexural strength and density, a value is assumed for a sample which has completely pyrolyzed hemicellulose and lignin and partially pyrolyzed cellulose. Based on unheated values of 420 kg/m^3 and 70,000 kPa for density and strength [62], post-pyrolysis values of 290 kg/m^3 and 20,000 kPa are selected. The density is given a normal distribution with a standard deviation of 15%, and strength is assumed to be proportional to density, as indicated by the linear trend of the experimental data.

For t_{plume}, it is assumed that the brand will be ejected at approximately the height where the plume velocity and the prevailing wind velocity are equal, because above this point the dominant drag force is caused by the prevailing wind. The brands which take the longest time to reach this height are the large brands, because their terminal velocity is highest and thus their upward travel velocity is lowest. The smallest brands reach this height almost instantaneously, so the bounds on t_{plume} are then zero and the travel time of the largest loftable brand. The largest possible loftable brand diameter is determined by the intersection of Equations 4.27 and 4.25, with $t = t_{ox}$ and $\theta = 0$, and the time it takes for this brand to reach the ejection point is determined from Equations 4.32b, 4.33,

4.34b, and 4.35. With the bounds set, a distribution may then be applied to t_{plume}, and for this case study, a uniform distribution is assigned between zero and the upper bound.

The trees in the case study are assumed to be yellow poplar. The nominal trunk diameter is taken to be 8 cm, and ten branching stages are assumed, so that the nominal diameter of the smallest stage is 3.5 mm. The aspect ratio of the branches is specified to be 50 based upon measurements of tree limbs collected and analyzed for this work. Woycheese et al. report a value of 1.2 for the B number for wood burning in air, which is used here. The wildfire is assumed to have a heat release rate of 50 MW and a prevailing horizontal wind velocity of 10 m/sec. The ground oxidation time t_{ox} is assumed to be 100 sec, which is consistent with values reported in the literature [65]. The upper bound on the plume travel time is determined to be approximately 10 sec.

The results of the Monte Carlo simulations are shown in Figure 4.9 and Figure 4.10. The average diameter ratios of brands lofted (D_{lofted}/D_o, equivalently D_{cr}/D_o) and deposited ($D_{deposited}/D_o$) are shown in Figure 4.9, along with the analytical prediction for D_{cr}/D_o, which is obtained by setting θ to zero and using the nominal values for density and flexural strength in Equations 4.25 and 4.27. For a nominal oxidation time of 100 sec, the analytical maximum loftable initial diameter, D_{max}, is 4.7 cm. For initial diameters above D_{max}, no analytical value for D_{cr}/D_o can be reported, because no brands are lofted or deposited.

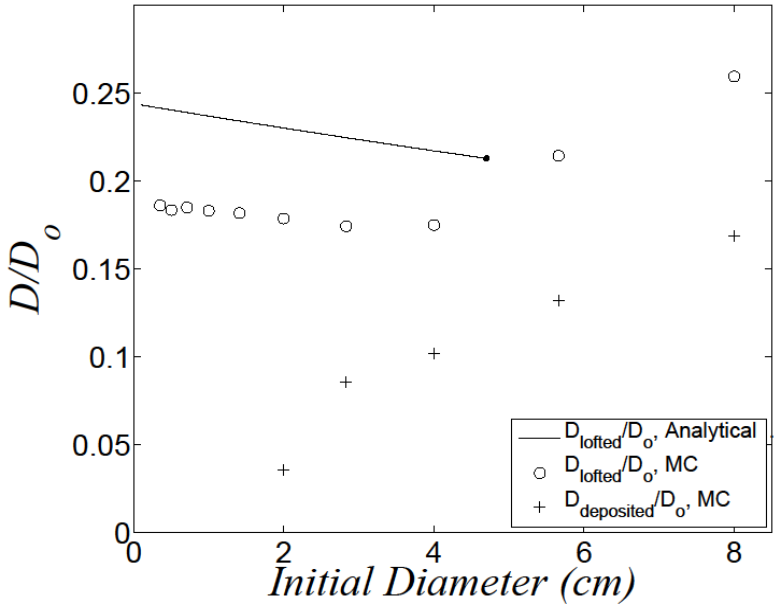

Figure 4.9: Diameter ratios D_{lofted}/D_o and $D_{deposited}/D_o$ for Monte Carlo simulations, along with analytical prediction.

The lofted brand diameter ratio, D_{lofted}/D_o, for the Monte Carlo simulations is lower than that predicted analytically for all initial diameters below D_{max}. This is because the angle of orientation θ is always greater than or equal to zero, which decreases the effective moment arm of the branch and requires more mass to be lost before fracture can occur. For initial diameters greater than D_{max}, only a small number of brands which have very low density and strength are lost, and these break with a larger diameter ratio than the analytical prediction, which is based on the nominal value for strength.

The deposited brand diameter ratio, $D_{deposited}/D_o$, for the Monte Carlo simulations is zero for the smallest branches and increases with initial diameter monotonically. This indicates that small brands, while easily lofted, are too small to survive the lofting and propagation phases, oxidizing completely in the air, while larger brands are able to survive lofting and propagation and land with appreciable mass.

Further insight is gained from Figure 4.10, which shows the fraction by number, N/N_o (N_o is the original 5000 samples), of brands lofted and deposited versus initial diameter. For the initial diameters tested, all brands of initial diameter less than D_{max} are lofted (except those with unusually high strength), but only brands of initial diameters around 4.0 cm are deposited in appreciable numbers. Brands with very small initial diameter are easily lofted but cannot survive propagation, while brands with large initial diameters can easily survive propagation but are only very rarely lofted. The results of Figure 4.9 and Figure 4.10 show that there is an optimal initial diameter for brand propagation which is small enough to be lofted frequently but large enough to survive the propagation process.

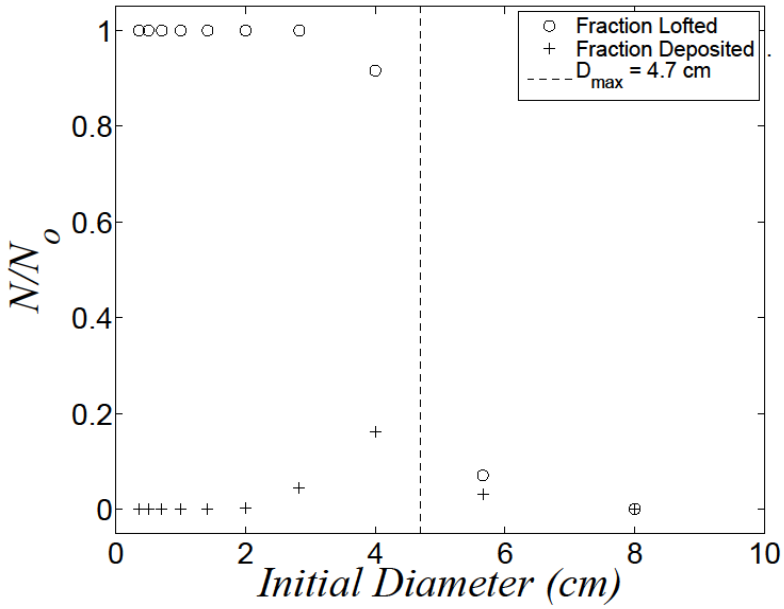

Figure 4.10: Fraction by number of brands lofted and deposited.

The average propagation distance for brands which survive the lofting and deposition process is approximately 75 m. One notes that even for this relatively small fire (50 MW) brands are lofted and deposited over distances that might compromise structures in an urban wildland interface scenario.

The brands produced in the case study were compared with the observations of Manzello et al. [54] and Manzello et al. [57], who performed experiments on Douglas fir and collected brands with diameters on the order of 1 cm or less. The aspect ratio of the brands collected is much smaller than that used in the present study, indicating that the flexural strength of experimentally collected brands is lower than that used in the model. This discrepancy is most likely due to the difficulty of determining post pyrolysis properties of real branches based on those found experimentally. The experimentally determined values for flexural strength are found from carefully prepared specimens with uniform cross sectional area and a minimal number of defects, while branches in wildland fire scenarios have large variability in cross-sectional area, may contain numerous defects, and are wrapped in bark, whose strength properties are unknown. The dowel rods tested are also probably taken from stronger, older regions of the tree (heartwood) to provide them with additional strength, while the wood in the branch tips is younger, softer, and has lower strength (sapwood). Additionally, as already discussed, the heating history and post pyrolysis state of branches in a wildfire is much different from that observed experimentally. A further investigation of the strength properties of pyrolyzed wildland fuels will be necessary to determine the appropriate values of flexural strength to use in predictive models.

It is also worth noting that the brands collected by Manzello et al. do not contain smaller elements from subsequent stages of branching. This indicates that smaller branches are indeed lost before large branches, confirming both the assumption used in determining the moment balance (Equation 4.17) and the results of Figure 4.8.

4.5 CONCLUSIONS

A model for brand breakage for a tree with self similar branching features has been developed. The fractal nature of the tree makes it possible to predict the sequence in which branches of varying diameters are lost from the tree, simplifying the moment and strength analysis for individual branches. For any individual branch, the breakage model relies on aerodynamic and weight loading of branch fibers that are being consumed by pyrolysis and oxidation. For both processes, when the time-increasing

stress at the branch junction equals the flexural strength for the specimen, breakage occurs. For the oxidation process, the breakage model can be framed in terms of a drag-induced stress to strength ratio and weight-induced stress to strength ratio. A limiting case is identified when the weight-induced stress to strength value is small, and one can show that a critical diameter ratio for failure is dependent only upon the drag-induced stress to strength ratio.

An experimental investigation was also performed to understand the effect of pyrolysis on the geometry, density, and flexural strength of wood. The experiments showed that with heating at oven conditions, there was minimal change in sample volume and shape when cellulose did not degrade, and there was a significant change in volume and shape when cellulose did degrade. For experimental conditions in which the wood samples were only dried, there was an increase in the flexural strength, but with subsequent heating and pyrolysis, the strength markedly decreased. The slope of the strength to final density values of the wood samples was roughly constant for a particular heating scenario. The experiments were useful in defining a reduced strength initial condition for the subsequent oxidation processes.

The breakage model was coupled to a plume and transport model taken from Woycheese et al., and a Monte Carlo wildland fire case study was performed. For wildland fires with branching fuel sources, there is an optimal branch diameter which propagates the most mass to the ground ahead of the fire front. This occurs for branches which are small enough to be removed from the tree within the time allowed by the traveling flame front but large enough to survive the transport process.

The post-pyrolysis strength properties of wildland fuels have not been investigated experimentally to a significant degree. The author hopes that the present work will encourage additional work in this area as a necessary component in the development of reliable models for predicting ember generation and propagation in wildfire scenarios.

Chapter 5: Conclusions

In this work, the coupled nature of thermochemical and mechanical degradation is explored. It is found that mechanical loss of mass is frequently tied to a weakened state in the system which is a result of thermochemical erosion. The thermochemical erosion mechanism is also explored, and it is found that its behavior is dependent upon the balance achieved between competing processes of transport and chemistry.

The thermochemical degradation mechanism is explored by constructing a quasi-steady-state ablation model with finite rate surface chemistry. This model is adjusted for a simple ablation scenario, the oxidation of solid carbon in air. This simplification allows observation of the fundamental balance between chemistry and transport which exists in this system, and it facilitates the validation of the model with experimental data. The model is validated through comparison with the experiments of Matsui et al. [17] and is shown to be a good predictor of the qualitative behavior of this system. The B number and Damkohler number are identified as the appropriate nondimensional groups for systems with mass loss from a solid phase and with competing chemical and transport effects, respectively, and collapse of experimental data is obtained using these groups. Manipulation of the laws of mass and energy conservation reveals an extremely useful formulation of the Damkohler number, $\overline{Da}$. Using this formulation, a simple algebraic relationship is found between B and $\overline{Da}$ which describes the combustion of solid carbon very well in the regime where chemical equilibrium is not valid.

With greater understanding regarding the thermochemical erosion mechanism, the mechanical erosion mechanism is then explored. A model is developed for a porous carbon preform (like those used to make PICA), and it is seen that for porous materials oxidation occurs over a finite depth rather than in an infinitesimal layer at the surface of the material. Conservation equations for the gas and solid phases within the porous solid are developed, and a nondimensional recession velocity, v_s^*, is derived, which is dependent upon the geometry of the porous medium, the boundary conditions, and the blowing velocity of pyrolysis gases out of the wall. The mechanical removal of thermochemically eroded particles from the surface of the solid is then considered, and it

is found that this phenomenon is consistent with the physics of the v_s^* model and can be incorporated into it. A useful approximate relation is developed for v_s^*, and this model is incorporated into the existing thermochemical ablation model, which is then capable of addressing both thermochemical and surface mechanical erosion for PICA. This model is applied to a realistic reentry scenario, and it is found that mechanical erosion of small particles from the surface of the ablator produces a negligible contribution to the overall recession rate for PICA. Although other mechanical erosion mechanisms (such as the ejection of large chunks of mass) exist, this exercise confirms the suitability of PICA for reentry applications in which only the surface erosion of individual fibers is important, and other scenarios in which this type of mechanical erosion may be important are discussed.

The thermo-chemo-mechanical erosion mechanism is then explored in the context of brand generation in wildland fires. It is proposed that solid brand particles are removed from a combusting plant when aerodynamic loading from the external flow produces stresses sufficient for fracture within the branches. Furthermore, it is proposed that thermochemical degradation is essential for weakening branches sufficiently that they may be removed by flow effects, so the two processes of chemical and mechanical loss are coupled, as in the ablation scenario. A model for brand generation is developed by considering the thermochemical degradation processes of pyrolysis and oxidation, and experiments are performed to investigate the changes in fuel properties as thermochemical degradation proceeds. The aerodynamic loading of branch fibers is also modeled, and this model is combined with the thermal degradation model to develop a criteria for determining if and when a particular branch size is lofted. The brand generation model is then coupled to a simple plume and propagation model, and the full model is exercised in a case study for a realistic wildfire scenario. The presence of an optimal diameter for lofting is identified, which is small enough that branches are lofted frequently but large enough that they survive the propagation process.

This work makes clear the fact that mechanical loss of mass is in some circumstances intimately tied to thermochemical loss of mass. Because of this, it is very

important to understand how geometry and mechanical properties change with damage to a material. Because the coupled thermo-chemo-mechanical erosion effect has not been investigated extensively, there is little experimental data on the subject. A valuable addition to this work would be experimental characterization of strength properties as a function of the extent of thermochemical damage for the systems investigated, namely carbon fibers and cylindrical wooden branches. Also, since the mechanical erosion mechanism is highly dependent upon the geometry of the material in question, additional valuable future work would be to extend the current models to situations with different geometries, such as ordered fiber layups for reentry applications and trees with leaves for the wildfire scenario.

Appendix A: The Equilibrium Model for Thermochemical Ablation

The following section describes the type of calculations made by an equilibrium ablation code such as the Aerotherm Chemical Equilibrium (ACE) code [4]. The following derivation follows that given in the ACE code, and afterwards the general theory is applied to the graphite oxidation problem of interest in the current work. The product of an equilibrium code such as ACE is a map between the B number and the wall temperature for a given total pressure, which can be used with a system energy balance to determine the appropriate B, T_w pair for a given scenario. We will therefore treat B and P as known quantities and solve a system of equations for a group of unknowns, one of which is T_w.

The ACE code determines the B number for an open system by analyzing the equilibrium state of a group of elements. That is, the reactions considered are between molecular species and their constituent elements rather than between groups of molecular species. We consider a group of $k = 1 \rightarrow K$ elemental species which may combine to form $j = 1 \rightarrow J$ gaseous molecular species and one condensed phase species (l). There are then a total of $K + J = I$ gaseous species and a single condensed species. The formation of each gaseous molecular species (j) from the elements (k) is governed by an equilibrium relation based on the minimization of Gibbs free energy of the form

$$\ln P_j - \sum_{k=1}^{K} \nu_{k\rightarrow j} \ln P_k = \ln\left[K_{p,j}(T_w)\right] \qquad \text{A.1}$$

where P_j and P_k are the partial pressures of the molecular and elemental gas species, $\nu_{k\rightarrow j}$ are the stoichiometric coefficients for each element in the formation reaction (forming one molecule of product), and $K_{p,j}$ is the equilibrium constant for each formation reaction, which is a function of temperature (in this case it is the ablating wall temperature T_w).

An equilibrium relation also exists between the elements (k) and the condensed phase (l) of the form

$$-\sum_{k=1}^{K} \nu_{k\to l} \ln P_k = \ln\left[K_{p,l}(T_w)\right] \qquad \text{A.2}$$

where the stoichiometric coefficients $\nu_{k\to l}$ are now for the formation of one molecule of the condensed phase species from the elemental species.

As was done for finite rate surface chemistry, the equilibrium model is related to a set of species mass balances for the open system. It is convenient in this context to track the mass fraction of elements ($\tilde{Y}_k$) through the solid phase, surface, and gas phase, rather than the mass fractions of molecular species, as was done in the finite rate model. Because the mass of each element is conserved, the conserved quantity $\mathcal{P}$ is simply $\tilde{Y}_k$, and the mass balance for each element k between the freestream and the T state is

$$h_m\left(\tilde{Y}_{k,w} - \tilde{Y}_{k,\infty}\right) + \dot{m}_g''\tilde{Y}_{k,w} = \dot{m}_g''\tilde{Y}_{k,T} \qquad \text{A.3}$$

In this case, we have assumed for simplicity that there is no blowing of pyrolysis gas, so the mass flux at the T state is the same as that out of the surface and is due only to surface reactions (the ACE code has the ability to account for blowing pyrolysis gas if desired). Defining the B number again as $B = \dot{m}_g''/h_m$, we obtain

$$B = \frac{\tilde{Y}_{k,\infty} - \tilde{Y}_{k,w}}{\tilde{Y}_{k,w} - \tilde{Y}_{k,T}} \qquad \text{A.4}$$

This can be rearranged for $\tilde{Y}_{k,w}$:

$$\tilde{Y}_{k,w} = \frac{B\tilde{Y}_{k,T} + \tilde{Y}_{k,\infty}}{1+B} \qquad \text{A.5}$$

Next, the elemental mass fractions at the wall must be related to the partial pressures. This is done by summing the contributions of all the gaseous species (i) to obtain the total amount of mass of each element:

$$\tilde{Y}_{k,w} = \frac{W_k}{W}\sum_{i=1}^{I} \nu_{k\to j}\frac{P_i}{P} \qquad \text{A.6}$$

where W_k and W are the elemental and mixture molar masses, respectively, and P is the total pressure. The mixture molar mass is determined from

$$W = \sum_{i=1}^{I} \frac{P_i}{P} W_i \qquad \text{A.7}$$

Additionally, if desired, Dalton's law may be used to eliminate one of the gaseous equilibrium relations (A.1):

$$P = \sum_{i=1}^{I} P_i \qquad \text{A.8}$$

Neglecting Dalton's law, we have the following unknowns: P_i (I unknowns), $\tilde{Y}_{k,w}$ (K unknowns), W (1 unknown), and T_w (1 unknown). This gives a total of $I + K + 2$ unknowns. We also have the following equations: A.1 (J equations), A.2 (1 equation), A.5 (K equations), A.6 (K equations), and A.7 (1 equation). This gives a total of $I + K + 2$ equations, so the system of closed.

The model just derived will now be applied to the graphite oxidation in air scenario that we have analyzed throughout this work. This reaction is

$$\mathrm{C_{(gr)}} + \frac{1}{2}\mathrm{O_{2(g)}} \rightarrow \mathrm{CO_{(g)}} \qquad \text{A.9}$$

In equilibrium, we expect to have $J = 3$ molecular gas species ($O_{2(g)}$, $N_{2(g)}$, $CO_{(g)}$) and one condensed species ($C_{(gr)}$), which are formed from $I = 3$ elemental gas species ($O_{(g)}$, $N_{(g)}$, $C_{(g)}$). The gas phase equilibrium formation reactions are then

$$\mathrm{2O_{(g)} \rightarrow O_{2(g)}} \qquad \text{A.10a}$$

$$\mathrm{2N_{(g)} \rightarrow N_{2(g)}} \qquad \text{A.10b}$$

$$\mathrm{C_{(g)} + O_{(g)} \rightarrow CO_{(g)}} \qquad \text{A.10c}$$

and the solid phase equilibrium reaction is

$$\mathrm{C_{(g)} \rightarrow C_{(gr)}} \qquad \text{A.11}$$

The gas phase equilibrium relations (A.1) become

$$\ln P_{O_2} - 2\ln P_O = \ln\left[K_{p,O_2}(T_w)\right] \qquad \text{A.12a}$$

$$\ln P_{N_2} - 2\ln P_N = \ln\left[K_{p,N_2}(T_w)\right] \qquad \text{A.12b}$$

$$\ln P_{CO} - \ln P_C - \ln P_O = \ln\left[K_{p,CO}(T_w)\right] \qquad \text{A.12c}$$

and the solid phase equilibrium relation (A.2) is

$$-\ln P_C = \ln\left[K_{p,C_{(gr)}}(T_w)\right] \tag{A.13}$$

With $Y_{O_2,\infty} = 0.232$ and $Y_{N_2,\infty} = 0.768$, the elemental wall mass fractions are related to the B number (A.5) by

$$\tilde{Y}_{O,w} = \frac{0.232}{1+B} \tag{A.14a}$$

$$\tilde{Y}_{N,w} = \frac{0.768}{1+B} \tag{A.14b}$$

$$\tilde{Y}_{C,w} = \frac{B}{1+B} \tag{A.14c}$$

and to the partial pressures (A.6) by

$$\tilde{Y}_{O,w} = \frac{W_O}{W}\left(\frac{P_O}{P} + 2\frac{P_{O_2}}{P} + \frac{P_{CO}}{P}\right) \tag{A.15a}$$

$$\tilde{Y}_{N,w} = \frac{W_N}{W}\left(\frac{P_N}{P} + 2\frac{P_{N_2}}{P}\right) \tag{A.15b}$$

$$\tilde{Y}_{C,w} = \frac{W_C}{W}\left(\frac{P_C}{P} + \frac{P_{CO}}{P}\right) \tag{A.15c}$$

Finally, the mixture molar mass (A.7) is

$$W = \frac{P_O}{P}W_O + \frac{P_N}{P}W_N + \frac{P_C}{P}W_C + \frac{P_{O_2}}{P}W_{O_2} + \frac{P_{N_2}}{P}W_{N_2} + \frac{P_{CO}}{P}W_{CO} \tag{A.16}$$

These 11 equations can be solved for the 11 unknowns (P_O, P_N, P_C, P_{O_2}, P_{N_2}, P_{CO}, $\tilde{Y}_{O,w}$, $\tilde{Y}_{N,w}$, $\tilde{Y}_{C,w}$, W, and T_w), provided that B is given. The dependence of K_p on T_w is usually complicated and requires the use of tables or polynomial fits.

The preceding system of equations was solved using ACE. The ACE solution is capable of including more reactions than the single one just described, so it includes a more complete picture of the system at all temperatures. Before analyzing the open system, however, it is important to understand the behavior of a closed system. A closed system calculation (which relies on equilibrium relations like Equation A.1) was performed using the NASA Chemical Equilibrium with Applications (CEA) code [66]. The gaseous species O_2 and N_2 were added to a system with excess graphite ($C_{(gr)}$), and the system temperature was varied over a wide range. The results are shown in Figure A.1.

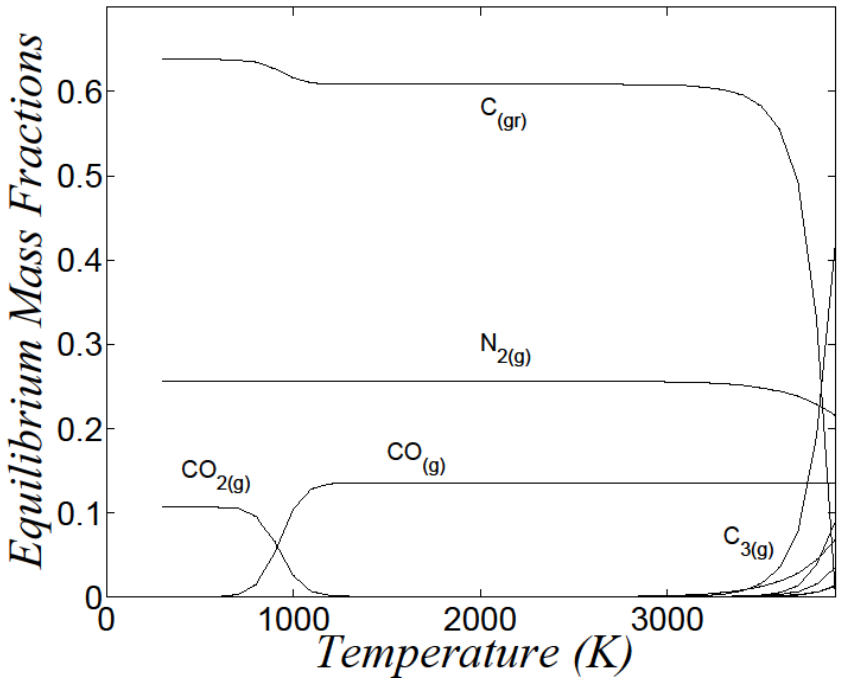

Figure A.1: Closed system equilibrium calculation for air and graphite at varying temperatures.

Clearly, many reactions are possible over the temperature range investigated, and the oxidation reaction A.9 modeled above is only representative of the temperature range between 1500 K and 3000 K, where carbon monoxide is the preferred state over carbon dioxide, nitrogen is non-reactive and sublimation is not occurring yet. Several important behaviors should be noticed in this figure. First, atomic or molecular oxygen is virtually absent from this system in equilibrium; it is completely consumed to create carbon dioxide or carbon monoxide. Second, between approximately 700 K and 1100 K, there is a transition from carbon dioxide to carbon monoxide as the oxidation product. Third, nitrogen is non-reactive throughout most of the temperature range, and it only reacts with carbon to form $CN_{(g)}$ and other products at high temperatures. Lastly, carbon is consumed at all temperatures by oxidation (to $CO_{(g)}$ or $CO_{2(g)}$), but this consumption is limited by the availability of oxygen. At high temperatures, carbon takes part in a host of sublimation reactions to form products such as $C_{(g)}$, $C_{2(g)}$, $C_{3(g)}$, $C_{4(g)}$, and $C_{5(g)}$, which are

not limited by the availability of any other element (only the most dominant product, $C_{3(g)}$, is labeled in Figure A.1; the other concentrations are shown as unlabeled lines). Thus, at high temperatures, the consumption rate of graphite increases tremendously, and all of the excess graphite in the current study is actually consumed into the gas phase by around 3800 K.

We expect to see the preservation of several of these features in the open system equilibrium calculation using ACE. There should be a low temperature region where CO_2 is the dominant product, an intermediate temperature region where CO is the dominant product, and a high temperature region where the mass loss rate increases greatly due to carbon sublimation and nitridation.

The open system equilibrium calculations using ACE are shown in Figure A.2. Two plateaus in the B number are present, which indicate the regions where the single reactions to produce CO or CO_2 are dominant. In terms of the B number, these plateaus can be understood from Equation 2.52:

$$B = \frac{Y_{O_2,\infty} - Y_{O_2,w}}{Y_{O_2,w} + \frac{1}{r}} \qquad 2.52$$

where $r = (\nu_C W_C)/(\nu_{O_2} W_{O_2})$. For the reaction to form CO, $\nu_{O_2} = 1/2$, and for the reaction to form CO_2, $\nu_{O_2} = 1$. Figure A.1 indicates that in equilibrium $Y_{O_2,w} \approx 0$, so Equation 2.53 is obtained:

$$B = rY_{O_2,\infty} \qquad 2.53$$

Using the appropriate value of ν_{O_2}, the plateaus $B = 0.087$ and $B = 0.174$ are obtained for temperature ranges in which a single dominant reaction produces CO_2 and CO respectively. Also shown in Figure A.2 is the sublimation regime, where the rate of mass loss of carbon increases greatly.

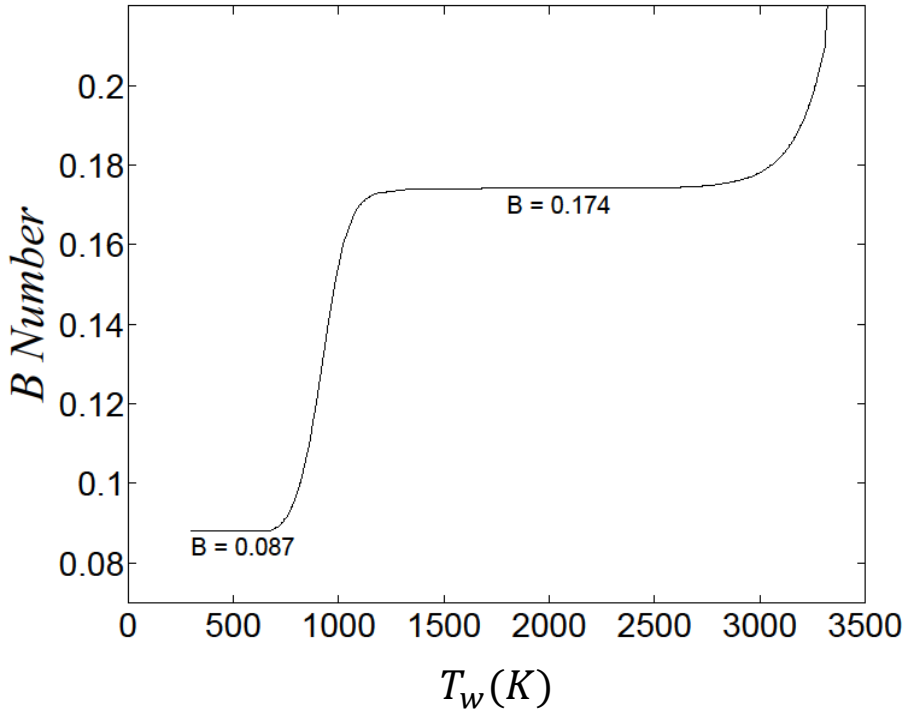

Figure A.2: B vs. T_w curve generated using ACE.

For scenarios which are diffusionally controlled, the results of equilibrium codes such as ACE are correct. However, when transport rates are comparable to or faster than reaction rates, we expect to see departures from the equilibrium limit. The results of Figure A.2 are used in section 2.2.4.4 to describe the transition from equilibrium to nonequilibrium behavior in thermochemically ablating systems.

Appendix B: Nominal Values for Parameters Used in Ablation Models

Table B.1: Nominal values of parameters used in validation of simplified model by data of Matsui et al.

Parameter	Value	Source
A_{O_2}	2.53e7 m/s	[17]
B_{max}	0.174	Equation 2.66.
$c_{p,air}$	1204 J/kg-K	[67]
$c_{p,C}$	1004.5 J/kg-K	[1]
$c_{p,CO}$	1683 J/kg-K	[67]
c_{p,O_2}	1136 J/kg-K	[67]
E_{a,O_2}	1.98e5 kJ/kmol 1.41e5 kJ/kmol	Matsui et al. [17]. Tognotti et al. [18].
$\tilde{\imath}_C^o$	0 kJ/mol	[68]
$\tilde{\imath}_{CO}^o$	-110.54 kJ/mol	[68]
$\tilde{\imath}_{O_2}^o$	0 kJ/mol	[68]
$\Delta i_{comb,O_2}$	6.91 kJ/g O_2	Equation 2.27.
k_{flow}	0.0584 W/m-K	Evaluated at film temperature of 844 K [69].
P	101.3 kPa	Assume atmospheric pressure.
Pr	0.70	Evaluated at film temperature of 844 K [69].
T_∞	288 K	[17]
T_{surr}	288 K	Assume $T_{surr} = T_\infty$.
T_T	288 K	Assume $T_T = T_\infty$.
$Y_{O_2,\infty}$	0.232	Assume air with only O_2 and N_2.
α	1	Assume black body.
ε	1	Assume black body.
ν_{flow}	88.86e-6 m^2/s	Evaluated at film temperature of 844 K [69].
ρ_v	2162.5 kg/m^3	[1]

Table B.2: Values of heat transfer coefficient with corresponding values of velocity gradient.

a [1/s]	h [W/m^2-K], untuned	h [W/m^2-K], tuned
1480	158	78.7
600	100	50.1
470	88.7	44.4
247	64.3	32.2
120	44.8	22.4
41	26.2	13.1
15.8	16.3	8.1

Table B.3: Nominal values of parameters used in reentry simulation for PICA with mechanical erosion.

Parameter	Value	Source
$A_{O_2,*}$	50 m/s	[31]
$B_{ox,max}$	0.174	Equation 2.66.
$c_{p,air}$	1204 J/kg-K	[67]
$c_{p,C}$	1400 J/kg-K	[1]
$c_{p,CO}$	1683 J/kg-K	[67]
c_{p,O_2}	1136 J/kg-K	[67]
D_{eff}	3e-3 m^2/s	[31]
d_c^*	0.038	Calculated, shown for convenience.
d_o	10 μm	[32]
$E_{a,O_2,*}$	1.2e5 kJ/kmol	[31]
h	60.6 W/m^2-K	Calculated, shown for convenience.
$\tilde{\imath}_C^o$	0 kJ/mol	[68]
$\tilde{\imath}_{CO}^o$	-110.54 kJ/mol	[68]
$\tilde{\imath}_{O_2}^o$	0 kJ/mol	[68]
$\Delta i_{comb,O_2}$	6.91 kJ/g O_2	Equation 2.27.
$k = c_p/c_v$	1.4	Assumed for air.
P_∞	3.54 Pa	[33]
Pr	0.71	Assumed for air.
R_n	0.2202 m	[33]
T_∞	221.6 K	[33]
T_{surr}	300 K	Assumed.
T_T	300 K	Assume $T_T = T_{surr}$.
U_∞	12063 m/s	[33]
u	1 m/s	[31]
$Y_{O_2,\infty}$	0.232	Assume air, O_2 and N_2 only.
α	1	Assume black body.
ε	1	Assume black body.
$\mu_{e,st}$	2.196e-4 kg/m-s	Lennard-Jones potential, parameters from [36].
μ_w	6.608e-5 kg/m-s	Lennard-Jones potential, parameters from [36].
ρ_s	1800 kg/m^3	[31]
ρ_∞	0.00192 mol/m^3	[33]
σ_u	1000 MPa	[43]
φ_o	0.1	[31]

Appendix C: Exploration of Nonequilibrium Behavior in Systems with Multiple Reactions

As stated in section 2.2.4.5, this section includes exploratory work on the development of analytical solutions for nonequilibrium ablating systems with multiple surface reactions. Its contents have not been validated, and the section should be used only as a reference for future work done in this area.

We consider a situation in which solid carbon is degraded by a set of K surface reactions of the form $\nu_C C + \nu_r R \rightarrow \nu_p P$, with no internal pyrolysis, where each reaction is governed by a rate equation analogous to the oxidation reaction considered in section 2.1.2. The nondimensionalized set of governing equations in terms of the B number is then

$$B = \sum_{k=1}^{K} B_k \tag{C.1a}$$

$$-\phi_k + B(1-\phi_k) + \frac{B_k}{B_{max,k}} = 0 \tag{C.1b}$$

$$-\theta + \sum_{k=1}^{K}\left[\frac{Da_k}{Da_{M,k}}\left(\frac{B_k}{B_{max,k}}\right)H_k\right] + \frac{\alpha \dot{q}''_{ext}}{hT_\infty} - \frac{\varepsilon\sigma {T_\infty}^3}{h}\left[(\theta+1)^4 - \left(\frac{T_{surr}}{T_\infty}\right)^4\right] = 0 \tag{C.1c}$$

where B_k, $B_{max,k}$, Da_k, $Da_{M,k}$, and H_k are defined for each k as if that reaction were the single reaction considered earlier. Because the total B is the sum of the B_k contributions from the separate reactions, this theory cannot be applied to systems with multi-step reactions. In Equation C.1b, only the mass balances for the reactant gas species are considered, since the product species concentrations are directly tied to the reactant concentrations through the definition of the B number (Equation 2.48). We rearrange Equation C.1b, seeking relationships between B_k and ϕ_k as in Equation 2.69:

$$\frac{B_k}{B_{max,k}} = \frac{\phi_k}{\left(\frac{B}{B_k}\right)B_{max,k}(1-\phi_k)+1} \tag{C.2}$$

In this case the denominator on the right side may not go to 1 if B/B_k is large. Figure C.1 plots $B_k/B_{max,k}$ vs. ϕ_k for several values of B/B_k.

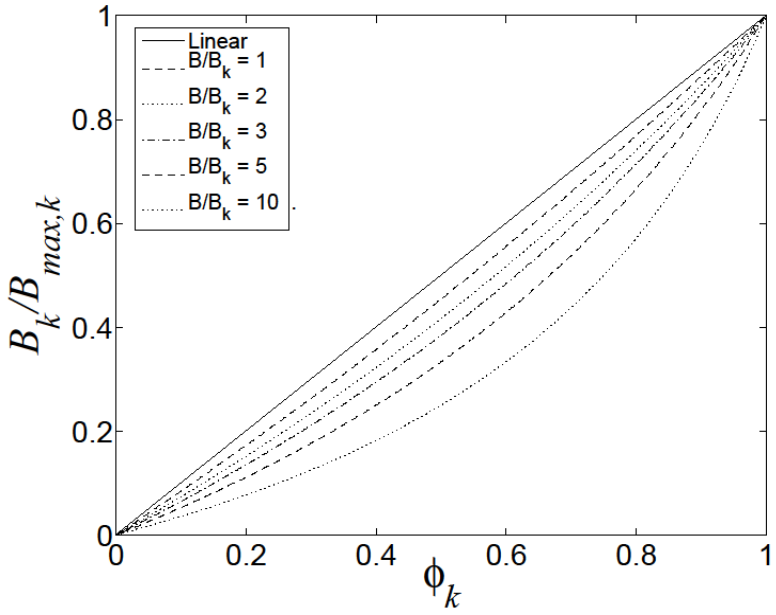

Figure C.1: $B_k/B_{max,k}$ versus ϕ_k for several values of B/B_k.

For values of $B/B_k \lesssim 3$, the relationship is still close to linear. This means that for the most dominant reactions,

$$\frac{B_k}{B_{max,k}} \approx \phi_k \qquad \text{C.3}$$

We then have the similar result to before for $B_k/B_{max,k}$:

$$\frac{B_k}{B_{max,k}} \approx \frac{\overline{Da}_k}{1+\overline{Da}_k} \qquad \text{C.4}$$

We now assume that for the minor reactions, $B_k \approx 0$, and obtain the final form of the energy balance:

$$-\theta + \sum_{\substack{dominant \\ reactions}} \left[\frac{Da_k}{Da_{M,k}} \left(\frac{\overline{Da}_k}{1 + \overline{Da}_k} \right) H_k \right] + \frac{\alpha \dot{q}''_{ext}}{hT_\infty} - \frac{\varepsilon \sigma {T_\infty}^3}{h} \left[(\theta + 1)^4 - \left(\frac{T_{surr}}{T_\infty} \right)^4 \right] = 0 \qquad \text{C.5}$$

Finally we see that for multiple reactions, in the kinetically controlled regime, the mass loss rate is governed by the following dimensionless parameters:

$$\dot{m}'' = \dot{m}'' \left(Da_k, Da_{M,k}, \gamma_k, \frac{\alpha \dot{q}''_{rad}}{hT_\infty}, \frac{\varepsilon \sigma {T_\infty}^3}{h}, \frac{T_{surr}}{T_\infty}, \frac{c_p T}{\Delta i_{comb,k}} \right) \qquad \text{C.6}$$

where k includes only the dominant reactions.

References

1 Anzalone, R.A. “A Toolkit for Characterizing Uncertainties in Hypersonic Flow-Induced Ablation.” MS thesis. The University of Texas at Austin, 2010.

2 Moyer, C.B. and Rindal, R.A., “Finite Difference Solution for the In-Depth Response of Charring Materials Considering Surface Chemical and Energy Balances”, NASA CR-1061, 1968.

3 Kendall, R.M., Rindal, R.A., and Bartlett, E.P., “A Multicomponent Boundary Layer Chemically Coupled to an Ablating Surface”, *AIAA Journal*, Vol. 5, No. 6, 1967, pp. 1063-1071.

4 “User’s Manual, Aerotherm Chemical Equilibrium Computer Program (ACE 81)”, UM-81-11/ATD, Acurex Corporation, Aerotherm Division, Mountain View, CA, 1981.

5 Chen, Y.-K. and Milos, F.S., “Ablation and Thermal Response Program for Spacecraft Heatshield Analysis”, *Journal of Spacecraft and Rockets*, Vol. 36, No. 3, 1999, pp. 475-483.

6 Chen, Y.-K. and Milos, F.S., “Two-Dimensional Implicit Thermal Response and Ablation Program for Charring Materials”, *Journal of Spacecraft and Rockets*, Vol. 38, No. 4, 2001, pp. 473-481.

7 Blackwell, B.F., Amar, A.J., and Edwards, J.R., “One-Dimensional Ablation with Pyrolysis Gas Flow Using a Full Newton’s Method and Finite Control Volume Procedure”, *39th AIAA Thermophysics Conference*, AIAA 2007-4535, AIAA, Miami, FL, 2007.

8 Zhluktov, S.V., and Abe, T., “Viscous Shock-Layer Simulation of Air-flow past Ablating Blunt Body with Carbon Surface”, *Journal of Thermophysics and Heat Transfer*, Vol. 13, No. 1, 1999, pp. 50-59.

9 Chen, Y.-K. and Milos, F.S., “Navier-Stokes Solutions with Finite Rate Ablation for Planetary Mission Earth Reentries”, *Journal of Spacecraft and Rockets*, Vol. 42, No. 6, 2005, pp. 961-970.

10 Glassman, I., Combustion, 3rd edition, San Diego: Academic Press, Inc., 1996.

11 Kanury, M.S., Introduction to Combustion Phenomena, New York: Gordon and Breach Science Publishers, 1975.

12 Quintiere, J.G., Fundamentals of Fire Phenomena, Hoboken: John Wiley & Sons, 2006.

13 Upadhyay, R.R., Bauman, P.T., Stogner, R.H., Schulz, K.W., and Ezekoye, O.A., "Steady-State Ablation Model Coupling with Hypersonic Flow," 48th AIAA Aerospace Sciences Meeting Including the New Horizons Forum and Aerospace Exposition 2010, AIAA-2010-1176, Orlando, FL, January 2010.

14 McBride, B.J. and Gordon, S., "Computer Program for Calculation of Complex Chemical Equilibrium Compositions and Applications II. User's Manual and Program Description", NASA RP-1311, 1996.

15 Kays, W., Crawford, M., and Weigand, B., Convective Heat and Mass Transfer, 4th edition, Boston: McGraw-Hill, 2005.

16 Mills, A.F., Mass Transfer, New Jersey: Prentice-Hall, 2001.

17 Matsui, K., Koyama, A., and Uehara, K., "Fluid-Mechanical Effects on the Combustion Rate of Solid Carbon," *Combustion and Flame*, Vol. 25, 1975, pp. 57-66.

18 Tognotti, L., Longwell, J.P., and Sarofim, A.F., "The Products of the High Temperature Oxidation of a Single Char Particle in an Electrodynamic Balance," Twenty-Third Symposium (International) on Combustion/The Combustion Institute, 1990, pp. 1207-1213.

19 White, F.M., Viscous Fluid Flow, 3rd edition, Boston: McGraw-Hill, 2006.

20 Fendell, F.E., "The Burning of Spheres Gasified by Chemical Attack," *Combustion Science and Technology*, Vol. 1, 1969, pp. 13-24.

21 Schneider, P.J., Dolton, T.A., and Reed, G.W., "Mechanical Erosion of Charring Ablators in Ground-Test and Re-Entry Environments," AIAA Journal Vol.6 Jan. 1968, pp 64-72.

22 Lundell, J.H., "Spallation of the Galileo Probe Heat Shield," AIAA Paper 82-0852.

23 Yoshinaka, T., Mizuno, M., and Morino, Y., "Detection of Ablator Spallation Phenomena at Arc Wind Tunnel Tests," IEPC-99-025.

24 Raiche, G.A., II, and Driver, D.M., "Shock Layer Optical Attenuation and Emission Spectroscopy Measurements During Arc Jet Testing with Ablating Models," AIAA Paper 2004-0825, Jan. 2004.

25 Park, C., "Radiation of Spalled Particles in Shock Layers," Journal of Thermophysics and Heat Transfer Vol.18 No.4 Oct.-Dec. 2004, pp 519-526.

26 Ziering, M., and DiCristina, V., "Thermomechanical Erosion of Ablative Plastic Composites," AIAA Paper 72-299, June 1972.

27 Ren, F., Sun, H.S., and Liu, L.Y., "Theoretical Analysis for Mechanical Erosion of Carbon-Base Materials in Ablation," Journal of Thermophysics and Heat Transfer Vol.10 No.4 Oct.-Dec. 1996, pp 593-597.

28 Dimitrienko, Y.I., Thermomechanics of Composites under High Temperature, Dordrecht: Kluwer Academic Publishers, 1999.

29 Mathieu, R.D., "Mechanical Spallation of Charring Ablators in Hyperthermal Environments," AIAA Journal Vol.2 No.9 Sept. 1964, pp 1621-1627.

30 Stackpoole, M., Sepka, S., Cozmuta, I., and Kontinos, D., "Post-Flight Evaluation of Stardust Sample Return Capsule Forebody Heat-Shield Material," AIAA Paper 2008-1202, Jan. 2008.

31 Lachaud, J., Cozmuta, I., Mansour, N.N., "Multiscale Approach to Ablation Modeling of Phenolic Impregnated Carbon Ablators," *Journal of Spacecraft and Rockets*, Vol. 47, No. 6, 2010.

32 Lachaud, J., Mansour, N.N., Ceballos, A., Pejakovic, D., Zhang, L., and Marschall, J., "Validation of a volume-averaged fiber-scale model for the oxidation of carbon-fiber preform," 42nd AIAA Thermophysics Converence, 27-30 June 2011, Honolulu, Hawaii.

33 Boyd, I.D., Trumble, K.A., and Wright, M.J., "Modeling of Stardust Entry at High Altitude, Part 1: Flowfield Analysis," *Journal of Spacecraft and Rockets*, Vol. 47, No. 5, 2010, pp. 708-717.

34 Wilmoth, R.G., Mitcheltree, R.A., and Moss, J.N., "Low-Density Aerodynamics of the Stardust Sample Return Capsule," AIAA Paper 97-2510, 1997.

35 Blottner, F.G., "Finite Difference Methods of Solution of the Boundary-Layer Equations," *AIAA Journal*, Vol. 8, No. 2, February 1970, pp. 193-205.

36 Anderson, J.D., Hypersonic and High Temperature Gas Dynamics, McGraw-Hill, 1989.

37 Koppenwallner, G., "Fundamentals of Hypersonics: Aerodynamics and Heat Transfer," in the Short Course Notes entitled *Hypersonic Aerothermodynamics*, presented at the Von Karman Institute for Fluid Dynamics, Rhose Saint Genese, Belgium, February 1984.

38 Kemp, H.H., Rose, R.H., and Detra, R.W., "Laminar Heat Transfer Around Blunt Bodies in Dissociated Air," *Journal of the Aerospace Sciences*, Vol. 26, No. 7, July 1959, pp. 421-430.

39 Beckwith, I.E., and Gallagher, J.J., "Local Heat Transfer and Recovery Temperatures on a Yawed Cylinder at a Mach Number of 4.15 and High Reynolds Numbers," NASA TR-R-104, 1962.

40 Fay, J.A., and Riddell, F.R., "Theory of Stagnation-Point Heat Transfer in Dissociated Air," *Journal of the Aeronautical Sciences*, Vol. 25, No. 2, 1958, pp. 73-85.

41 Crabtree, L.F., Dommett, R.L., and Woodley, J.G., "Estimation of Heat Transfer to Flat Plates, Cones, and Blunt Bodies", R. & M. No. 3637, 1970.

42 Munson, B.R., Young, D.F., and Okiishi, T.H., Fundamentals of Fluid Mechanics, 5th edition, John Wiley & Sons, Inc., 2006.

43 Fitzer, E., and Manocha, L.M., Carbon Reinforcements and Carbon/Carbon Composites, Springer, 1998.

44 Driver, D.M., Carballo, J.E., Beck, R., Prabhu, D., Santos, J.A., Cassell, A., Skokova, K., Tang, C., Hwang, H.H., Slimko, E., Willcockson, W., and Songer, J., "Arc Jet Testing in a Shear Environment for Mars Science Laboratory Thermal Protection System," 41st AIAA Thermophysics Conference, 22-25 June 2009, San Antonio, Texas.

45 Driver, D.M., Olson, M.W., Barnhardt, M.D., and MacLean, M., "Understanding High Recession Rates of Carbon Ablators Seen in Shear Tests in an Arc Jet," 48th AIAA Aerospace Sciences Meeting Including the New Horizons Forum and Aerospace Exposition, 4-7 January 2010, Orlando, Florida.

46 Quintiere, J.G., Fundamentals of Fire Phenomena, Hoboken: John Wiley & Sons, 2006.

47 Drysdale, D., An Introduction to Fire Dynamics, 2nd edition, Hoboken: John Wiley & Sons, 1998.

48 Woycheese, J.P., Pagni, P.J. and Liepmann, D., "Brand Propagation from Large-Scale Fires," *Journal of Fire Protection Engineering*, Vol. 10, No. 2, 1999, pp. 32-44.

49 Woycheese, J.P., Pagni, P.J. and Liepmann, D., "Brand Lofting Above Large-Scale Fires," *Proceedings of the Second International Conference of Fire Research and Engineering*, Society of Fire Protection Engineers, 1998, pp. 137-150.

50 Huang, H., Ooka, R., Kato, S., and Hayashi, Y., "A Numerical Study of Firebrands Scattering in Urban Fire Based on CFD and Firebrands Aerodynamics Measurements," *Journal of Fire Sciences*, Vol. 25, 2007, pp. 355-378.

51 Anthenien, R.A., Tse, S.D., and Fernandez-Pello, A.C., "On the trajectories of embers initially elevated or lofted by small scale ground fire plumes in high winds," *Fire Safety Journal*, Vol. 41, 2006, pp. 349-363.

52 Albini, F.A., "Spot Fire Distance From Burning Trees – A Predictive Model," General Technical Report INT-56, USDA Forest Service, 1979.

53 Sardoy, N., Consalvi, J.-L., Porterie, B., and Fernandez-Pello, A.C., "Modeling transport and combustion of firebrands from burning trees," *Combustion and Flame*, Vol. 150, 2007, pp. 151-169.

54 Manzello, S.L., Cleary, T.G., Shields, J.R., Maranghides, A., Mell, W., and Yang, J.C., "Experimental investigation of firebrands: Generation and ignition of fuel beds," *Fire Safety Journal*, Vol. 43, 2008, pp. 226-233.

55 Manzello, S.L., Park, S., Suzuki, S., Shields, J.R., and Hayashi, Y., "Experimental investigation of structure vulnerabilities to firebrand showers," *Fire Safety Journal*, Vol. 46, 2011, pp. 568-578.

56 Yoshioka, H., Hayashi, Y., Masuda, H., and Noguchi, T., "Real-Scale Fire Wind Tunnel Experiment on Generation of Firebrands from a House on Fire," *Fire Science and Technology*, Vol. 23, 2004, pp. 142-150.

57 Manzello, S.L., Maranghides, A., and Mell, W.E., "Firebrand generation from burning vegetation," *International Journal of Wildland Fire*, Vol. 16, 2007, pp. 458-462.

58 Mandelbrot, B.B., The Fractal Geometry of Nature, New York: W.H. Freeman and Company, 1977.

59 Collin, A., Lamorlette, A., Bernardin, D., and Séro-Guillaume, O., "Modelling of tree crowns with realistic morphological features: New reconstruction methodology based on Iterated Function System tool," *Ecological Modelling* 222, 2011, pp. 503-513.

60 Vovelle, C., Mellottee, H., and Delfau, J.L., "Kinetics of thermal degradation of wood and cellulose by T.G.A. comparison of the calculation techniques," National Meeting of the American Chemical Society, 1983.

61 Ostman, B.A.-L., "Wood tensile strength at temperatures and moisture contents simulating fire conditions," *Wood Science and Technology*, Vol. 19, 1985, pp. 103-116.

62 Kretschmann, D.E., Wood Handbook, Chapter 05: Mechanical Properties of Wood, Department of Agriculture, Forest Service, Forest Products Laboratory, 2010.

63 Hilpert, R., *Forsch. Geb. Ingenieurwes*., Vol. 4, 1933, pp. 215.

64 McCaffrey, B.J., *Purely Buoyant Diffusion Flames: Some Experimental Results*, NBSIR 79-1910, National Bureau of Standards, 1979.

65 Johnson, E.A., and Miyanishi, K., Forest Fires: Behavior and Ecological Effects, San Diego: Academic Press, 2001.

66 Gordon, S., and McBride, B.J., "Computer Program for Calculation of Complex Chemical Equilibrium Compositions and Applications I. Analysis," NASA Reference Publication 1311, October 1994.

67 Schmidt, P.S., Ezekoye, O.A., Howell, J.R., and Baker, D.K., Thermodynamics: An Integrated Learning System, John Wiley & Sons, Inc., 2006.

68 Bejan, A., Advanced Engineering Thermodynamics, 3rd edition, John Wiley & Sons, Inc., 2006.

69 Mills, A.F., Heat Transfer, 2nd edition, New Jersey: Prentice Hall, Inc., 1999.

Vita

Benjamin Barr was born in 1988 in Austin, Texas. He attended L. C. Anderson High School and graduated in May 2006. He received his Bachelor of Science in Mechanical Engineering from the University of Texas at Austin in May 2010. He entered graduate school in the Thermal/Fluid Systems Department of the Department of Mechanical Engineering at the University of Texas at Austin in August 2010 and is due to receive his Master of Science in Mechanical Engineering in May 2012.

Author's email address: benjamin.w.barr@gmail.com
This thesis was typed by Benjamin Witten Barr.